Time-resolved X-ray Studies of Electric-field Induced Switching in Smectic Liquid Crystals

A thesis submitted to the University of Manchester for the degree of
Doctor of Philosophy in the Faculty of Science

1995

Adrian Morse

Department of Physics

Manchester University

CONTENTS

Abstract

Switching processes in planar smectic-A and surface stabilised ferroelectric liquid crystal cells have been studied in detail. The technique of low angle time-resolved x-ray diffraction was used to look specifically at the behaviour of smectic layers during switching with electric fields. The x-ray source was the synchrotron radiation facility at Daresbury Laboratory in the U.K. Complementary electro-optic experiments were performed to observe the motion of the liquid crystal director and correlate this motion with the layer behaviour.

The smectic-A material chosen for investigation was S3, which has positive dielectric anisotropy. This was contained in a home-made cell, similar to those used in displays. The cell allowed both x-ray and visible light observations. The liquid crystal thickness was 15µm and the inner cell surfaces were rubbed anti-parallel with P.V.A to promote unidirectional planar alignment. An initial x-ray rocking experiment showed that there was in fact a chevron structure in the smectic-A phase. Chevrons were shown to form due to the decrease in layer spacing when cooling from the nematic phase.

At 51.5°C, the temperature chosen for smectic-A switching, the chevron angle was approximately 10°. A 30Vr.m.s 1kHz sinusoidal voltage was applied across the cell thickness to produce a transition from a chevron to a homeotropic structure. Optical observations showed that the switching was complete within about 8 seconds. Layer behaviour during the switching process was monitored using low angle time-resolved x-ray diffraction. The experiment was repeated at different angles; the resulting set of rocking curves showed the complete structural evolution with time. The results showed that a multi-domain system had formed, with layers remaining intact throughout the early stages of switching. The layers in each arm of the chevron structure rotated towards their nearest cell wall. An asymmetric chevron structure formed before breaking up. The apparatus did not allow examination of the final layer structure. Photographs of the switching process show that the structural changes began near cell defects and that layer rotation propagated along the layers in preference to co-operative rotation with neighbouring domains.

For the ferroelectric experiments the material chosen was SCE13. The cell was similar to that used for the smectic-A material except that the thickness of the ferroelectric liquid crystal was 4µm. An initial x-ray rocking experiment showed a chevron structure within the cell; the room temperature chevron angle was about 22.5°.

The effect of high electric fields was examined by performing x-ray rocking experiments at increasing voltages. Significant changes were seen at a voltage of 10V D.C: A sharp chevron structure converted to an obtuse structure with a lower angle. The Bragg diffraction spots arced on the detector showing that a simultaneous layer reorientation had taken place in the plane of the cell surfaces. The structural transformations were irreversible and accompanied by notable changes in the optical texture.

To examine the effect of low electric fields the cell was oriented to give a Bragg diffraction spot on the area detector. The intensity and position of the spot was observed with time during director switching. The results show that the switching involves a small (~1°) layer rotation in the planes parallel to the cell faces and a simultaneous "wobble" of the chevron structure.

About the Author

The author obtained a First Class degree in Physics from Salford University in 1990. The 4-year course included a year in the Quality Control section of the 3M UK (Scotch) videotape facility in Swansea. After graduating the author was employed as a Graduate Engineer for GEC-Marconi Underwater Systems in Portsmouth. During this period the author worked in the areas of electromagnetic compatibility and torpedo trials analysis. After one year with Marconi the author left to embark on an S.E.R.C-funded Ph.D. course and was fortunate to obtain sponsorship from GEC Research. The Ph.D. research work is described in this thesis. During the Ph.D. period the author obtained a European scholarship to attend a two-month course in Grenoble, France for users of large experimental facilities (H.E.R.C.U.L.E.S). On completing the 3-year S.E.R.C-funded period the author obtained a temporary lectureship post in the Manchester University Physics Department.

Acknowledgements

I would like to thank the many people who have helped me during my Ph.D. Those due special thanks include:

- Dr. Helen Gleeson, my supervisor, for having the inspiration to choose such an interesting project, for not listening when the sceptics told her it couldn't be done, for her constant encouragement and support, and for offering that feature lacking from many academic supervisors—her supervision.

- Dr. Mike Wiltshire, my industrial supervisor, for his fruitful discussions; SERC and GEC Research for financial support in the form of a collaborative CASE award.

- My friends in the Physics Department, for their assistance and discussions.

- Dr. Stewart Cummings for his guidance on x-ray techniques and Daresbury meals.

- Dr. Nick Bowring for the benefits of his computational expertise.

- Dr. Carlo Carboni for saving me from cabin fever during those long nights at the synchrotron source.

- Drs. John Harries and Sue Slawson of the Daresbury S.R.S staff, for their help in setting up the x-ray experiments.

- The technical staff in the Physics Department, who have always been friendly and helpful.

I would also like to thank my family for their love and encouragement during the Ph.D. Thanks are due also, to my girlfriend's parents for their friendship and support. Finally, the biggest thank-you must go to my girlfriend, Irina, for her love, friendship and understanding during the successes and crises of academic research.

Chapter 1

INTRODUCTION

Liquid crystals are familiar for their use in electro-optic displays, such as those in watches, calculators and computers. Although they were discovered at the end of the last century, their full potential in displays remained unexploited until the 1960s. The liquid crystal displays of today are clear, fast, portable, and consume little power. Much of the present research regarding liquid crystal displays is aimed at the development of large, robust displays for incorporation into flat, wall-mounted televisions. Besides their use in displays, liquid crystals are also important for their thermo-optic properties, and for their behaviour in biological systems. The reader is referred to reference [1] for more details on liquid crystal applications.

A liquid crystal is a material that exhibits one or more phases between the crystalline solid phase and the isotropic liquid phase. As the name suggests, a liquid crystal phase displays characteristics of both liquids and crystals. The liquid nature is manifested by the ability of the material to flow and occupy the volume available to it. The crystal nature is reflected by the presence of at least one degree of long-range order within the sample. A liquid crystal electro-optic display takes advantage of this dual nature. The presence of order gives the material bulk optical characteristics, which are dependent on the mean molecular orientation. The fluidity allows this orientation to be changed in response to an electric field.

A phase that possesses only orientational order is called a nematic. In addition to the orientational order the molecules of the material may be arranged in layers. Such phases are termed smectic. Nematic and smectic phases are discussed in detail in chapter 2. The experimental work presented in this thesis concerns two types of smectic phases; the smectic-A phase, in which the molecules are perpendicular to the layers, and the chiral smectic-C (ferroelectric) phase, in which the molecules are tilted with respect to the layers. The structures of these particular phases are discussed in detail in chapter 2.

The main objective of this thesis was a study of the reorientation (switching) processes in home-made liquid crystal displays, containing the aforementioned smectic phases. There have been many optical studies of such processes, using visible light to monitor the collective rotation of molecules. (These studies and the subsequent switching models are presented in chapter 2.) This thesis, however, reports the use of time-resolved low angle x-ray diffraction to look at the motion of the molecular layers rather than the average motion of the molecules themselves.

X-ray diffraction theory is introduced in chapter 3. The theory includes realistic and idealised diffraction patterns from smectic liquid crystals and discusses the information obtainable from them. The production and properties of synchrotron x-rays are also discussed.

Chapter 4 gives details of the smectic-A experiments. The apparatus and experimental procedures are given. The results of the x-ray experiments and complementary optical experiments are discussed in the light of the switching models introduced in chapter 2.

Chapter 5 gives details of the apparatus, experimental procedures and results of the ferroelectric experiments. The effects of both high and low electric fields were examined. The high electric field experiment consisted of x-ray measurements before and after switching, and is called the *static* experiment. The low electric field experiment consisted of time-resolved x-ray measurements during switching, and is called the *dynamic* experiment. The results of both experiments are considered in the light of the models introduced in chapter 2.

The thesis is summarised in chapter 6 and suggestions are given for future research.

There are two appendices. The first is a review of defect structures in smectic liquid crystals, and may help the reader with the smectic-A discussion in chapter 2. The second is a reference guide to the interpretation of rocking curves, which may help the reader at various stages throughout this thesis.

Note that the full version of the thesis contains an additional chapter that reproduced a published paper. That chapter has been omitted from this abridged version for reasons of brevity.

Chapter 2

LIQUID CRYSTAL THEORY

2.1 Introduction

This thesis examines the switching processes in smectic-A and ferroelectric (chiral smectic-C) liquid crystal devices. This chapter provides the liquid crystal theory relevant to the experimental work.

2.2 Formation of a Liquid Crystal Phase

Liquid crystal phases occur only in organic materials composed of molecules with geometric anisotropy [2][3][4]. The phase can form due to the action of heat alone (thermotropic liquid crystals) or additionally as a function of concentration in solution (lyotropic liquid crystals). A variety of phases is possible and the material can exhibit one or more phases. The work reported in this thesis concerns low molar mass rod-shaped, thermotropic materials.

2.3 A Brief Description of the Relevant Phases

A thermotropic liquid crystal is generally classified as one of four types: nematic, smectic discotic or cholesteric. The work described in this thesis involves smectic phases; for details of other phases see reference [5].

In its isotropic liquid state (**I**) a material possesses no long-range order. As the material is cooled it might first form a nematic phase (**N**). The order in this phase is directional only; molecules point along an average direction defined by a unit vector **n** (the director). There is still only liquid-like short-range correlation between the centres of mass (Figure 1).
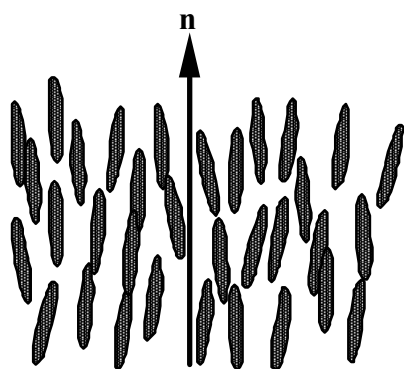
Figure 1: The nematic phase.

At high temperatures within the nematic phase the molecular fluctuations are large, resulting in a large distribution of angles about the director. As the temperature is lowered the spread of angles

is reduced and the directional order increases. This is reflected in the orientational order parameter, *S*, as defined in Equation 1.

$$S = \frac{1}{2}\left\langle 3\cos^2\theta - 1 \right\rangle$$

Equation 1

where θ is the orientation of a single molecule with respect to the director.

At lower temperatures, the sample might enter a smectic phase. In addition to directional order a smectic phase has at least one degree of positional order. This is manifested by a density wave in the direction of the director, so that, to a first approximation, the molecules appear layered. Figure 2 shows the simplest of the smectic phases, a smectic-A phase.
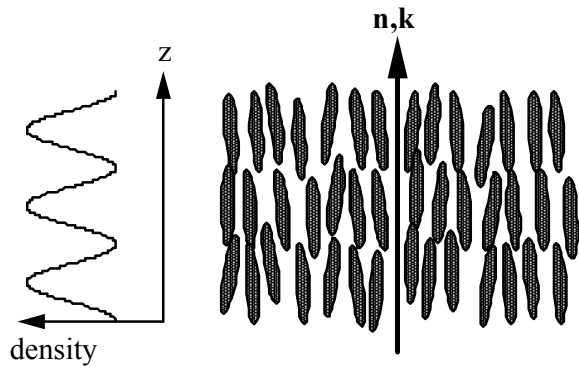
Figure 2: The smectic-A phase.

The ordering is quasi long range and is represented by a series of smectic order parameters τ:

$$\tau_n = \cos 2\pi(n\,z/d)$$

Equation 2

where *n* is an integer, *z* is the distance along the layer normal from some arbitrary origin, and *d* is the mean layer repeat distance. Larger values of *n* correspond to deviation from a purely cosine layer distribution. Within a layer the system may adopt a number of structures with different degrees of order. The simplest is smectic-A ($\mathbf{S_A}$) which has only short-range order between molecules within a layer. The molecules are arranged such that the director is parallel to the layer normal $\mathbf{k}$ (Figure 2). In the smectic-C ($\mathbf{S_C}$) phase the molecules are tilted within each layer (Figure 3). The chiral smectic-C ($\mathbf{S_C}$*) phase is further complicated. Molecular chirality causes the director to precess about the layer normal in a helical manner (Figure 4). Other smectic phases ($\mathbf{B}$, $\mathbf{E}$ etc.) exist; these exhibit additional order within the layers (see reference [6]).

Figure 3: The smectic-C phase. 　　　　　　*Figure 4: The chiral smectic-C phase.*

2.4   Theory of Smectic-A Liquid Crystals

2.4.1 Electrical properties

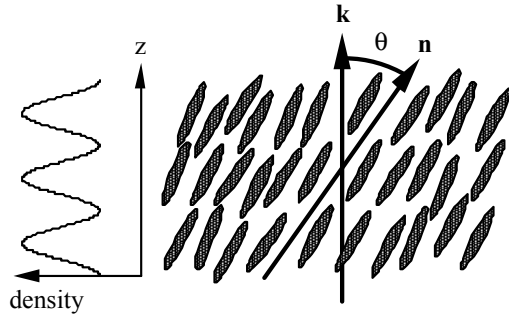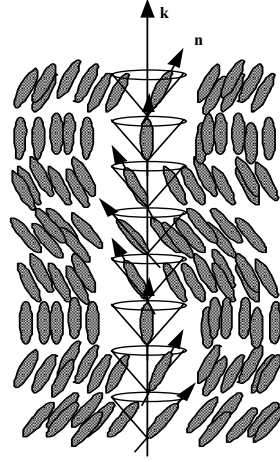Smectic-A materials respond to an applied electric field by forming induced dipoles i.e. they are dielectric. The response of a dielectric material to an applied field is indicated by its polarisation **P**, the dipole moment per unit volume, which is a measure of the separation of charge in the material. **P** is a vector quantity; for low fields it is related to the applied field as described in Equation 3.

$$\mathbf{P} = \varepsilon_0 \; \varepsilon_r \, \mathbf{E}$$　　　　　　　　　　　　　　　　　　　　　　　　　　　　　*Equation 3*

where ε_0 is the dielectric susceptibility of a vacuum and ε_r is the relative dielectric permittivity (strictly speaking a tensor). A macroscopic *spontaneous* polarisation (ferroelectricity) cannot form in the smectic-A phase. Such polarisation requires reduced symmetry so that molecular rotation is hindered and local molecular dipole moments do not average to zero. (Using symmetry arguments in 1975 Meyer *et al.* [7] suggested that the reduced symmetry condition could be achieved in a chiral smectic-C phase.)

Reference [8] shows that the dielectric permittivity tensor, ε_r is given by:

$$\varepsilon_r = \varepsilon' + i\varepsilon''$$　　　　　　　　　　　　　　　　　　　　　　　　　　　　　*Equation 4*

ε' represents the combined effect of the molecular polarisability and the permanent dipole moments. ε'' represents the dielectric losses. When the bulk material is anisotropic, as in an aligned liquid crystal, ε' becomes $\langle\varepsilon'\rangle$, a weighted average of the contributions perpendicular ($\varepsilon_\perp$) and parallel ($\varepsilon_\parallel$) to the molecules (Equation 5):

$$\langle\varepsilon'\rangle = (\varepsilon_\parallel + 2\varepsilon_\perp)/3$$　　　　　　　　　　　　　　　　　　　　　　　　*Equation 5*

$\varepsilon_\perp$ and $\varepsilon_\parallel$ reduce in value with increasing frequency as dipole reorientation is inhibited. In the

case of $\varepsilon_\parallel$ this orientation is occurs about a transverse axis through the centre of molecular mass, with a long relaxation time. In the case of $\varepsilon_\perp$ the orientation concerns the rotation about the long axis of the molecule, and is thus quicker (Figure 5).
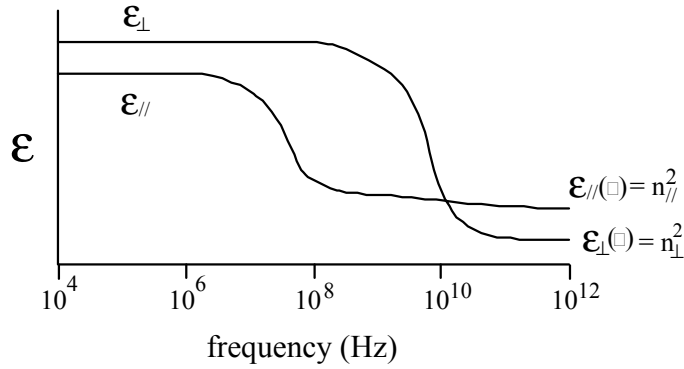

Figure 5: Typical behaviour of dielectric permittivity with applied field frequency.

The difference between $\varepsilon_\parallel$ and $\varepsilon_\perp$ is known as the dielectric anisotropy $\Delta\varepsilon$. It is the important parameter when discussing the switching of liquid crystals in electric fields.

2.4.2 Behaviour in an electric field

There has been much research concerning the response of nematic liquid crystals to electric fields [5][9]. There has been less enthusiasm for research into smectic-A switching as the high viscosity results in slow response times and difficulty in relaxing back to the original state when the field is removed. (Smectic-A materials with chiral molecules can switch faster via the "electroclinic effect" [10].) Switching in smectic-A materials is best explained by comparison with switching in nematics.

It can be shown [11] that three types of elastic deformations can occur in nematic liquid crystals, namely splay, bend and twist of the director (Figure 6).

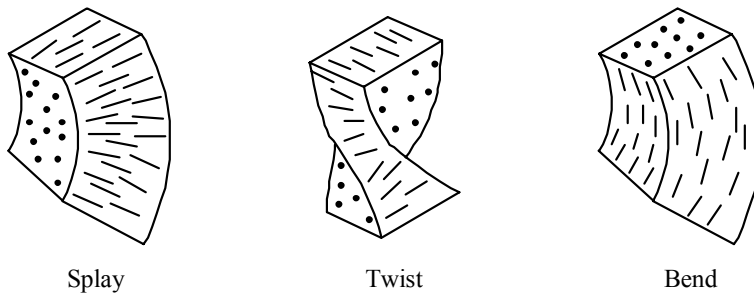Splay   Twist   Bend

Figure 6: Splay, twist and bend deformations of the nematic director.

Mathematically these may be expressed as:

Splay: div $\mathbf{n} \neq 0$

Bend: $\mathbf{n} \times \mathrm{curl}\ \mathbf{n} \neq 0$

9

Twist: $\mathbf{n} \cdot \text{curl } \mathbf{n} \neq 0$

The splay, bend and twist deformations have elastic constants k_{11}, k_{22} and k_{33} respectively [11] and these contribute to the free energy g as defined in Equation 6.

$$g = 1/2 \{ k_{11}(\text{div } \mathbf{n})^2 + k_{22}(\mathbf{n} \cdot \text{curl } \mathbf{n})^2 + k_{33}(\mathbf{n} \times \text{curl } \mathbf{n})^2 \}$$ *Equation 6*

In 1933, Frederiks *et al.* [12] showed that the energy of the system could be altered with a magnetic or electric field. An electric field $\mathbf{E}$ interacts with the dielectric permittivity anisotropy $\Delta\varepsilon$ to give an energy term $-\Delta\varepsilon/4\pi(\mathbf{E} \cdot \mathbf{n})^2$. The energy term is lowest when $\mathbf{n}$ is parallel to $\mathbf{E}$ for a material of positive $\Delta\varepsilon$, indicating a tendency for the molecules to align with the field. This effect is known as a *Frederiks transition* and occurs when the (threshold) field is large enough to overcome the relevant elastic forces. For nematics the threshold field is given [8] Equation 7.

$$E_0 = \frac{\pi}{d}\sqrt{\left(\frac{4\pi.k}{\Delta\varepsilon}\right)}$$ *Equation 7*

where $\mathbf{d}$ is the sample thickness and $\mathbf{k}$ (= k_{11} = k_{22} = k_{33}) is an assumed elastic constant representing all distortions. Thus the threshold voltage, V_{th} = $\mathbf{E} \times \mathbf{d}$, is independent of thickness. In the smectic system under investigation we consider a Frederiks transition from an initially planar, unidirectional state to a final homeotropic state (Figure 7).
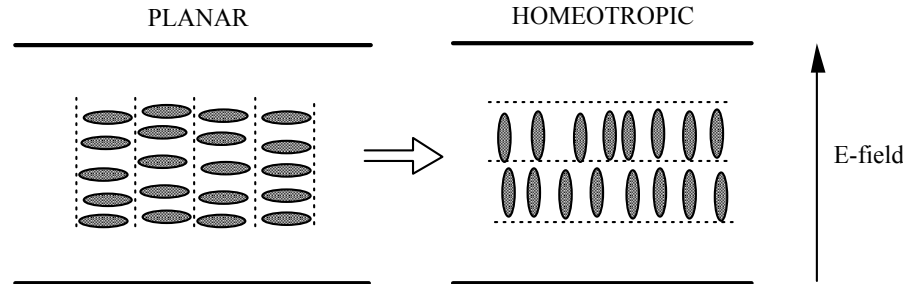

Figure 7: The planar-to-homeotropic transition in a smectic-A phase with positive dielectric anisotropy.

In 1972 Rapini [13] postulated the effect of a magnetic field applied across a planar smectic-A sample, so that $\mathbf{n} \perp \mathbf{H}$. The theory can be adapted to the case of an electric field interaction with the dielectric permittivity anisotropy (by substituting $\Delta\chi$ and $\mathbf{H}$ with $\Delta\varepsilon/4^1$ and $\mathbf{E}$ respectively). The electric field exerts a torque on the director that rotates $\mathbf{n}$ parallel to the field and lowers the energy. Surface anchoring restrains this motion below a certain threshold field, above which the sample would undergo a "ghost transition", meaning that, even at large fields the deviation would be very small (Figure 8). The reason for this was the assumption that the smectic layers were virtually incompressible. (Rapini did not account for defect generation due to surface forces.)
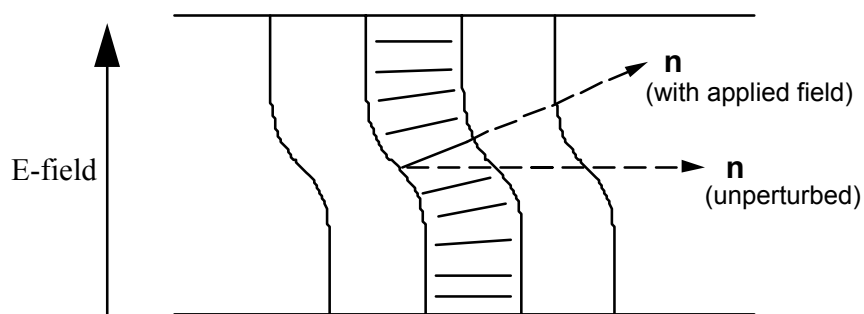
Figure 8: A "ghost" transition in a smectic-A material subjected to an electric field. Molecules are represented by sticks.

The effect of *electric* fields on smectic-A systems was first discussed in 1970, by Carr [14]. In the following year Tani [15] was the first to apply an electric field to convert a cell with focal conic domains, to a homeotropic texture. The next few years saw more switching theories and different experimental set-ups [13][16]. In 1972 Parodi [17] proposed a theory that incorporated the creation of defects. He proposed that a fully switched state would be reached for molecules in the bulk, leaving a defect structure within a penetration depth, λ, of the surfaces, as shown in Figure 9.
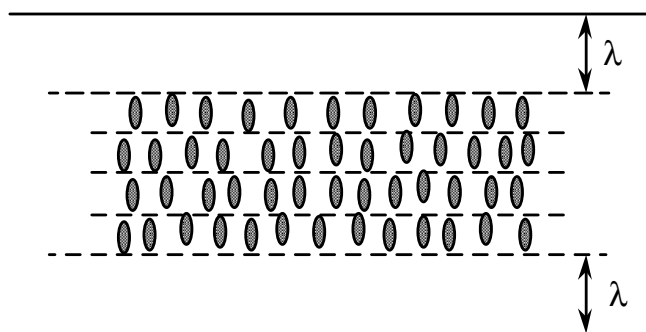
Figure 9: Quasi-homeotropic structure proposed by Parodi.

Parodi reasoned that the only energetically feasible defect was a periodic array of boundary grains (Figure 10). Above the threshold field Parodi predicted that the penetration would decrease with an increasing electric field as more layers overcame the surface forces.
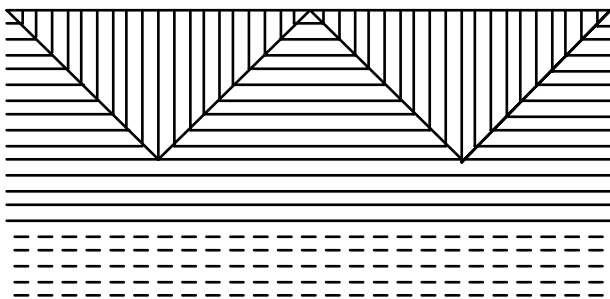

Figure 10: A "Parodi" array of boundary grain defects at one surface of a switched smectic-A material.

Such domain patterns were first observed in 1975 by Goscianski *et al.* [18]. The authors reported that after the defect pattern had appeared the central layers tilted with increased applied field, from an initial non-zero angle $\theta = \theta_c$ to $\theta = 90°$ in the fully switched position. Blinov [8] suggested that the discrepancy between theoretical and experimental values for the defect *period* might be due to the presence of chevrons in the smectic-A phase (see section 2.4.4).

Other smectic-A studies have been performed by Yoshino *et al.* (1975), Hareng *et al.*(1975), Rout and Choudhary (1989), and Jakli and Saupe (1992). Yoshino *et al.* [19] obtained response curves for the optical transmission as a function of time after voltage application. Hareng *et al* [20] looked specifically at defect structures formed during switching. (The defect structures mentioned in this chapter are described in more detail in Appendix A). For thick (50–100µm) cells Hareng *et al.* observed a toroidal focal conic domain (TFCD) in the sample centre when applying the field. The domain grew at larger applied fields, before forming a focal conic network and finally a quasi-homeotropic structure. Thin (10–20µm) cells were also examined but a detailed description of the intermediate structures was not given. The authors did not observe a Parodi defect array in either the thick or thin cells.

In 1989 Rout and Choudhary [21] investigated a 50µm planar sample. As the field was applied, neighbouring parabolic focal conics (PFCs) agglomerated before the sample became quasi-homeotropic. The authors describe the textures using a simple theory based on the work of Williams and Kléman [22] who proposed the existence of several defect structures in smectic-A. The relevant defect structures are shown in Figure 11.
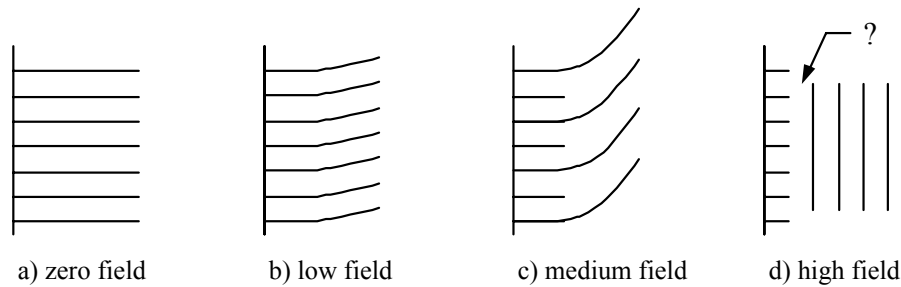

a) zero field　　　　b) low field　　　　c) medium field　　　d) high field

Figure 11: The planar-to-homeotropic switching process in a smectic-A material, as proposed by Williams & Kléman.

At low fields the layers bend. This is similar to Rapini's ghost transition except that it incorporates a region of surface layers that remains rigid. At medium fields the surface layer region thins and edge dislocations appear parallel to the smectic planes. In this model the defects emerge independently of one another.

In 1992 Jakli and Saupe [23] reported on the relaxation process when an electric field was removed from a sample with planar surface alignment. They observed a Parodi-type transition that agreed with an earlier paper by Hareng *et al.* [24] (the article concerned switching from a focal conic to a quasi-homeotropic structure). Regarding the texture they comment that "it started on the domain edges and propagated parallel to the smectic layers".

A summary of the smectic-A work reviewed in this chapter is given in Table 1.

Table 1: Summary of relevant studies of switching in smectic-A materials.

Reference	Comments
Rapini [13]	Theoretical. Bending of layers (ghost transition) at low fields.
Parodi [17]	Periodic array of defects (quasi-homeotropic).
Goscianski *et al*. [18]	Experimental paper, 20–290 μm cells. Parodi array observed. Non-zero initial layer tilt. Layers tilt towards 90° with increasing field.
Hareng *et al*. [20]	Experimental paper. Thick (50-100 μm) cells: Planar → TFCD's → expand → f.c network → q.homeo. Thin (10–20 μm) cells: Planar → f.c network → q.homeo
Rout and Choudhary [21]	Experimental, 50 μm cells. Planar PFC's → defect lines parallel to layers → non-periodic dislocation array → ellipses → TFCDs → q.homeo.
Jàkli and Saupe [23]	Experimental, 5–50 μm cells. Planar → defect lines parallel to layers → q.homeo. No mention of periodic array.

It is clear that smectic-A switching is a grey area, with different observations and deductions being made for similar processes. The Rapini model seems redundant; it has been superseded by a combination of the Parodi and Williams-Kléman models. Hareng's work suggests that the differences are partly due to the cell thickness. Maybe also the roughness and parallelism of the constraining plates must be taken into account, as well as the surface anchoring energy.

But there is a more fundamental problem, which is that smectic layers cannot actually be seen microscopically; only where defects occur can the configuration be deduced. This has several implications:

- If there are no defects or they are small, the layers cannot be "seen".

- Defect patterns are often ambiguous.

It was for these reasons that we decided to use the technique of x-ray diffraction to examine the smectic layers during switching.

The theory and review presented has focused on a planar-to-homeotropic transition. Several authors describe other switching possibilities ([10][16][25]–[34]).

2.4.3 Electro-optic measurements

Electro-optic measurements monitor the change in birefringence as a function of time, after a voltage has been applied to the sample [8]. The perceived birefringence comes from the molecular birefringence coupled with the director orientation. For plane polarised light incident on a sample, the transmitted light will, in general, be elliptically polarised.

Consider a uniaxial, birefringent system. On a molecular level the birefringence, Δn, is the difference in refractive indices along ($n_{//}$) and across ($n_\perp$) the optic axis. This value does not change with switching, although the perceived birefringence does change, giving electro-optic response curves. In the geometry shown in Figure 12 unpolarised light falls on the sample, in which the director is initially oriented along the x-axis.
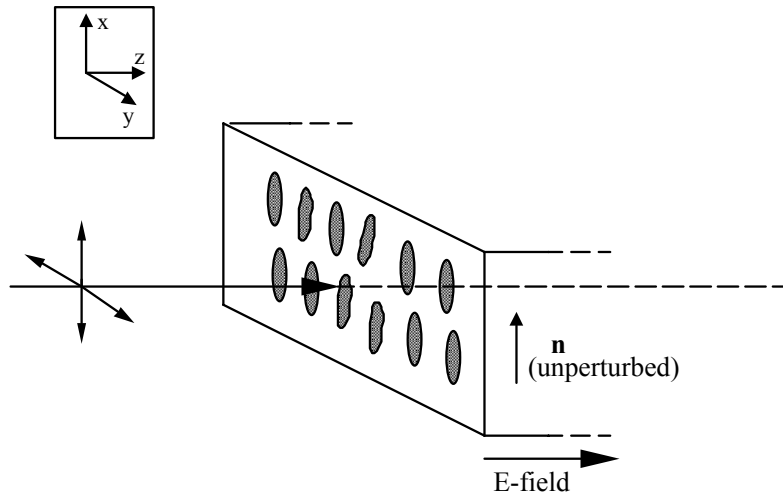

Figure 12: General geometry for discussion of birefringence.

The sample has bulk birefringence $\Delta n' = n_e - n_o$, where n_e and n_o are the refractive indices of the extraordinary and ordinary rays, which are polarised parallel and perpendicular to the system optic axis respectively. Before switching the perceived birefringence $\Delta n'$ equals the molecular birefringence Δn. When the director rotates, the system optic axis rotates and the polarisation direction of the extraordinary and ordinary rays change. This changing frame of reference makes the situation difficult to analyse. It is easier to consider the system as seen by rays polarised along the original e and o directions i.e. the frame of reference being the original director orientation (Figure 13).
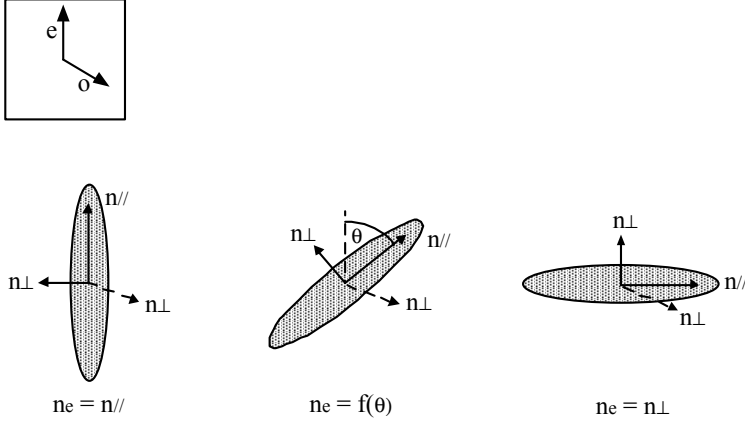
Figure 13: Change in refractive index component in the direction of polarisation of the extraordinary ray. In the fully switched state this component equals the "o" component and the perceived birefringence thus vanishes.

As the sample rotates the o-ray "sees" a constant refractive index $n_o = n_\perp$. The e-ray however sees an x-axis projection of the resultant vector formed by combining $n_{//}$ and $n_\perp$. This projection starts at $n_e = n_{//}$ and decreases as the sample switches, tending towards $n_e = n_\perp$. In other words n_e is a function of director orientation [8], and the perceived birefringence changes with angle, towards a value of zero in the fully switched state. If the incident beam is polarised in the x-direction the o-ray will be suppressed and the sample will no longer appear birefringent. A similar situation occurs if the incident beam is polarised in the y direction. Birefringence effects are only observed therefore when the director is at some angle to the incoming polarisation other than 0° or 90°.

Now consider an unswitched sample between *crossed* polarisers. E-rays and o-rays will traverse the sample along the same path, but travelling at different velocities. At the far edge of the sample they will, in general, be out of phase, the optical path difference being Δn'd, where d is the sample thickness. At this point the wave will in general be elliptically polarised and the component in the analyser direction will pass. As implied earlier the transmittance is maximised when the director is at 45° to the crossed polarisers. On application of an electric field to the sample Δn' will tend to zero. In a fully switched state the e and o rays thus recombine in phase, leaving the polarisation unaltered on leaving the sample. The emerging ray will thus not pass through the analyser and the output will be dark. A typical electro-optic response is shown in Figure 14.
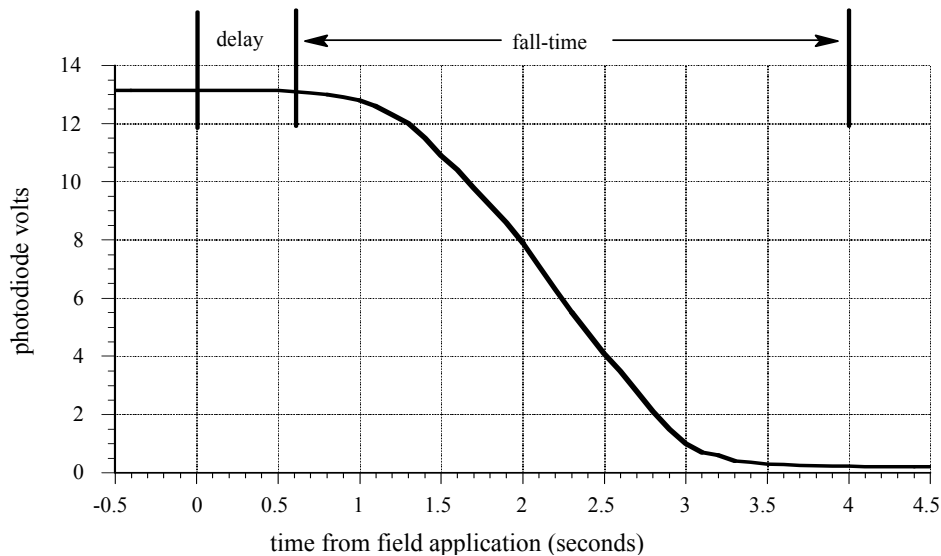
Figure 14: A typical electro-optic response curve for smectic-A switching.

A delay (indicating for example, defect pinning), might be observed between the application of a voltage to the sample and the first optical response. The fall time depends on director motion and is affected by the viscosity and elastic constants of the material [11]. The shape of the curve indicates the director orientation as a function of time.

Although birefringence effects dominate, there can be an increase in transmitted light intensity because scattered light contains a spread of polarisation directions, a proportion of which will pass through the analyser to the detector. The final response is a convolution of birefringence and scattering.

Unusual two-stage switching curves have been observed in polymeric systems [35]. It has been hypothesised that the two stages are the manifestation of different time-scales for layer and director responses. **The desire to investigate such two-stage switching processes was our initial reason for performing the research described in this thesis.**

2.4.4 Planar smectic-A layer structures

In 1987 Rieker *et al*. showed that chevron structures were commonplace in thin smectic-C cells [36]. Until then it had been assumed that the molecules in planar aligned smectic-C cells would sit in layers that were perpendicular to the cell walls, forming the so-called *bookshelf* structure (see section 2.5.3.2).

Chevrons form due to the increase in tilt angle of the smectic-C director and the subsequent reduction in layer thickness. In a smectic-A phase however, the molecules are perpendicular to the layer normal at all times. There is no tilt angle variation, and it was believed therefore, that there could be no layer thinning either. It has thus been assumed that the smectic-A layers adopt the bookshelf structure as shown in Figure 15.
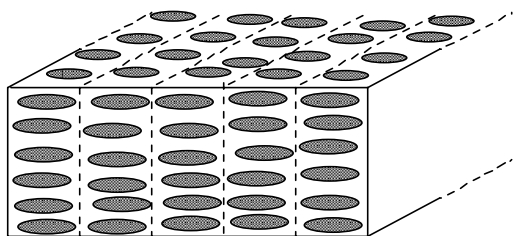
Figure 15: Bookshelf smectic-A structure.

In 1989 this assumption was proved to be false for some smectic-A materials, when Takinishi *et al.* [37] demonstrated the first experimental evidence of chevrons in the smectic-A phase. They showed that the formation of chevrons was due to thermal contraction of the layers [38]. In addition to zigzag defects (see section 2.5.3.3), parabolic focal conic defects (see appendix A) were observed due to excessive local strain in the sample caused by the chevron structure.

Limat and Prost [39] subsequently proposed a model for chevron formation incorporating cell thickness, temperature, anchoring strength, elastic constants and layer compressibility. Kralj and Slukin [40] proposed an extension of this theory in terms of the orientational order parameter and the smectic order parameter.

2.5 Theory of Ferroelectric Liquid Crystals

2.5.1 Introduction.

The theory presented here concerns chiral smectic-C materials, although other ferroelectric phases are known [10]. Note that references in this section of the text to *polarisation* refer to the electronic polarisation vector, not to the polarisation of light.

2.5.2 Ferroelectricity in the chiral smectic-C phase

A ferroelectric material shows spontaneous polarisation in the absence of an external field. Such a material shows hysteresis in the electronic polarisation produced by an electric field, i.e. the polarisation is not uniquely determined by the applied electric field but depends on previous values.

In a single layer of the chiral smectic-C phase, the molecules tilt at an angle θ (known as the tilt angle) with respect to the layer normal. If the molecules have a fixed dipole along the short axis of the molecules, the helix can be unwound (with a suitably applied electric field) to produce a spontaneous polarisation Ps across the bulk of the phase [10]. In such a situation the molecules lie on the same portion of a cone of possible directions. The polarisation couples to an electric field so that when the field direction is changed the polarisation changes direction due to the torque between it and the applied field. The molecules switch through an angle of 2θ when the electric field is reversed.
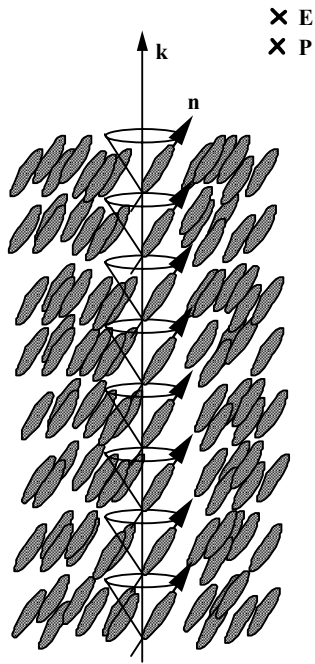
Figure 16: Suppression of the helix in the chiral smectic-C phase, using an electric field. The field E, and the net polarisation P, are directed into the plane of the paper.

The helix can also be unwound using strong surface alignment on the cell walls; this gives a "Surface Stabilised Ferroelectric Liquid Crystal" (SSFLC) [10]. Such cells need to be thin to suppress the helix in the centre of the cell. The typical thickness is about half the helical pitch, i.e. 1-5µm in commercially available samples. SSFLC structures generally adopt either the bookshelf geometry or the chevron geometry, depending on the phases present in the liquid crystal and on the thermal and electrical history of the cell.

There are two different tilt angles: The *optical* tilt angle is the angle between the layer normal and the optic axis. (The rigid molecular core is the main contributor to the optical axis.) The *molecular* tilt angle is the angle between the layer normal and the long molecular.
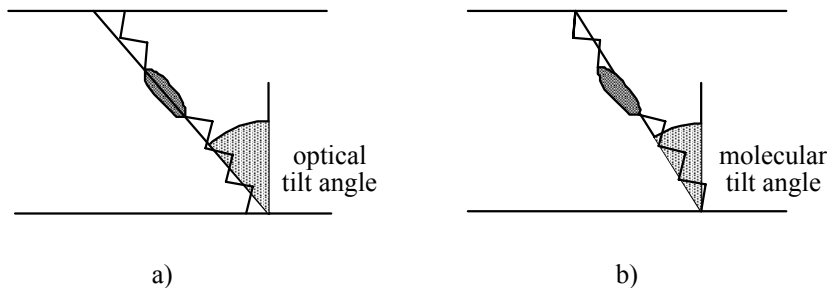

Figure 17: The optical (a) and molecular (b) tilt angles.

For this thesis the slight difference between the molecular and optical tilt angle is irrelevant and the term "tilt angle (θ)" is used to mean both. Depending on the direction of optical observation an *apparent* tilt angle might be observed.

In the absence of an externally imposed bias, the tilt angle is not restricted in azimuthal direction but is defined by a cone of possible orientations in such a way that the cone axis is normal to the layers. The tilt angle θ makes small fluctuations about its thermodynamically determined value (changes require layer compression or dilation and thus considerable energy). This fluctuation is called the Soft mode. Thermal fluctuations in the azimuthal angle φ, around the cone are much larger and easily excited. This motion is called the Goldstone mode (Figure 18).
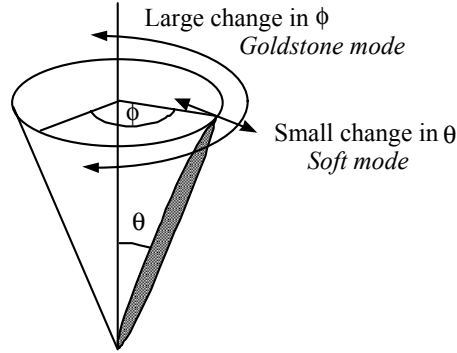

Figure 18: The excitations of the smectic-C phase.

Due to rotational bias of the long molecular axis, the direction of the spontaneous polarisation, for a given tilt angle, depends on φ and is such that it is tangent to the cone base at the point where the director touches, as shown in Figure 19.
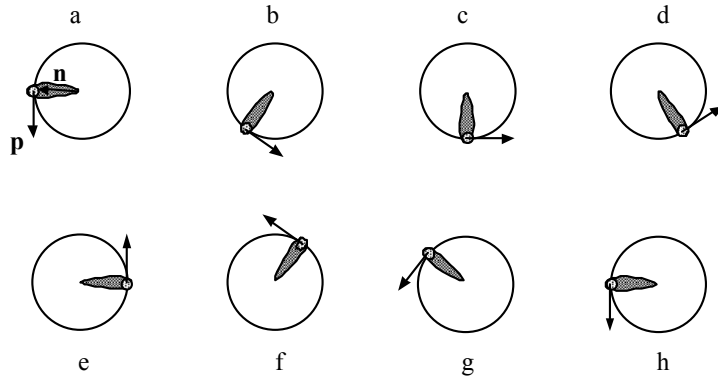

Figure 19: A projection of the cone base showing the coupling between the polarisation direction and the director orientation (azimuthal angle).

Thus the director **n** and the unit molecular polarisation **p** are intrinsically related. They are referred to as the **n-p** couple.

2.5.3 Surface stabilised ferroelectric liquid crystals (SSFLCs)

2.5.3.1   Introduction

In the first demonstration of a SSFLC cell [41] it was presumed that the layers were

perpendicular to the cell faces. Such a structure is called a bookshelf structure (Figure 20).
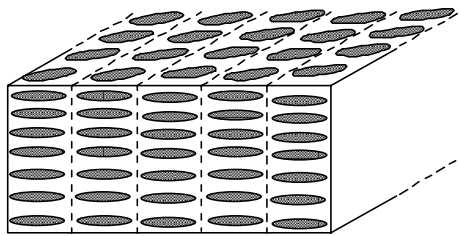

Figure 20: The (chiral) smectic-C bookshelf structure.

With later x-ray experiments [36] it became clear that in most cases a chevron structure emerges, as shown in Figure 21.
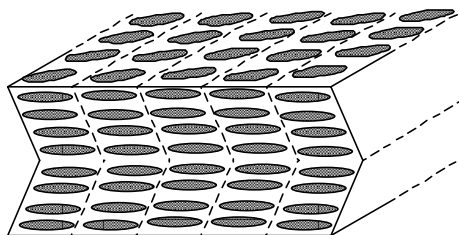

Figure 21: The (chiral) smectic-C chevron structure.

2.5.3.2   The SSFLC bookshelf structure and its response to electric fields

In the simplest configuration the director is everywhere parallel to the surface and the polarisation is either UP or DOWN as shown in Figure 22.
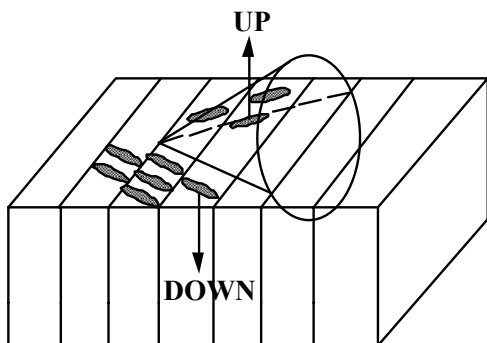

Figure 22: Simple director configuration in the bookshelf SSFLC.

An unswitched sample will generally exhibit both UP and DOWN regions, separated by a domain wall (Figure 23) [41], which effectively rotates the **n-p** couple by 180°.
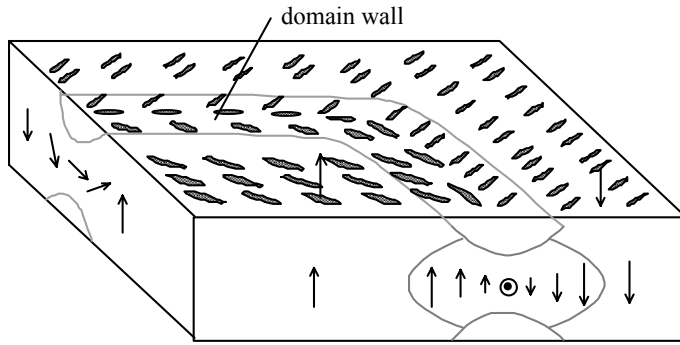
Figure 23: UP and DOWN regions separated by a domain wall. The arrows represent the polarisation. A decreasing arrow size symbolises a rotation of polarisation out of the vertical plane.

When an electric field is applied across the cell to switch molecules into (for example) an UP state the domain walls move accordingly, reducing the size of DOWN regions. The domain wall velocity is different in different directions [42]. At large values of E the director can rotate homogeneously throughout the sample, without the need for domain wall mediation. The characteristic response time, for ferroelectric switching is given by equation 2.11.

$$\tau = \frac{\gamma}{P.E}$$

Equation 8

where γ is the orientational viscosity. Response times are typically of the order of microseconds [10]. Polar surface interactions can cause the director profile within the cell to adopt various configurations, with complex switching possibilities [43].

2.5.3.3   The chevron structure

When cooling from a smectic-A phase to a chiral smectic-C phase an increasing tilt angle means that the layer thickness d must decrease. Surface anchoring however, strongly binds the surface layers, fixing their length. The result is that the layers rotate so that the layer normal tilts around the director and not vice versa. The layer tilt angle δ is related to the smectic-A layer thickness d_A and the smectic-C layer thickness d_C, as shown in Equation 9 [44].

$$d_C(T) = d_A.\cos(\delta(T))$$

Equation 9

To preserve the strong anchoring condition at *both* surfaces for the same layer, a chevron structure emerges (Figure 24). The structure is usually symmetric although an asymmetric structure will arise if the preceding S_A phase is tilted [44]. In each half of the chevron structure the switching cones tilt along with the local layer normal. At the chevron apex the director can only sit where these cones overlap. If $\delta < \theta$, there are two possible director orientations (U and D in Figure 24). The device is thus bistable. The width of the chevron apex is typically of the order of 100Å or less [45] i.e. it is abrupt.
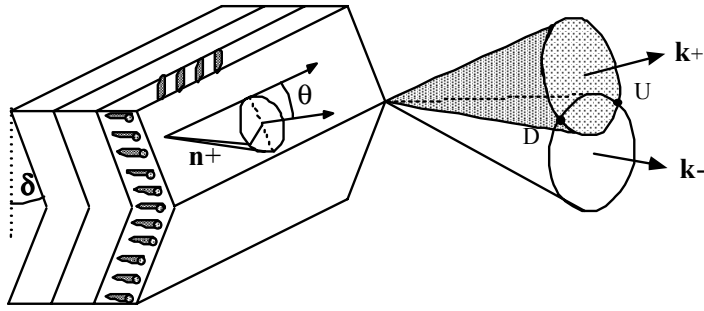
Figure 24: Stable director orientations, D and U, at the chevron interface. The + and - suffices refer to the top and bottom arms of the chevron respectively. The polarisation at D is nearly down and at U it is nearly up.

Strong polar surface interactions can lead to a number of director configurations and subsequent switching schemes [10]. Figure 25 shows for example, what is known as the triangular director profile (from [46]).
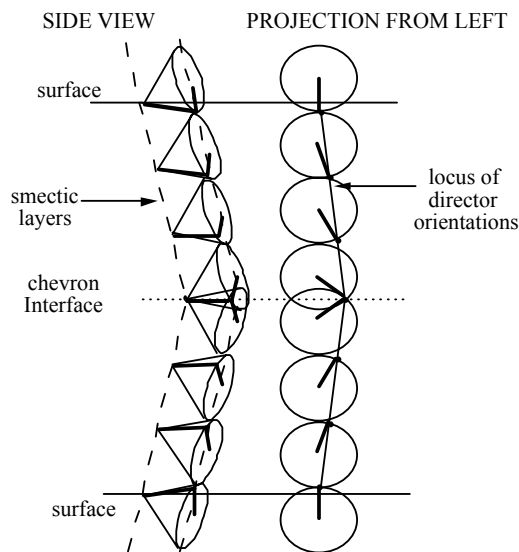
Figure 25: The triangular director profile. The projections are taken along the cone axes.

The choice of chevron direction is arbitrary, so that a given sample will have regions of each. These regions are separated by the zigzag defect. The zigzag defect is clearly visible between crossed polarisers when looking down onto the cell face, as shown schematically in Figure 26.

Figure 26: Schematic diagram of a zigzag defect loop, showing the background director.

The defect consists of a loop, within which the chevron structure points in a unique direction. At one end of the loop a narrow-walled zigz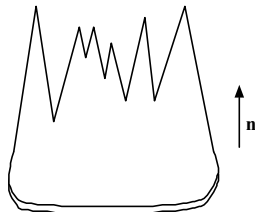ag structure signifies chevrons pointing away from one another. At the other end of the loop a broad wall signifies chevrons pointing towards one another. Zigzag defects can be removed by applying high electric fields.

2.5.3.4   Application of LOW electric fields to the chevron structure

The word *low* signifies that the electric field is sufficiently high to switch the director but not the layers. During switching the director must overcome the energy associated with both the chevron interface and the surfaces.

At high fields (within the *low* regime) the directors above and below the chevron interface can homogeneously decouple and switching occurs without the need for domain wall motion [10]. The directors above and below the chevron interface rotate around the cone in opposite directions. At lower fields decoupling is not possible. "Holes" however, may nucleate at defects and spread, so that domain walls begin to move within the plane of the chevron apex. The chevron interface switches as a domain wall passes [10].

Recent theories ([47] and [48]) suggest that switching involves motion of the layers (not just the local director), due to a coupled layer–director model. The model assumes that the director configuration in a chevron cell is not splayed, as portrayed by Reiker [44], but that the director orientation remains constant throughout the cell; the orientation being defined by the chevron apex condition (Figure 24). In Hartmann's model the director remains in position even while rotating about the cone during low-field switching. It achieves this due to a "wobble" of the layers. As the director switches around the cone from (say) an UP state to a DOWN state, the chevron interface bends initially to a higher tilt before relaxing back (Figure 27). In this way it facilitates continuous director motion. Hartmann suggested that the change in chevron angle would be of the order of 1°.
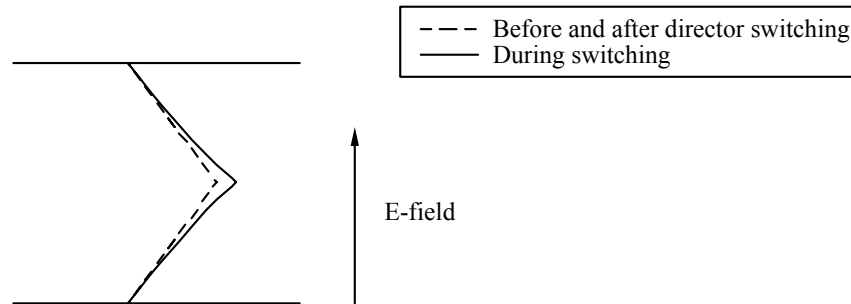

Figure 27: Layer motion during ferroelectric switching.

MacGregor proposed a similar model [49], in which the director is not necessarily planar but nevertheless remains stationary with respect to the substrates during switching. Giesselmann *et al.* [48] performed electro-optical experiments which were analysed on the basis of a modified Hartmann model. They measured the in-plane and out-of-plane director orientation during switching and concluded (for a switching field of 1V/μm) that the director does indeed remain constant while the layers "wobble". They also showed that the director moves considerably out-of-plane during switching after E.F.T, as would be expected.

2.5.3.5   Application of HIGH electric fields to the chevron structure

The first observations of smectic layer motion due to electric fields, were made by Johno *et al.* in 1989 [50]. Measurements were made in the antiferroelectric phase of MHPOBC[1]. They observed an irreversible change from a chevron structure to a bookshelf structure, on application of a large D.C field. The threshold for layer motion was 3.5V/μm and that full conversion to a full bookshelf structure was obtained with a field of 9V/μm [51].

Layer changes have since been observed in many chevron structures ([48][52]–[66]) typically with fields between 6V/μm and 15V/μm. The mechanism for the deformation is the same ferroelectric torque that drives the director switching. As Figure 24 demonstrates, the spontaneous polarisation in a chevron structure can switch between states that are nearly UP and nearly DOWN. The electrostatic energy of such a system can be lowered further by rotating the P_S even more. This can be achieved by rotating the hypothetical cone axis, which is equivalent to rotating the layers. Such a rotation is hindered by the energy needed to overcome layer thickness changes, and by the anchoring energy associated with the substrates and with the chevron apex. Patel *et al.* [67] proposed that the surface anchoring energy could be overcome by layers slipping at the surface and re-growing at an angle ψ to the original layer normal, as shown in Figure 28.
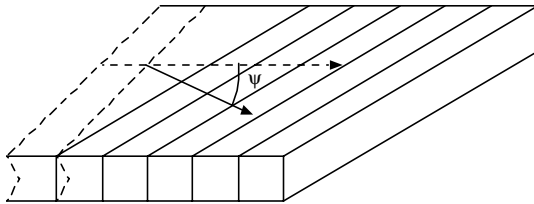

Figure 28: The change in layer orientation with E.F.T.

The angle ψ would increase from 0° to approximately the tilt angle, as the internal structure changed from chevron to bookshelf. The hypothesis was confirmed by microscopic observation [53]. It was seen that the sense (+/-) of ψ could change on crossing the cell face, giving rise to a "surface chevron" structure (Figure 29).
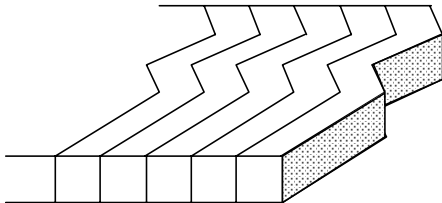

Figure 29: Emergence of a surface chevron structure due to E.F.T.

There has since been a lot of research on the technical aspects of structural changes because of the potential enhancement of displays [8]. (Appendix B will aid the reader with following text.)

Nearly all x-ray diffraction experiments concerning E.F.T have been single axis rocking experiments, obtained with a 1D detector. In such cases the sample has been pre-rotated to bring

---

[1]4-(1-methylheptyloxycarbonyl) phenyl 4'-octyloxybiphenyl-4-carboxylate [MHPOBC]

the initial surface layers parallel to the rocking axis. There have been only a few experiments in which full 2D rocking has been performed [54] [68], notably that by Srajer *et al.* [54]. In the case of the 1D experiments the pre-E.F.T rocking curves generally show two sharp peaks, at angles of approximately +/- 20° to the layer normal, indicating the presence chevrons. On application of an increasing field the chevrons gradually disappear. The rocking curve peaks generally become wider and approach 0°, indicating a conversion to a low tilt obtuse chevron structure (e.g. [55]). If the applied field is large enough a central peak emerges on the rocking curve, indicating the formation of bookshelf-type features. These may coexist with chevron features [56] or may become the solitary diffraction feature [50]. Typically on field removal, a deformed structure relaxes reversibly to a low tilt obtuse chevron structure [55][57].

The 2D rocking experiment of Srajer *et al.* provided additional information: It showed that the surface layer normal can change, forming a surface-chevron structure as discussed previously. Furthermore the diffraction peaks indicate that the surface-chevron is quite sharp. The implication of this for 1D rocking experiments is that the post-E.F.T bookshelf structure should not give diffraction peaks at any angle unless the cell is "pre-rotated" once more, so that the surface layers are again locally parallel to the rocking axis (see Appendix B). In none of the 1D rocking experiments has this been done. Thus, based on the surface-chevron picture, it is unclear why the final bookshelf-type features can be seen in the 1D rocking experiments. **It was our intention to use a 2D x-ray detector to help clarify this issue.**

The most striking feature of E.F.T is the change in the defect texture, when viewed between crossed polarisers. On increasing the applied field the zigzag defects of the chevron structure slowly disappear and a new defect textures appears: the shallow field line defect [61], the steep field line defect [61] and the stripe defect [62]. The stripe defect contains chevron regions and bookshelf regions, as seen in Figure 30. On continued application of the field the bookshelf regions grow, at the expense of the chevron regions.
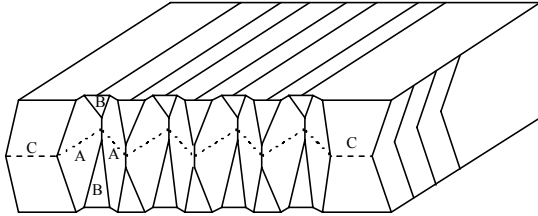
Figure 30: Formation of the stripe-defect with E.F.T. A and B represent emerging bookshelf and remaining chevron areas respectively. C represents the chevron structure before electric field application.

There have been several articles on the characterisation of post-E.F.T structures ([52][63][65]–[71]). Nagao *et al.* [63], for example, showed that the apparent optical tilt angle could be controlled by performing E.F.T at different temperatures.

Chapter 3

X-RAY THEORY

3.1 X-ray Diffraction Intensities

In smectic-A liquid crystals the electronic distribution across a layer is not exactly the same as that along a molecule, due to structural smearing caused by thermal motion. To a first approximation the layers form a sinusoidal density wave along the layer normal axis. The smectic order parameters indicate the extent of smearing. The parameters are related to the relative intensities of the meridianal peaks [72].

3.2 X-Ray Diffraction Patterns

3.2.1 Reciprocal space and the Ewald sphere construction

The Ewald sphere construction can be used to determine the expected diffraction Figure 31).
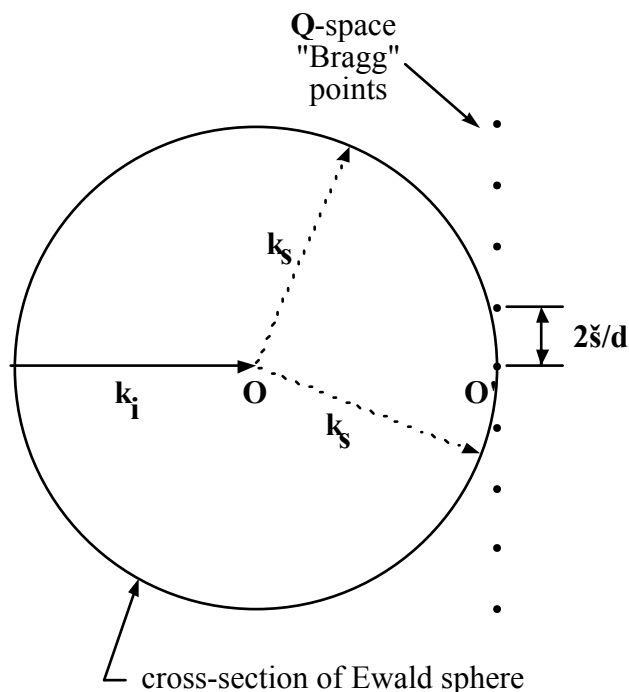
Figure 31: The Ewald sphere construction. All elastically scattered wavevectors must end somewhere on the sphere surface. This figure shows two of these wavevectors.

The sphere is centred at the sample position, O, and its radius is the magnitude of the incident wave vector (it does not depend on the sample). For elastic scattering, any scattered wave vector

k_s must end somewhere on the surface of the sphere and this means Q must do also. Now I(Q) provides the scattered intensity for all Q throughout Q-space, regardless of whether or not those Q values are actually obtainable. For a one-dimensional crystal it can be shown [72] that the diffracted intensity distribution I(Q) is a series of "Bragg" spots. In general these spots do not touch the surface of the Ewald sphere and will not therefore give rise to any diffraction. However, the sample can be tilted so that the Q-vector of interest touches the Ewald sphere. Figure 32 shows for example, how the sample might be tilted so that the second order (n=2) diffraction spot gives observable diffraction. This tilting is known as rocking (see Appendix B).
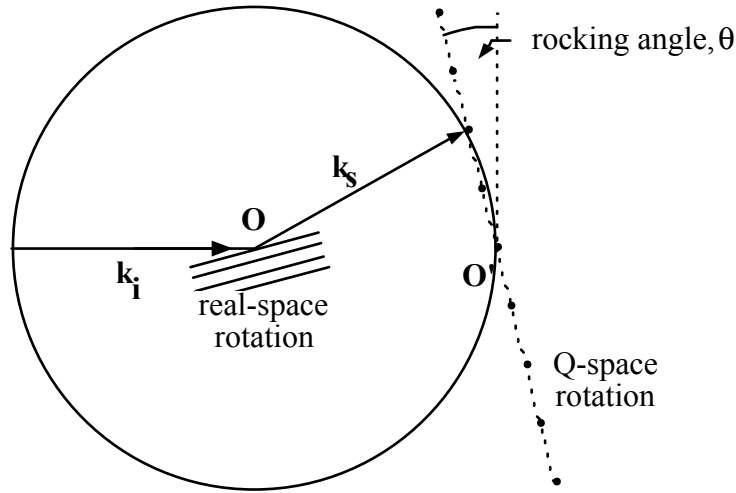

Figure 32: Rocking a 1D crystal to bring the Bragg spots onto the Ewald sphere.

If the periodicity is sufficiently large then low angle diffraction spots effectively "see" the Ewald sphere as a flat surface. They will thus touch it without the need for rocking.

Bragg's Law

Simple trigonometry applied to Figure 32 shows that;

$$|Q| = \left(\frac{4\pi}{\lambda}\right) sin(\phi/2)$$

Equation 10

Substitution into Equation 10 gives the condition for interference from a 1-D crystal, Bragg's Law:

$$n\lambda = 2dsin\theta_B$$

Equation 11

where $\phi/2$ is also known as the Bragg angle, θ_B.

The layer reflection model also gives a convenient way of looking at diffraction. In the model (Figure 33) x-rays strike parallel layers and give Bragg scattering only when the scattered angle is a Bragg angle. Furthermore the angle of incidence must equal this angle of scattering. This is known as the Bragg condition. Pictorially the situation may be envisaged as reflection from surfaces and the term "Bragg reflection" is thus sometimes used.
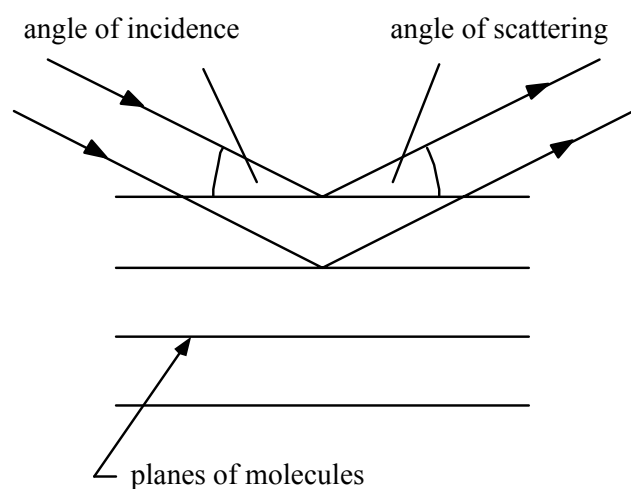
Figure 33: Bragg diffraction

3.2.2 Diffraction patterns for different types of translational order

Different types of translational order will give different diffraction patterns. A schematic review is presented overleaf. The distance r is measured in just one direction and so, therefore, is I(Q). Q is thus replaced by the modulus, Q.

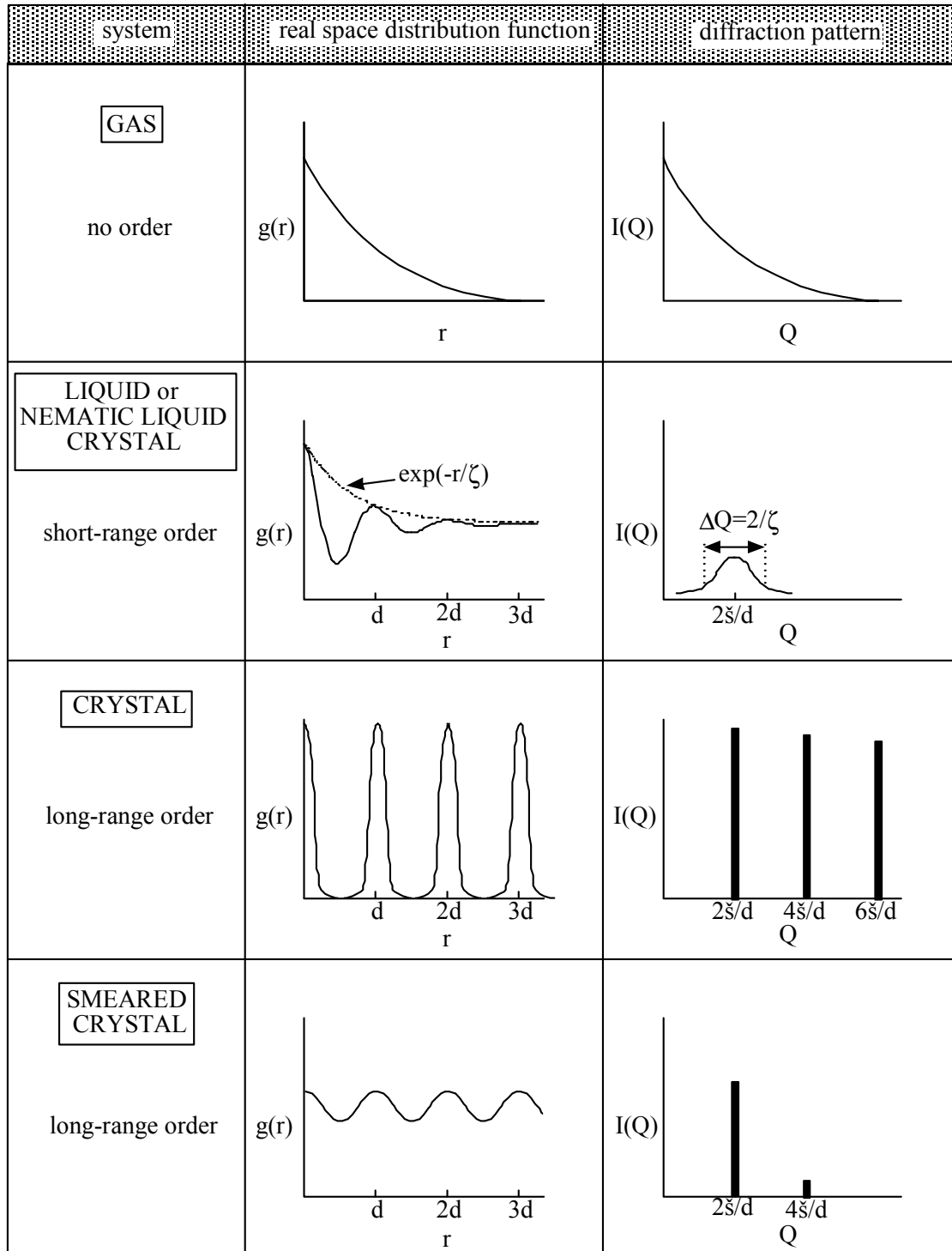| system	real space distribution function	diffraction pattern
GAS no order	g(r) curve decaying, axis r	I(Q) curve decaying, axis Q
LIQUID or NEMATIC LIQUID CRYSTAL short-range order	g(r) with exp(-r/ζ) envelope, damped oscillations, marks d, 2d, 3d, axis r	I(Q) broad peak, ΔQ=2/ζ, at 2š/d, axis Q
CRYSTAL long-range order	g(r) sharp peaks at d, 2d, 3d, axis r	I(Q) sharp peaks at 2š/d, 4š/d, 6š/d, axis Q
SMEARED CRYSTAL long-range order	g(r) damped oscillations at d, 2d, 3d, axis r	I(Q) peaks at 2š/d, 4š/d, axis Q

Figure 34: A schematic review of the diffraction patterns for different types of translational order. ζ is the positional correlation length.

A sample that possesses only one dimension of crystallinity, such as a smectic liquid crystal, has in fact only quasi long-range order. The distribution function is pictured overleaf (Figure 35).

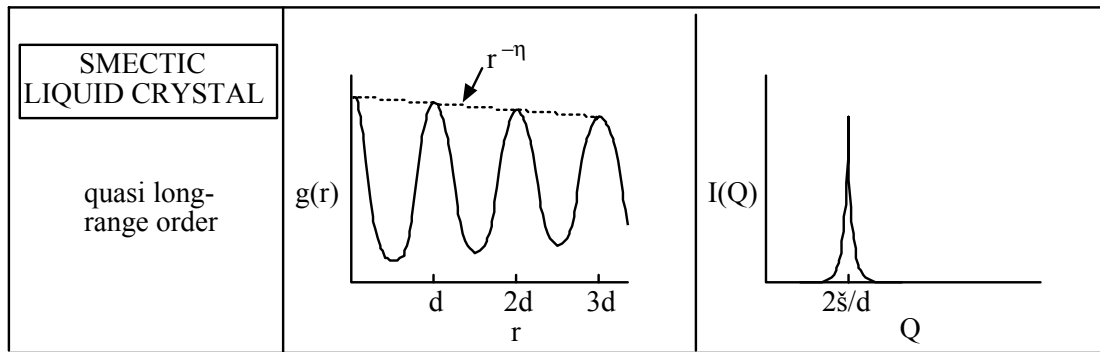| SMECTIC LIQUID CRYSTAL		
quasi long-range order	$g(r)$	$I(Q)$

Figure 35: Schematic illustration of quasi long-range order and its associated diffraction pattern. η is a temperature-dependent factor related to elastic properties of the material.

Translational order is slowly lost on moving away from a reference site because of thermally-excited fluctuations in the sample [73]. Its effect is to give "wings" to the Bragg spots so that they are no longer delta functions but weaker singularities. In practise this spread cannot be resolved and the integrated intensity in the region is the same as that from a true Bragg peak.

3.2.3 Diffraction from unaligned liquid crystals

An unaligned liquid crystal is similar to a crystal powder in that its Q-space diffraction is spherically symmetric and the intersection with the Ewald sphere thus has circular symmetry. Such a pattern gives less information than an aligned liquid crystal but has the advantage that the sample does not need to be rocked to see diffraction. This is because, for a given magnitude of Q there is always a vector Q which touches the Ewald sphere. The pattern at the detector consists of a series of concentric circles. Diffuse circles reflect the short-range order and sharp circles reflect the quasi-long-range order. Circle radii on the detector can be converted to scattering vectors (or Bragg angles) by simple trigonometry (Figure 36).
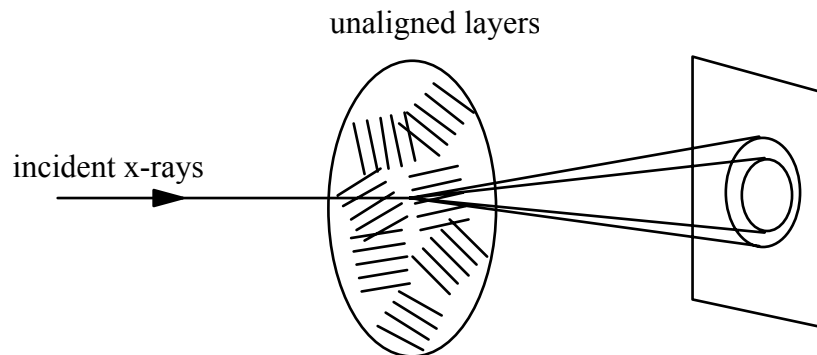

Figure 36: Diffraction from unaligned liquid crystals.

3.2.4 Diffraction from aligned liquid crystals

More information is obtainable from aligned liquid crystals. The diffraction patterns of nematic liquid crystals are usually referenced with respect to the Q-space axis parallel and perpendicular to the global director. These axes are called the meridian and equator respectively.

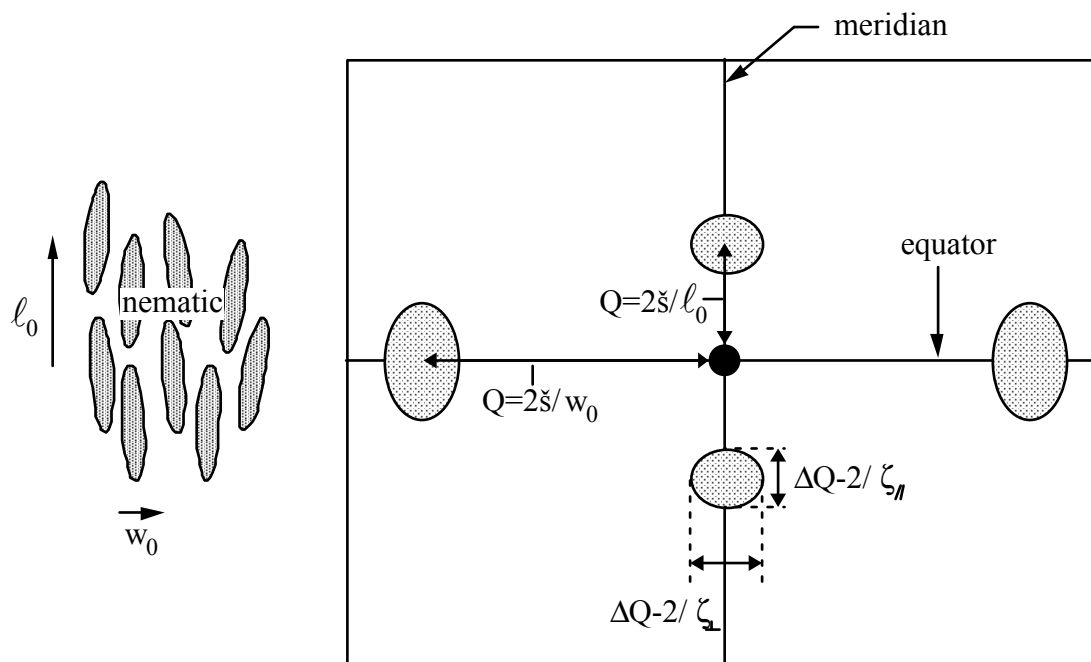### *3.2.4.1 Diffraction from nematic liquid crystals*

Figure 37: The diffraction pattern of an aligned nematic liquid crystal.

The figure shows the diffraction pattern from an aligned nematic phase. The central black spot represents the point at which the undeviated beam strikes the detector (in practise this is prevented by using a lead beamstop). The uniaxial symmetry of the phase means that rotating the sample around the director axis has no influence on the pattern. The low-angle diffuse peaks on the meridian reflect the average end-to-end separation of the molecules. The peak centres are located close at $Q = 2\pi \div l_0$, where l_0 is the molecular length. The wide-angle diffuse peaks on the equator reflect the average side-to-side separations and are centred close to $Q = 2\pi \div w_0$, where w_0 is the molecular width[2]. The meridional spot dimensions give the correlation lengths parallel to and perpendicular to the director. The equatorial width of the wide-angle diffuse peaks also gives the correlation length perpendicular to the director. In real systems it is usual to see patterns such as the one in Figure 38.

---

[2] The value is usually midway between maximum and minimum lateral dimensions of the molecule [11].
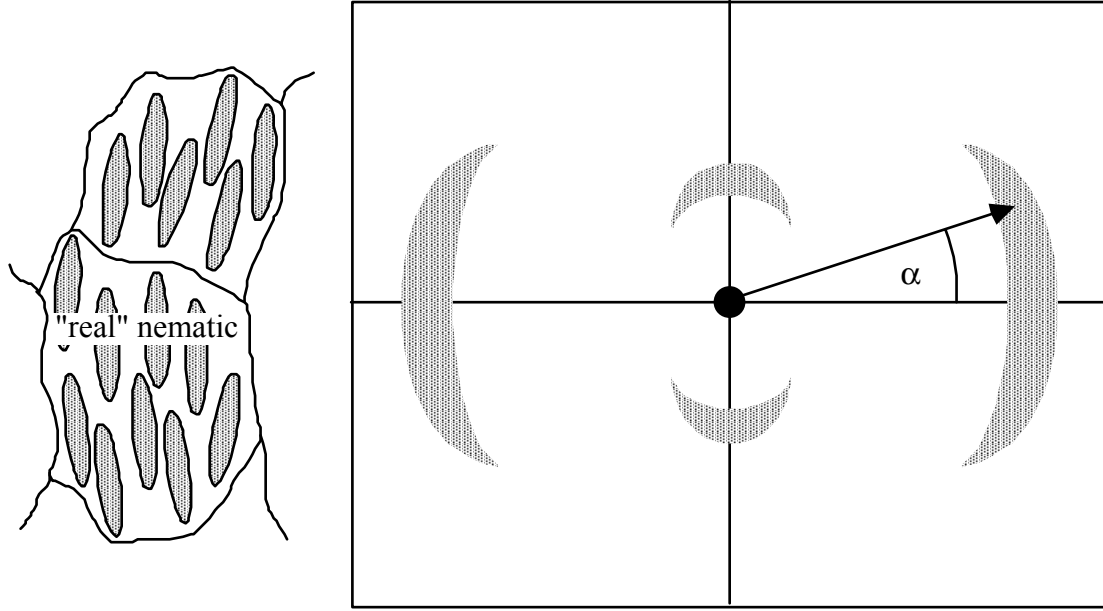
Figure 38: The diffraction pattern from an aligned, non-ideal nematic liquid crystal.

The extent of peak arcing is reciprocally related to the orientational order parameter. The arcing is also related to the spread of directors in a multi-domain sample i.e. to the mosaicity. In practice the mosaicity distribution function is similar to the orientational distribution function [74]. This assumption simplifies determination of the single domain orientational distribution function f(§). The intensity variation around the wide-angle arc is related to f(§) as given by Equation 12 [74]:

Equation 12

$$I(\alpha) = \int_{\beta}^{\pi/2} sin\beta . f(\beta). \sec^2 \alpha . (tan^2\alpha - tan^2\beta)^{1/2} . d\beta$$

f(§) can be solved by trial and error substitution of anticipated distributions. Once f(§) is obtained extracting orientational order parameters is straightforward [74].

3.2.4.2   Diffraction from smectic-A liquid crystals

On cooling an aligned nematic into the smectic-A phase the diffuse meridional peaks sharpen into a small number of equally-spaced Bragg peaks at $Q = 2\pi n \div l_0$ (Figure 39).
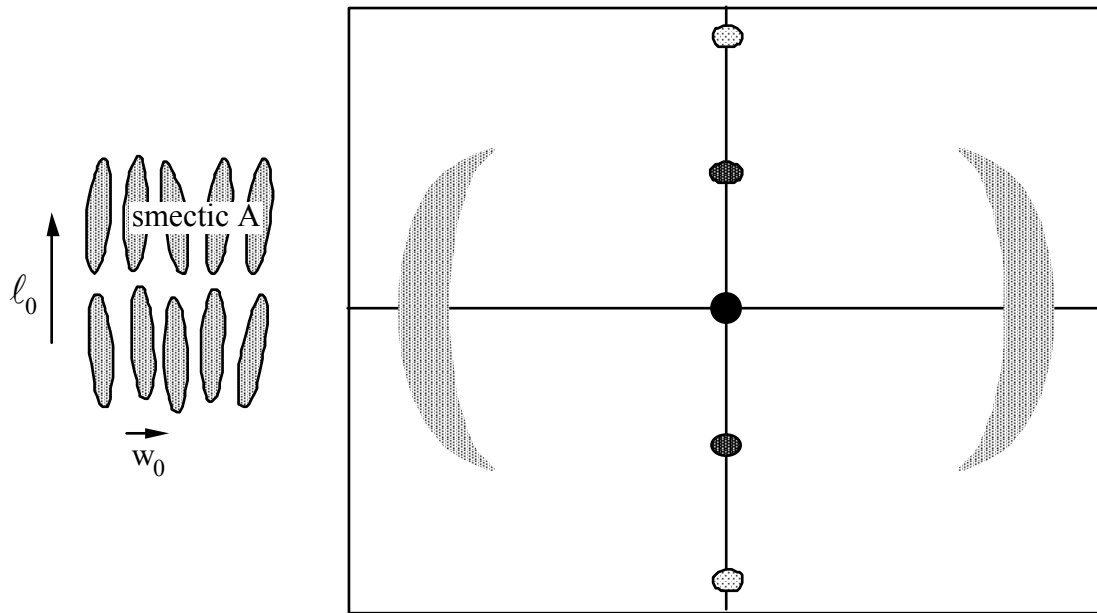
Figure 39: The diffraction pattern from an aligned smectic-A liquid crystal. In practice individual spots may only appear when the sample is rocked.

Simple trigonometry (Equation 11) enables one to deduce layer spacing. The intensity of the second order peaks is typically 10^{-3} times that of the first order peaks. These and higher order spots may thus not be seen. As previously described, the ratio of peak intensities can be measured to obtain the smectic order parameters. The other obtainable information is the same as that for an aligned nematic material. In addition, rocking the sample can give information on the layer geometry. If the orientation of the constraining surfaces is known (relative to the incident beam direction) then it is easy to determine the orientation of the layers with respect to these surfaces.

3.2.4.3   Diffraction from smectic-C liquid crystals

The geometry of an aligned smectic-C phase depends on the particular alignment mechanism. If, on cooling into the phase, the layers are anchored then the situation shown in Figure 40a results. If the director is anchored then the situations shown in Figure 40b or Figure 40c result. The most usual occurrence is director anchoring i.e. b) or c). This is the case for the experiments reported in this thesis. The information obtainable from the pattern is almost the same as that from a smectic-A. The only additional information is the tilt angle, which can be measured directly from the diffraction pattern, as shown overleaf in Figure 40b.
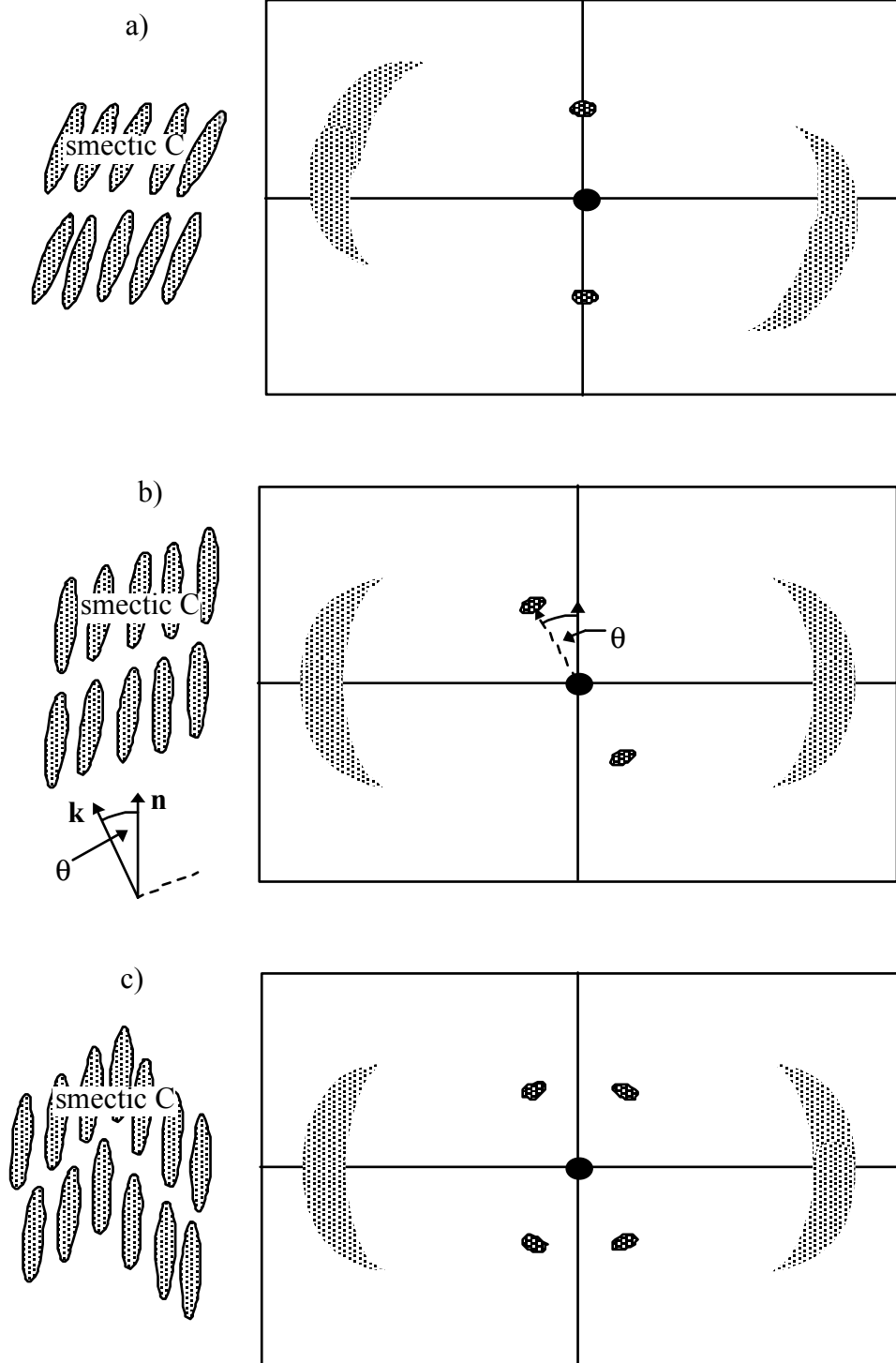
Figure 40: Smectic-C configurations and their diffraction patterns. The tilt angle θ is shown in (b).

3.3 Properties of Synchrotron Radiation

Synchrotron radiation is the radiation produced by accelerating charges as they attain relativistic speeds. The radiation of electromagnetic waves by an accelerating charge is a well-known classical effect [75]. At non-relativistic speeds this radiation is emitted from the charged body in all directions, represented by a toroidal flux density distribution. As the charge speed becomes relativistic the radiation is emitted only in the direction of travel of the charge. Synchrotron radiation is harnessed in storage rings (Figure 41).
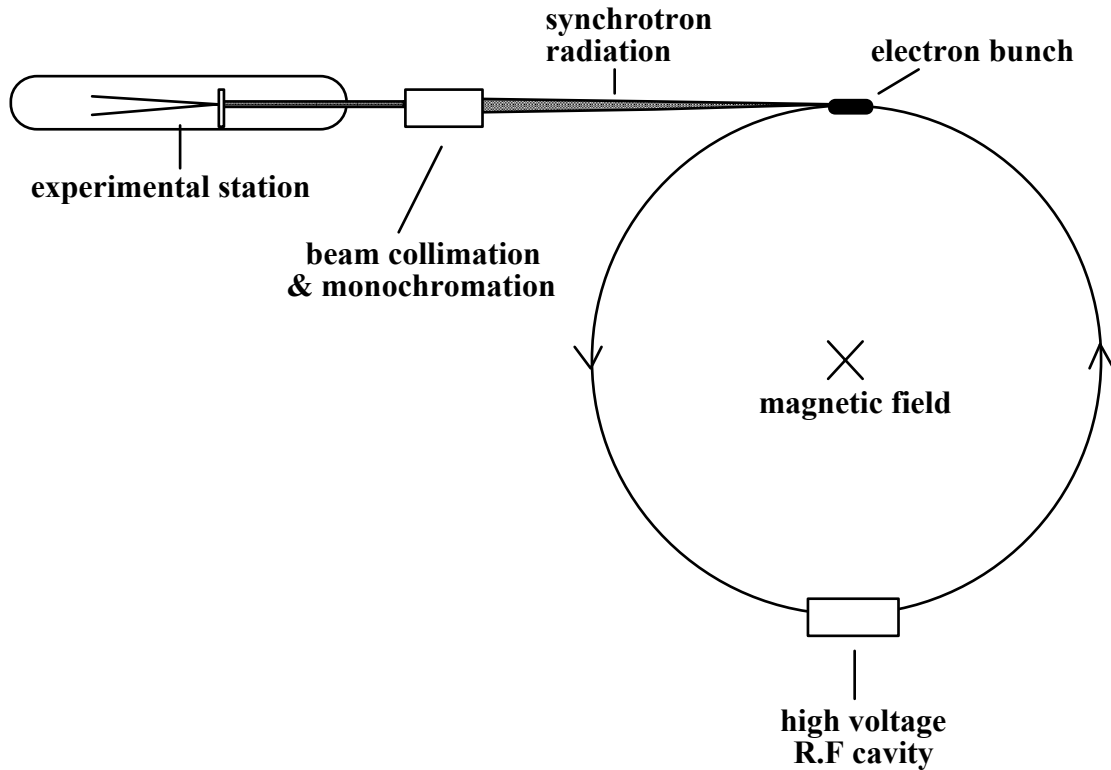

Figure 41: Schematic diagram of a synchrotron radiation storage ring.

A linear particle accelerator injects high-energy electrons (or positrons) into a booster ring, which increases the velocity of the particle before it enters the storage ring. In the storage ring the electron velocity increases to a relativistic level and stabilises. The electrons travel in a circular orbit due to the action of magnetic fields and the centripetal force ensures that they are continuously accelerated. A high voltage R.F source at one point in the orbit replenishes energy lost through radiation and packs electrons into bunches. Steering magnets reduce the cross-sectional beam area and guide the beam. The beam lifetime is limited to ~20 hours by atomic collisions, despite the high vacuum inside the storage ring. Storage rings, such as the one at Daresbury Laboratory (Warrington, U.K.) are usually operated in multi-bunch mode, with up to 160 electron bunches. This increases the current in the ring and subsequent radiation intensity. Single-bunch mode can be used when it is necessary to synchronise an experiment with the bunch "flypast" time i.e. an experiment on the timescale of the bunch rotation period (~nanoseconds).

The electron beam sweeps a "torchlight" of radiation ahead of it as it circles. The radiation is broadband, extending from the infra-red to hard x-ray region. The high frequency limit is reciprocally related to the local orbit radius, among other things. This radius can be reduced by inserting a compound arrangement of magnets, known as a wiggler, into the ring. Radiation is "extracted" from the electron beam along tangential "beamlines". The radiation is then split and diverted to different users working in experimental stations around the beamline. Experimental stations are each dedicated to a particular radiation requirement. The reader is referred elsewhere [76] for further information on the production of synchrotron radiation.

The work presented in this thesis was performed at Daresbury experimental station 2.1. Station 2.1 is dedicated to small angle time-resolved x-ray diffraction; the beam has the following properties [77]:

i)   Wavelength: 1.54Å. ($\Delta \lambda/\lambda \leq 0.03$).

ii)   Photon flux: 5 x 10^{11} photons/s (for storage ring operating at 2 GeV, 100mA).

iii)   Spot size at sample: nominally 1mm vertical by 5mm horizontal (can be reduced by further collimation, at expense of flux).

iv)   Divergence: depends on collimation and focusing (typically 1mrad horizontally and 0.2mrad vertically).

v)   Polarisation: virtually 100% plane-polarised in the plane of the electron bunch orbit.

The important parameter, as far as time-resolved experiments are concerned, is the photon flux, which is considerably higher than that obtainable from a conventional tube source (approximately 6 orders of magnitude higher).

Chapter 4

SMECTIC-A EXPERIMENTS

4.1 Introduction

The objective of the smectic-A experiments was a qualitative analysis of the switching process from a planar to homeotropic structure using electric fields. The study consisted of x-ray rocking experiments and complementary electro-optic experiments.

Before electric fields were applied to the sample the prevailing structure was examined; the sample was shown to have a chevron structure, which is unusual in the smectic-A phase. A preliminary x-ray experiment showed that the chevron structure emerged when cooling from the nematic phase, due to the decrease in layer spacing.

The "dynamic" x-ray rocking experiment was then carried out. This consisted of sitting the sample at a specific angle and applying an electric field while recording the x-ray diffraction as a function of time. The angle was then changed and the procedure repeated. It was thus possible to observe the layer orientation during switching, as a function of time. This was the first time ever that such experiments have been performed. The results show that the layering persists for a while after field application, even during molecular rotation.

Electro-optic switching experiments were then conducted. These consisted of microscopic observations, photographs, and an experiment to monitor the director behaviour during switching.

Finally, the electro-optic and dynamic x-ray results were compared, in order to formulate a model for the switching process.

4.2 Liquid Crystal Material

The main requirement of the liquid crystal material was the presence of positive dielectric anisotropy in a low molar mass system. S3 was chosen as it was specifically designed for use in smectic-A displays i.e. it is smectic at room temperature, and has a nematic phase to help alignment. S3 is the commercial name for a material obtained from Merck-BDH Ltd [78]. The company is unwilling to release details of the full chemical composition. S3 possesses the following phase sequence:

$$S_A \xrightarrow{\ 54.5^o C\ } N \xrightarrow{\ 59^o C\ } I$$
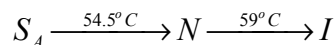
4.3 Cell Design

Sample cells were designed for use in both the x-ray experiments and the electro-optic experiments. The design criteria were as follows:

i)   A way of inducing uni-directional planar alignment in the liquid crystal

ii)   A way of applying electric fields to switch the liquid crystal

iii)   A thick section of liquid crystal, to give greater diffraction of x-rays

iv)   Maximum transmission of x-rays through cell substrates

v)   Thick cell substrates to prevent bending and to give the cell rigidity

vi)   Transparent cell substrates to facilitate electro-optic experiments

vii)   Parallel cell substrates to ensure a constant liquid crystal thickness across the cell,

The chosen cell design is shown in Figure 42.

100µm glass with transparent ITO coating

12µm Mylar polymer spacers

electrode wire

conductive coat

liquid crystal (capillary fills from one end)

wire soldered to conductive coat

PVA alignment agent applied on top of conductive coating and rubbed parallel to cell sides
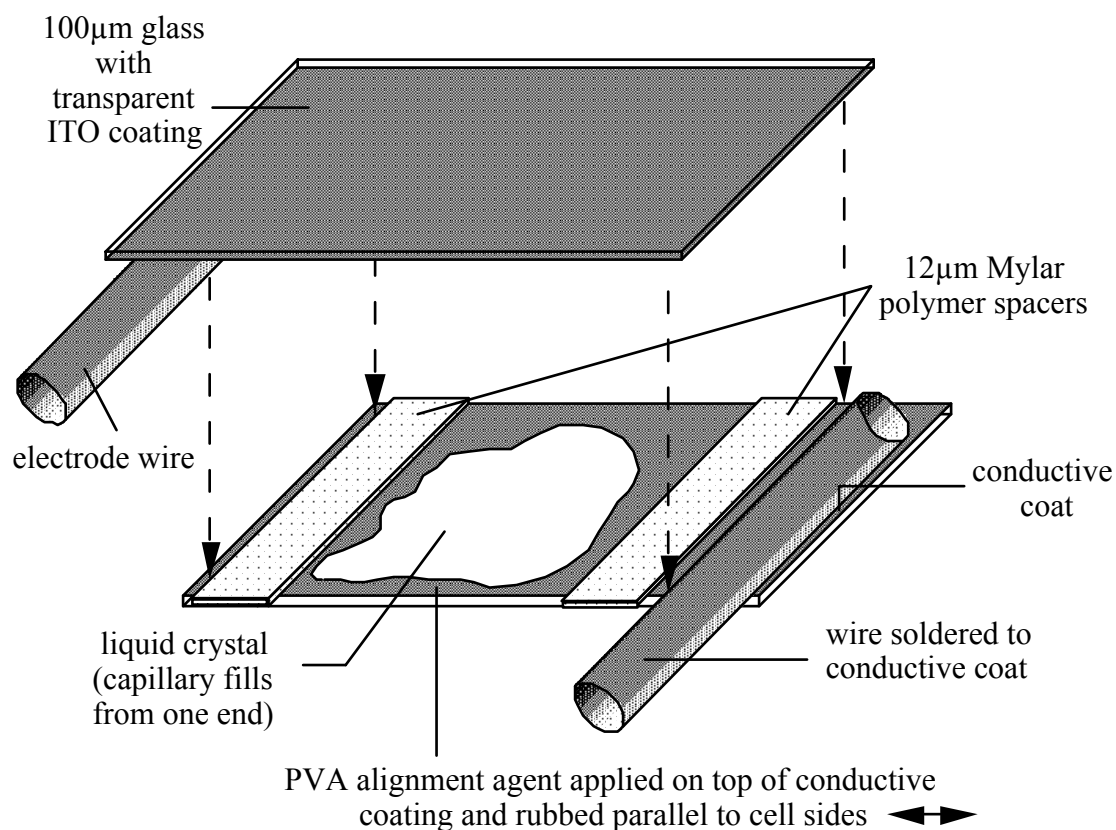
Figure 42: The final cell design.

Alignment

Planar alignment was achieved by applying a chemical agent to the substrates. The agent consisted of a 1% (by weight) solution of polyvinylalcohol (PVA) in distilled water. Uni-directional planar director alignment was achieved by rubbing the deposited PVA in a unique direction with a fine brush [79]. The preferred molecular orientation at the surfaces causes elastic forces to propagate into the liquid crystal, thereby causing the inner molecules to rotate. Alignment forces propagate better through nematic rather than smectic liquid crystals. For this reason the liquid crystal is introduced between the substrates in the nematic phase and cooled

slowly (approx. 1°C/min) into the smectic-A phase.

Liquid crystal thickness

The maximum thickness of liquid crystal that can be aligned by surface forces is typically 50–100μm in the nematic phase and 20–40μm in the smectic phase. Typical electric field strengths for smectic-A switching are 1-2 V/μm [80]. The voltage generator available for the experiments had a maximum output of 120V r.m.s. This imposed an upper limit of 60μm on the cell thickness. Thus the maximum liquid crystal thickness was governed by the alignment requirement of ~20μm. The requirement for maximum diffraction of x-rays dictated that the cell thickness be as near this upper limit as possible.

Cell substrates

The cell substrate materials considered were mica and glass. Mica was eventually rejected because of its birefringence, the poor adherence of conductive coatings and its tendency to break when the PVA was applied. Glass was thus chosen in preference.

It was necessary to obtain glass as thin as possible for lower x-ray attenuation. 100μm-thick glass [81] was obtained in sheets of ~10cm x 10cm. The glass was sufficiently flat for fabrication of the cells (<0.5μm thickness variation). The sheets were sent to GEC Hirst Research Centre [82] where they were coated with a conductive indium-tin-oxide (ITO) surface. Preliminary trials showed that the conductive coating did not contribute appreciably to x-ray attenuation. The coated sheets were cut to the required size (~1cm x 1cm) using a diamond-tipped cutting knife.

Applying electric fields

Electrode wires were attached to the conductive coating on the inner surfaces using indium solder. Indium solder has a lower melting point than conventional solder, and adheres much better to ITO-coated surfaces. The cell was sealed with glue before soldering, to avoid the liquid crystal flowing out towards the heat. Measures were also taken to reduce the local heat load on the cell so that the alignment was not destroyed.

Spacers

12μm Mylar polymer spacers were used between the substrates to maintain a constant thickness of liquid crystal and prevent a short-circuit [83]. They were fixed using a minute amount of epoxy [84].

Cell thickness measurements

The final thickness of liquid crystal equals the spacer thickness plus the glue thickness. Conventionally, liquid crystal cell thickness is measured using such techniques as the measurement of interference fringes with a spectrophotometer [85] or the measurement of empty cell capacitance with a capacitance bridge [86]. Neither of these techniques were used as a simple micrometer was sufficient. A precision digital display micrometer was used, for which the error in reading was +/-0.5μm. The total glass thickness (nominally 100+100=200μm) was measured before the cell was fabricated. The thickness of the completed cell was then measured; the liquid crystal cell thickness being the difference between the two readings (with a reading error of +/-1μm). The main concern with this technique was that the cell might be compressed during measurement. This was investigated by comparing micrometer results with

spectrophotometer results for the same cell[3]. Cell compression was determined to be < 0.25μm). This makes the total error asymmetric i.e. +1μm / -1.25μm. This error was considered acceptable for a qualitative analysis of the switching process.

The final liquid crystal thickness for the cell used in the smectic-A experiments was measured to be 15μm (+1μm / -1.25μm). In other words the glue thickness is approximately 3μm.

4.4 Static Smectic-A Experiment: Determination of Initial Structure

4.4.1 Introduction

Before applying electric fields to the cell the initial layer structure was examined. Many methods used in this experiment were also used in the other x-ray experiments.

4.4.2 Apparatus
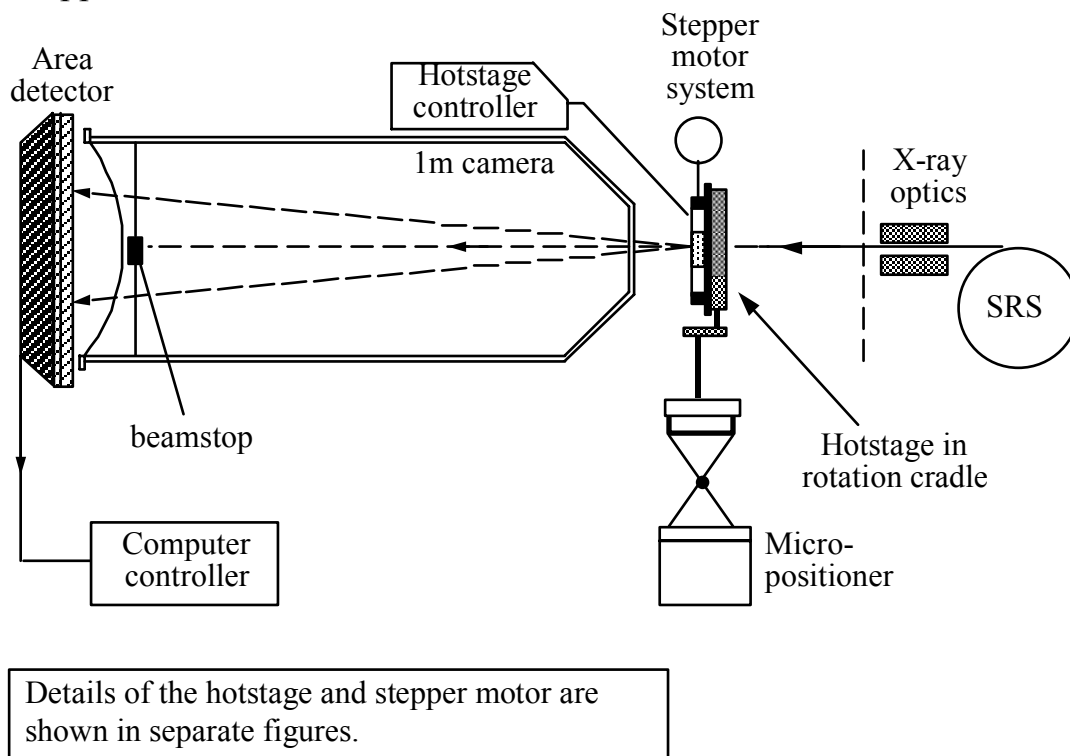
Figure 43: Apparatus for x-ray diffraction rocking experiment

The 1.54Å x-ray beam (full characteristics are given in section 3.3) enters the experimental hutch (station 2.1. at Daresbury) where it passes through an ion chamber (not shown in Figure 43 for clarity). The ion chamber measures the incident radiation intensity. The beam then passes through the hole in the back of the heating stage and onto the specimen where diffraction occurs.

---

[3]Private communication with P. Cox, Physics Dept;. Manchester University.

The diffracted beams (including the transmitted main beam) traverse a 1m evacuated camera, through a beryllium window. The main beam is blocked by a lead beamstop to protect the area detector. Diffracted beams pass through the thin Mylar membrane at the back of the camera and reach the area detector, which is kept close to the camera to minimise the air gap. The camera, detector and cell manoeuvring apparatus are on an optical bench. The area detector is a multi-wire proportional counter. The sensitive area of the detector is 200x200 mm^2, and consists of a grid of wires in a gaseous environment (Xe/Ar/CO$_2$ mixture). Radiation arrives at the detector and causes local ionisation; this results in a current pulse along the orthogonal wires that are nearest to the ionisation event. The pulse on each electrode travels towards both ends of the wire, where the signals are amplified. The relative signal arrival times are then compared in a time-to-amplitude converter (T.A.C), which determines the arrival point of the relevant x-ray photon. The quoted spatial resolution is ~0.5mm (wire spacing is 1mm) [77]. The event is registered in a memory crate, which converts and stores images as 4 byte numbers in a 512 x 512 array corresponding to the detector face. Additional events are added into the relevant element of the array; a larger number signifies higher x-ray intensity at that point. The total collection time is programmable from 10µs to several hours. For time-resolved experiments the user can specify up to 120 timeframes. The number is limited by the memory capability (each frame needs 512 x 512 x 4$\cong$1Mbyte.) Data is automatically transferred to the local computer (LS11/23), which is located in the experiment control room, outside the radiation hutch. The local computer is also used for data acquisition control. This includes programming the time frame generator (T.F.G), setting the graphics monitor, and sending synchronised T.T.L pulses for triggering (section 5.5.2). Data can be seen in real time on a graphics monitor with 256 colour levels. Up to four timeframes may be viewed simultaneously. Collected data is transferred to a local SUN workstation via an Ethernet link, and saved.

The liquid crystal cell is heated by mounting it on a commercially available heating stage (Linkam THMS 600 - "hotstage" [87]). Details of the heating stage are shown in Figure 44. A clip allows any part of the cell to be positioned over the hole in the heating block. An internal heating element can heat the sample up to 600°C. Temperature is measured by a platinum resistance thermometer close to the surface of the heating block. The temperature of the specimen is regulated using the Linkam TMS91 control unit, which attaches to the heating stage via a flexible cable that allows the stage to rotate freely. The control unit can adjust the temperature of the heating stage to a relative accuracy of 0.1°C. Linkam does not quote the accuracy of the absolute temperature. However it was sufficient to measure the reduced temperature relative to the smectic-nematic transition temperature. Because of thermal lag the temperature of the liquid crystal in the centre of the hole was lower than that of the heating block. The difference was calculated by measuring the phase transition temperatures of S3 on another (unmodified) heating stage, with the liquid crystal resting on a piece of 100µm glass. The temperature difference, which increases with temperature, was 0.5°C at the smectic-nematic transition. The temperature difference was then calculated for each temperature used in the experiment, presuming there to be a linear variation from 0°C difference at room temperature to 0.5°C difference at the smectic-nematic transition temperature. All experimental temperatures mentioned in this thesis have already been adjusted accordingly.
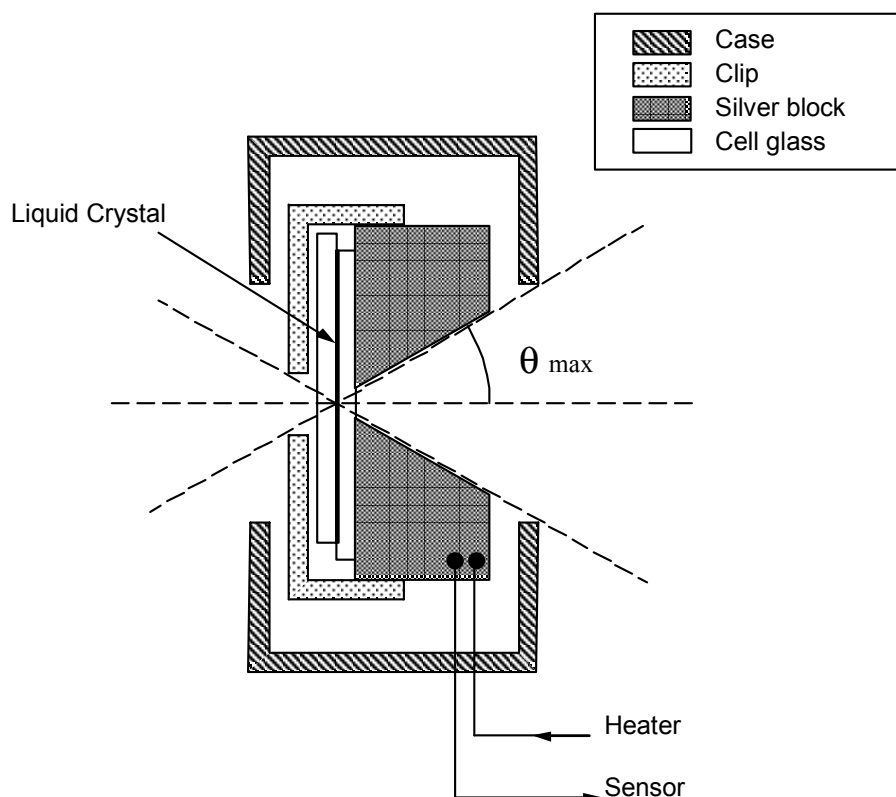
Figure 44: The heating stage and sample holder. θ_{max} is the maximum angle through which the sample may be rotated without blocking the incident and Bragg-diffracted x-ray beams (for small angle diffraction only).

The heating stage is held in a cradle, which allows it to be manual rotated about the beam axis (Figure 45). The cradle is attached to a 25:1 gearbox that couples with a stepper motor (RS 440/442). The orientation of the stepper motor system is such that the cell can be rotated about a vertical axis. The stepper motor is run from a PC via a control crate, which provides the driving voltages. The software–which enables one to move the cell to a specified angle–was developed in the physics department in conjunction with Nick Bowring. The step size is 1.8°, which means that the overall resolution in rocking angle is $1.8 \div 25 = 0.072°$.

Beamline shutters can be opened and closed (effectively turning on and off the incident x-ray beam) from the control room.
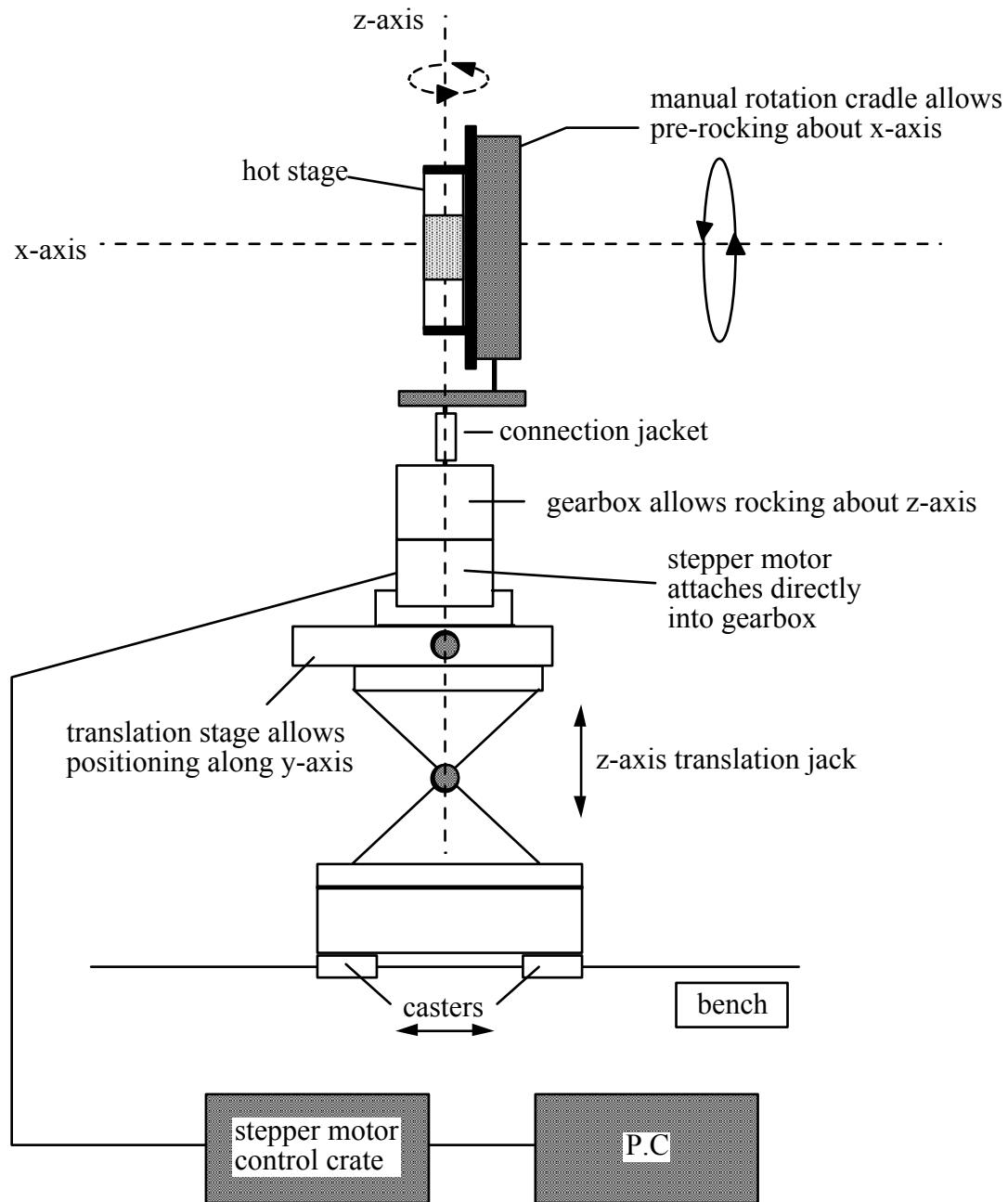
Figure 45: X-ray positioning apparatus. The y-axis comes out of the plane of the paper.

4.4.3 Alignment of the apparatus

The size of the beam spot at the sample can be controlled by adjusting the collimating slits. The size is measured using photosensitive "green paper". X-rays cause the paper to turn red at the point of impact. The chosen beam spot size was ~1mm x ~1mm. This enabled the beam to pass through the hole in the centre of the heating stage at all rocking angles. A 1m camera was assembled and a lead beamstop was installed at the back of the camera. The x-ray camera was

then evacuated. The area detector was placed immediately behind the camera. The heating stage was placed in the rotation cradle. The micro-positioning equipment (a translation stage and a jack) was adjusted so that the central hole in the heating block was concentric with the x-ray beam path (using "green paper"). The heating stage was moved as close as possible to the front of the camera to minimise the air gap for diffracted beams. After all adjustments had been made it was possible to remove and replace the heating stage in the rotation cradle without disturbing its position.

4.4.4 The experiment

The temperature chosen for the later dynamic experiment was 51.5°C (the reasons for which will be discussed later). Because an initial check showed chevrons at this temperature X-ray rocking experiments were carried out at various temperatures from the nematic phase downwards to investigate.

The sample cell was checked (using a polarised microscope) to find a region of good alignment to be used for all the experiments. The cell was then adjusted so that this region lay over the heating stage hole, with the layer normal direction (k) approximately along the y-Figure 45). The 0° rocking angle position was defined as that in which the cell face was perpendicular to the x-ray beam. The apparatus was rotated to this position (0°). This procedure was only undertaken once, so the error involved is a systematic error. The accuracy in aligning the heating stage was estimated to be +/-1°, and +/-2° in the angle of the cell face relative to the heating block (due to the cell glue). This gives a total systematic error in rocking angle of +/-3°.

Fine adjustments were carried out to make the layer normal direction coincide with the horizontal detector axis (see section 3.2 and appendix B). With the sample at room temperature and 0° rocking angle, an unrecorded diffraction pattern was taken (~10s). The pattern showed two spots, indicating a smectic-A structure. The rotation cradle was manually rotated until the spots lay on the equator.

The sample was then heated into its nematic phase and cooled at 1°C/min. until it reached 54.5°C, just within the smectic phase. The cell was held at this temperature. The sample was rotated to -11° and a 30-second x-ray exposure recorded. The cell was then rotated, in 1° steps, to +12°; a 30-second exposure was taken at each step. Rotation was always performed clockwise to avoid gearbox backlash. The process was repeated at various temperatures down to 30.5°C (54.5°C - 50.5°C in 1°C intervals, then 50.5°C - 30.5°C in 5°C intervals). Large angle steps were used to complete the experiments in our allocated "beam time". The practical resolution in rocking angle was thus 0.5°, compared to a possible resolution of 0.072°. The 0.5° resolution was sufficient for a qualitative analysis.

A standard collagen calibration sample was used to calibrate positions on the detector in terms of the related structural spacing. Collagen has a lamellar structure along the strand, with a room temperature lamellar spacing of 670Å [88], and produces a sharp diffraction pattern with clearly identifiable low angle spots. The liquid crystal cell was removed and the collagen sample placed in exactly the same position, oriented such that the diffraction spots were horizontal. A 10 minute x-ray exposure was taken. The diffraction pattern was recorded and used to calibrate

the detector (see section 4.4.5).

Because different wires on the detector are more sensitive than others a "detector response" calibration was performed. A small radioactive source was placed in a frame at about 50cm away from the face of the detector. The radiation pattern was then recorded for two hours and used to calibrate the detector (see section 4.4.5).

4.4.5 Treatment of data

4.4.5.1   *Computational process*

The data was transferred from the local computer to a high performance PC. The PC has a Pentium processor, a 2Gb hard disk, and a 17inch S.V.G.A monitor. Data processing consisted of analysing the two-dimensional files and any subsequent one-dimensional files (line integrations etc.). The 2D analysis was performed using software developed in the physics department by N. Bowring. 1D analysis was performed using the Origin graphics program from MicroCal Software Inc [89]. Typical raw data is shown in Figure 46.
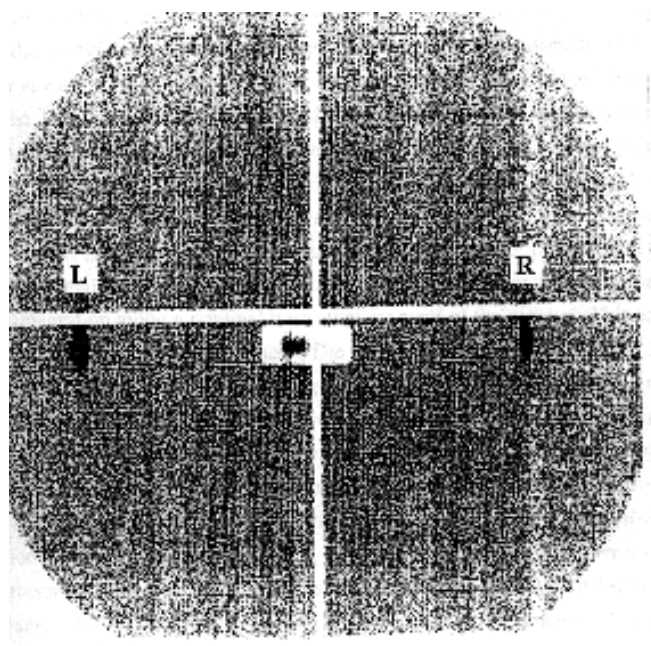
Figure 46: A typical raw data printout.

The central rectangle is the outline of the beamstop. (The beamstop does not necessarily correspond with the exact centre of the detector.) The strips passing through the centre of the detector are facets of the T.A.C system (section 4.4.2.) They displace the diffraction picture rather than obscure it, and are removed computationally during data manipulation.

The printout shows two diffraction spots, L and R, on the equator. The spots correspond to diffraction from both sides of different layers, and can be seen simultaneously because the sample mosaicity was greater than twice the Bragg angle. In other words the reciprocal space lattice points are smeared so much that the n=1 and n=-1 spots both touch the Ewald sphere

simultaneously. As the sample is rotated, the diffracting planes will gradually swap over so that the rocking curves are the same for both spots, but displaced by 2θ. Thus it was only necessary to monitor one of the spots (L or R) to form a complete rocking curve.

The raw data files were normalised by dividing them by the detector response calibration file. The T.A.C strips were then removed by shifting horizontal and vertical raster lines accordingly. To find the width to shift by, a vertical integration was taken along a nominal horizontal segment of the picture and a horizontal integration was taken along a nominal vertical segment. A typical 1D vertical integration is shown in Figure 47.
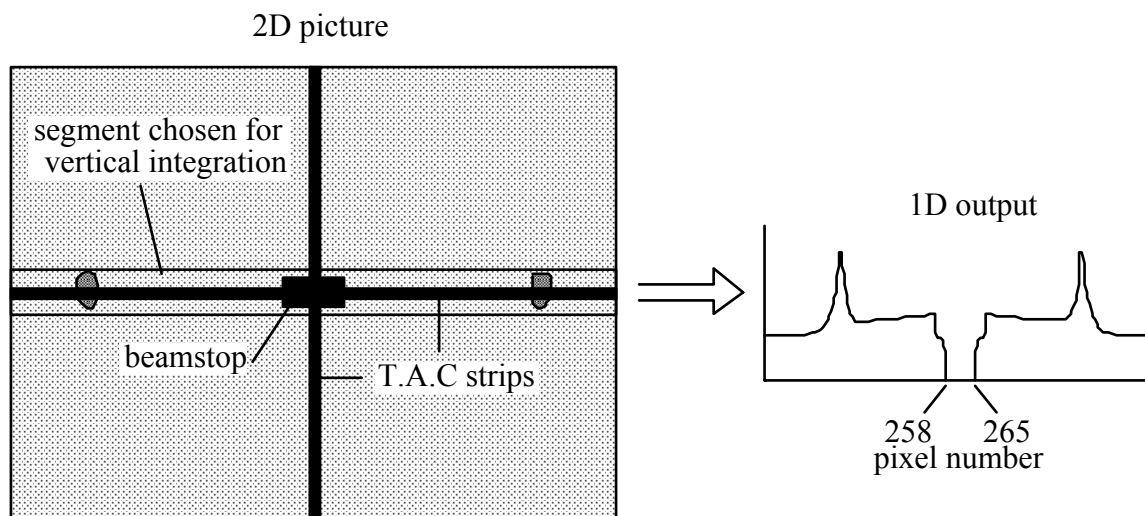
Figure 47: Obtaining a typical 1D vertical integration plot.

4.4.5.2   Obtaining rocking curves

A rocking curve indicates the number of layers contributing to a Bragg peak, at any particular cell angle. As the *maximum* Bragg peak intensity is sensitive to experimental conditions it is usual to determine the *integrated* peak intensity [90]. Diffraction spot A was chosen. The total diffracted intensity of the spot was obtained by performing a box integration. A box integration adds the intensities of every pixel within a tight box around the spot. At each temperature all rocking angle files were first previewed to determine a good box size/position. The spot position was expected to change slightly with temperature. The process was thus repeated for each temperature and a "global" box size/position was determined accordingly.

The rocking curve at each temperature was obtained by plotting the integrated diffraction intensity against the cell angle. The final curve was normalised to account for the various contributions discussed later in this section.

4.4.5.3   Obtaining layer spacing

Obtaining the layer spacing involved three steps: Firstly a 1D diffraction profile was taken by performing a vertical integration over a narrow horizontal segment passing through the diffraction spot. Secondly, the centre of the resulting peak was determined in terms of pixel

position, and thirdly the collagen calibration file was used to convert this position into layer spacing.

There are different methods for defining the peak centre [91]. The chosen method was based on determination of the centre-of-area of the peak. Unlike the other methods this one can be applied equally well to a "messy", indistinct peak such as the low intensity peaks obtained in the time-resolved experiments. Consider the peak below.
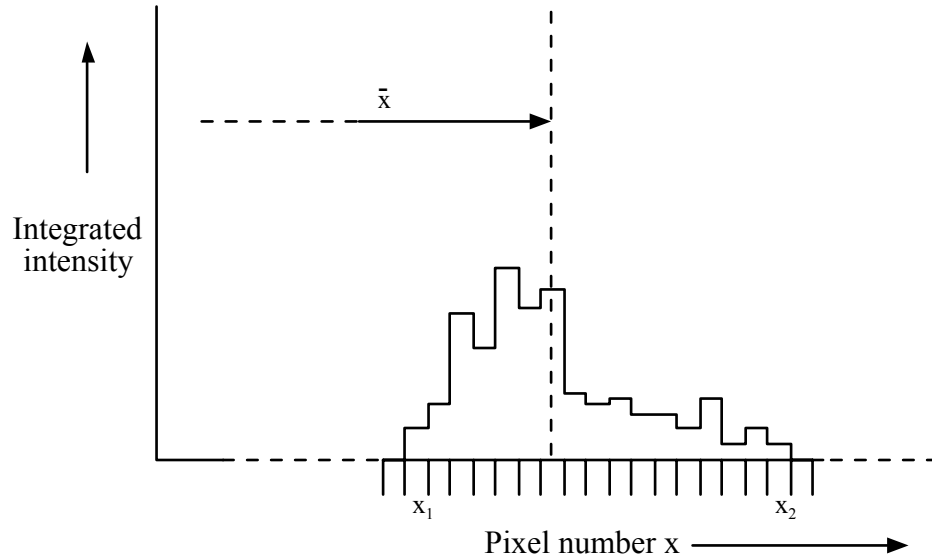

Figure 48: Determination of peak centre using the centre-of-area technique.

The peak position is defined to be that of the vertical axis through the centre-of-area. This position is determined relative to an arbitrary zero (the first pixel). The procedure is as follows:

Let $X+1$ be the peak centre in terms of pixel position. Let the integrated x-ray intensity at a single pixel position be dI. Let the total integrated intensity under the peak (the total area) be I The peak centre is then given by the standard centre-of-area formula:

$$X = \frac{\sum x.dI}{I} \equiv \frac{\sum x.dI}{\sum dI}$$

Equation 13

The calculation is performed using values of x from $x=x_1$ to $x=x_2$.

The collagen calibration can then applied. Figure 49 shows the vertical integration plot obtained from the collagen diffraction pattern (raw data). The first few diffracted orders are obscured by the beamstop. The other orders can still be identified because the relative intensities are well-documented [88]. For wet collagen the most intense peaks occur for orders 1, 3, 5, 9, 12... These are indicated in Figure 49.

47
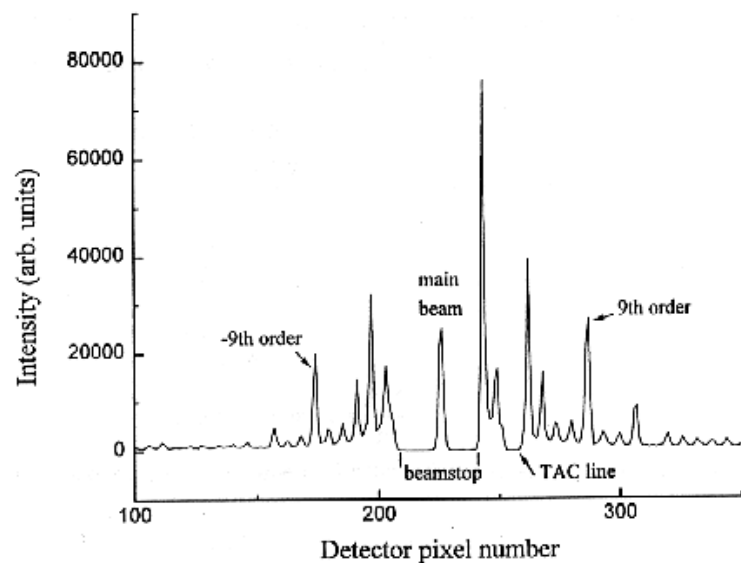
Figure 49: The vertical integration plot obtained from collagen.

Consider a small angle n^{th} order diffraction and the corresponding $-n^{th}$ order diffraction, for collagen, as shown in Figure 50 (T.A.C lines removed).
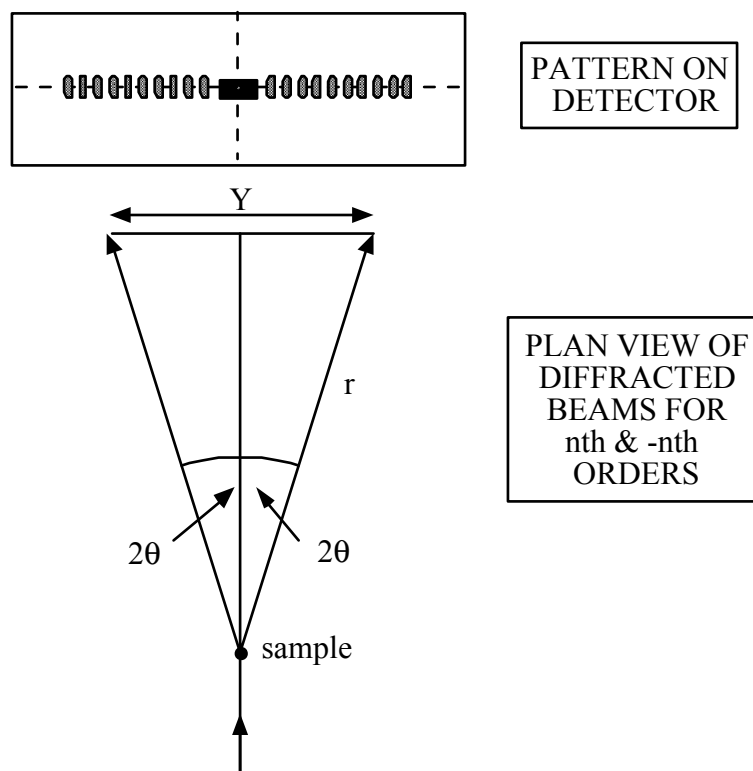
Figure 50: Calibrating for layer spacing using the collagen diffraction pattern.

θ is the Bragg angle. Y is the distance on the detector between the diffraction spots, measured in

pixels. Now, from Equation 11,

$$n\lambda = 2.d.\sin\theta$$

$$= 2.d.\frac{\sin 2\theta}{2} \quad \textit{(for small angles)} \qquad \textit{Equation 14}$$

$$= \frac{d.Y}{2.r}$$

Therefore $\quad r = \frac{d.Y}{n} \Big/ 2\lambda$

$\textit{Equation 15}$

$= a/2\lambda, \textit{ where } a \equiv \frac{d.Y}{n}$

Now consider the same geometry for the diffracted beams from the liquid crystal:

$$n''\lambda = \frac{d'Y'}{2r'} \qquad \textit{Equation 16}$$

For small angles $r \approx r'$ so:

$$n''\lambda = \frac{d'.Y'}{2r'}$$

$$= \frac{d'.Y'.2\lambda}{2a} \qquad \textit{Equation 17}$$

Therefore $\quad \dfrac{n'}{d'} = \dfrac{Y'}{a}$ $\qquad \textit{Equation 18}$

$d' = \dfrac{n'.a}{Y'}$ $\qquad \textit{Equation 19}$

Now, the 9th order peaks for collagen were nominally chosen, for which the difference in pixels, Y, was 113 pixels. The d-spacing for collagen is 670 .

Therefore $\quad a = \dfrac{670 \times 10^{-10}}{9} \times 113 = 8412 \times 10^{-10} \, (m.pixels)$

And the liquid crystal diffraction is first order so:

$d' = \dfrac{8412}{Y'} \; \mathring{A}$ $\qquad \textit{Equation 20}$

4.4.5.4   Error and resolution in layer spacing

The experimentally observed layer spacing resolution (full width at half maximum, "fwhm") is not necessarily the same as the error in the calculated layer spacing, as the latter also depends on computational procedures. The spread in diffraction spot size, for example, might be five pixels,

whereas the peak position might have an error of two pixels for the same spot. The resolution nevertheless gives an idea of the instrumental and sample contributions to the diffraction spot size and is thus treated below, in addition to the error calculations.

4.4.5.4.1 *Error in layer spacing*

The error in layer spacing is calculated from Equation 20. The absolute error is determined from the errors in a and Y'. The relative error is determined only by the error in Y' (used for layer space comparisons in the smectic-A experiments).

Relative error:

Estimated error in peak centre identification = +/-0.25 pixels. Since Y' involves finding the centres of two peaks, the error in Y' is +/-0.5 pixels. For ~35Å this equates to +/-~0.2% = +/-0.07 Å.

Absolute error:

a) Error in *a*.

The small angle assumptions introduce negligible error. The error in *a* therefore equals the error in Y (for collagen) = +/- 0.5/113 = +/- 0.45%.

b) Error in Y' = +/-0.2% as shown above.

The absolute error is then approximately 0.5%. For ~35Å this equates to +/- 0.0175Å.

4.4.5.4.2 *Resolution in layer spacing (spot size)*

Contributions are first calculated in terms of pixel resolution and then converted to layer spacing resolution. (For a 1m camera a 1° diffraction angle is approximately equivalent to 0.017m on the detector $\cong$ (17mm/200mm) x 512 = 44 pixels). The overall experimental resolution (fwhm) is obtained by comparing the overall diffracted beam resolution with the detector resolution. The ultimate obtainable experimental resolution will be the larger of the two. The contributing factors are considered below:

Diffracted beam resolution

a) Sample broadening factors

- Out-of-plane mosaicity: This is considered later.

- Darwin width [90]: A 15μm thick sample has a Darwin width broadening of 9 x10^{-6} radians = 5 x10^{-4} °= 0.02 pixels fwhm.

b) Instrumental broadening factors:

- Wavelength spread: $\Delta\lambda/\lambda$ = 0.03. The layer spacing for S3 turns out to be ~35Å, corresponding to a Bragg angle of 1.26°. The wavelength spread gives a corresponding spread in Bragg angle of 0.08° fwhm.

- Divergence: typically 1mrad horizontally = 0.06° approx. (incident beam).

- Incident beamspot size diameter: = 1mm = (1mm/200mm) x 512 = 2.6 pixels.

Detector resolution

- (0.5mm/200mm) x 512 = 1 pixel approx.

The Darwin width is evidently negligible. The other factors contribute as follows. First consider the hypothetical case of zero mosaicity. The divergence alone allows the Bragg rocking condition to be satisfied for a wavelength spread (Bragg angle spread) of 0.06°. The spread in 2θ at the detector is then = 0.12° = 5.3 pixels. The incident spot size adds an extra 2.6 pixels. So the final (convoluted) contribution to diffracted beam resolution = 7.9 pixels. Now consider the contribution from the out-of-plane mosaicity, which is gauged by looking at the diffraction plots. The fact that two spots can be seen simultaneously, means that the out-of-plane mosaicity must at least equal 2θ$_B$ (~3°). This means that there will always be suitably oriented layers to correspond with the 0.08° spread of Bragg angles (the effect of the wavelength spread). The resultant spread in 2θ, at the detector is 0.16° = 7 pixels. Adding the spot size contribution gives 9.6 pixels.

The overall resolution is thus given by the convoluted diffracted beam resolution = 9.6 pixels (rather than the detector resolution, which is only 1 pixel). This corresponds to an angular resolution (spot size) of 0.22° (equivalent to a resolution in layer spacing of 2.89Å (fwhm), at ~35Å).

4.4.5.5 Normalisation of rocking curve intensity

The simple, qualitative nature of the x-ray experiments meant that many of the usual x-ray correction factors did not need to be applied [90].

The effect of the change in rocking angle (+/-30°) *was* significant however, and the appropriate correction factors were thus applied. Background count reductions were also applied. As far as qualitative information is concerned the normalised data did not differ from the raw data. The normalisation procedures are discussed below:

4.4.5.5.1 Background reduction

Background radiation adds to the coherent Bragg scattering, as shown in Figure 51.
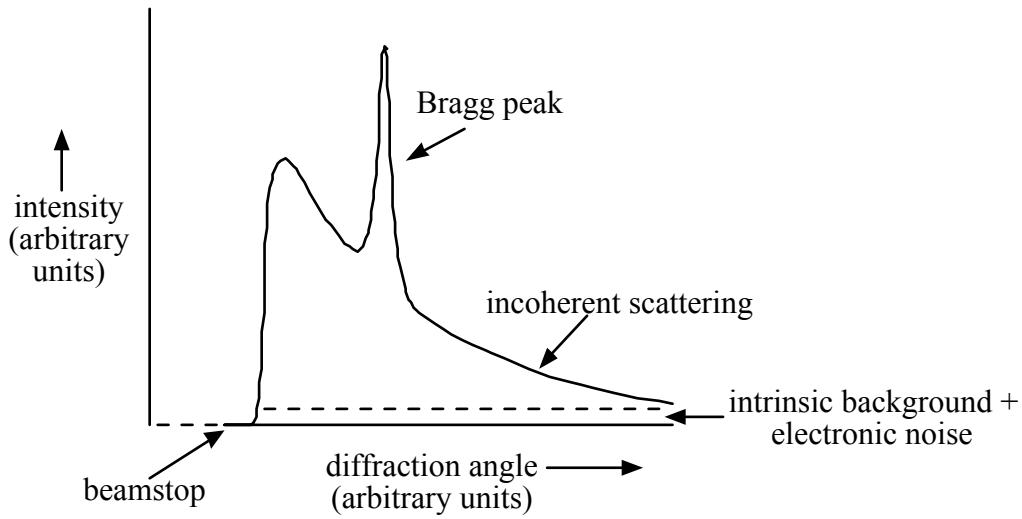
Figure 51: Schematic background scattering in a diffraction experiment.

In the reported experiments the Bragg peak typically occurred over ~15 detector channels. The highly noisy diffraction profiles and the qualitative nature of the experiments, made an elaborate background fit unsuitable. To a first approximation the background beneath the peak falls off linearly and was accordingly subtracted in the following way:

The mean count was calculated for the 10 (nominal) detector channels either side of the peak (Figure 52). The average of the two means was taken to as the average background below the peak. This value was multiplied by the total number of channels beneath the peak and the result was subtracted from the total integrated peak intensity.

These detector channels integrated
to get total peak intensity

Background
count

mean background
to left of peak

average of the means
approximates total
background below peak

mean background
to right of peak

10 channels   10 channels
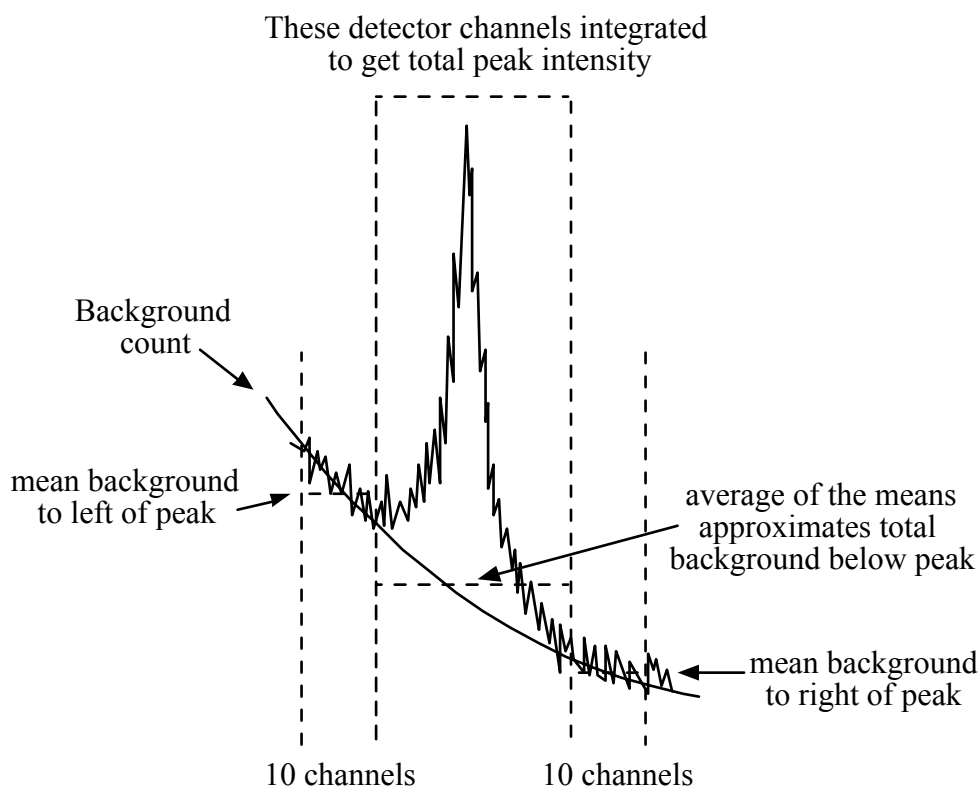
Figure 52: Removal of background radiation count.

4.4.5.5.2   *Incident beam intensity.*

Each rocking curve was normalised to account for changes in the incident beam intensity, by dividing the diffracted intensity by the corresponding ion chamber count.

4.4.5.5.3   *Changes in absorption with rocking angle.*

Incident radiation reaching the liquid crystal is attenuated by the first glass plate. Diffracted radiation is then attenuated by the second glass plate. The overall attenuation depends on the angle of the cell relative to the beam. At larger angles the incident beam travels through a thicker section of glass. The diffracted beam attenuation also depends on the diffraction angle and the sense (+ or −) with respect to the incident beam. Low angle scattering makes the situation simpler however: The scattering angle 2θ is less than $3°$; this is comparable to the error in locating the zero position (see section 4.4.3). For any cell angle the diffracted beam can thus be considered to travel through the same thickness of glass as the incident beam. The overall attenuation is that of the incident beam multiplied by that of the diffracted beam.

To calculate the beam attenuation, the linear absorption coefficient of the glass (μ) was measured as follows: The incident x-ray beam was attenuated to avoid damage to the detector in the absence of the beamstop. The integrated spot intensity (I_0) was recorded (over 10 seconds). A piece of the 100μm-thick glass was then placed in the beam path, with its face normal to the beam. The attenuated integrated spot intensity (**I**) was recorded over the same time. The linear

absorption coefficient is given by [90]:

$$\mu = \frac{-\ln(I/I_0)}{x}$$

Equation 21

The measured value was ~136 cm^{-1}. The path length of the incident beam in the front glass plate of the fabricated cell (r) is then given by Equation 22:

$$r = \frac{x}{\cos\delta}$$

Equation 22

where x is the glass thickness and is the rocking angle of the cell relative to the incident beam. The zero degree position is that where the beam strikes the cell face normally. The relative intensity of the beam (A) after traversing a distance r is given by Equation 23:

$$A = \exp(-\mu.r)$$

Equation 23

The final normalisation factor is then A^2. This value is calculated for each rocking angle and the diffracted intensity at each angle is divided by the normalisation factor.

4.4.5.5.4   Changes to liquid crystal active volume with rocking angle

As the cell is rotated to different angles the x-rays pass through different thicknesses of liquid crystal. An increase in active volume has two consequences:

a) The amount of material contributing to diffraction increases.

b) The absorption of x-rays by the liquid crystal increases.

The two effects lead to an optimum sample thickness, above which the diffracted intensity falls off. It can be shown [90] that this thickness is given by $1/\mu$. The linear absorption coefficient of the liquid crystal was calculated based on the liquid crystal chemical composition (obtained from the manufacturer in confidence). The reader is referred to reference [92] for details of such calculations. The linear absorption coefficient of the liquid crystal was calculated to be ~4.1 cm^{-1} and the optimum thickness is accordingly ~0.24cm, being much larger than the sample sizes used. a is therefore very much the dominant process in this case. An angular correction factor is routinely applied in transmission diffraction experiments from sheet samples. The factor R, given below, relates the diffracted intensity at a rocking angle δ to that at 0°. A full derivation of the factor is given in reference [90].

$$R = \frac{I_D(\delta = \delta)}{I_D(\delta = 0)} = \frac{\cos\theta.\left[e^{-\mu.t/\cos(\theta-\delta)} - e^{-\mu.t/\cos(\theta+\delta)}\right]}{\mu.t.e^{-\mu.t/\cos\theta}\left\{\left[\cos(\theta-\delta)/\cos(\theta+\delta)\right]-1\right\}}$$

Equation 24

where I_D is the diffracted intensity, θ is the Bragg angle and t is the liquid crystal thickness. R is then calculated for each rocking angle and the value of the measured intensity at that angle divided by it. (For $\theta = 1.5°$, $t = 15\mu m$ and $\delta = 30°...R = 1.14$).

The appropriate normalisation factors were applied to the raw data for the smectic-A experiment.

4.4.6 Results
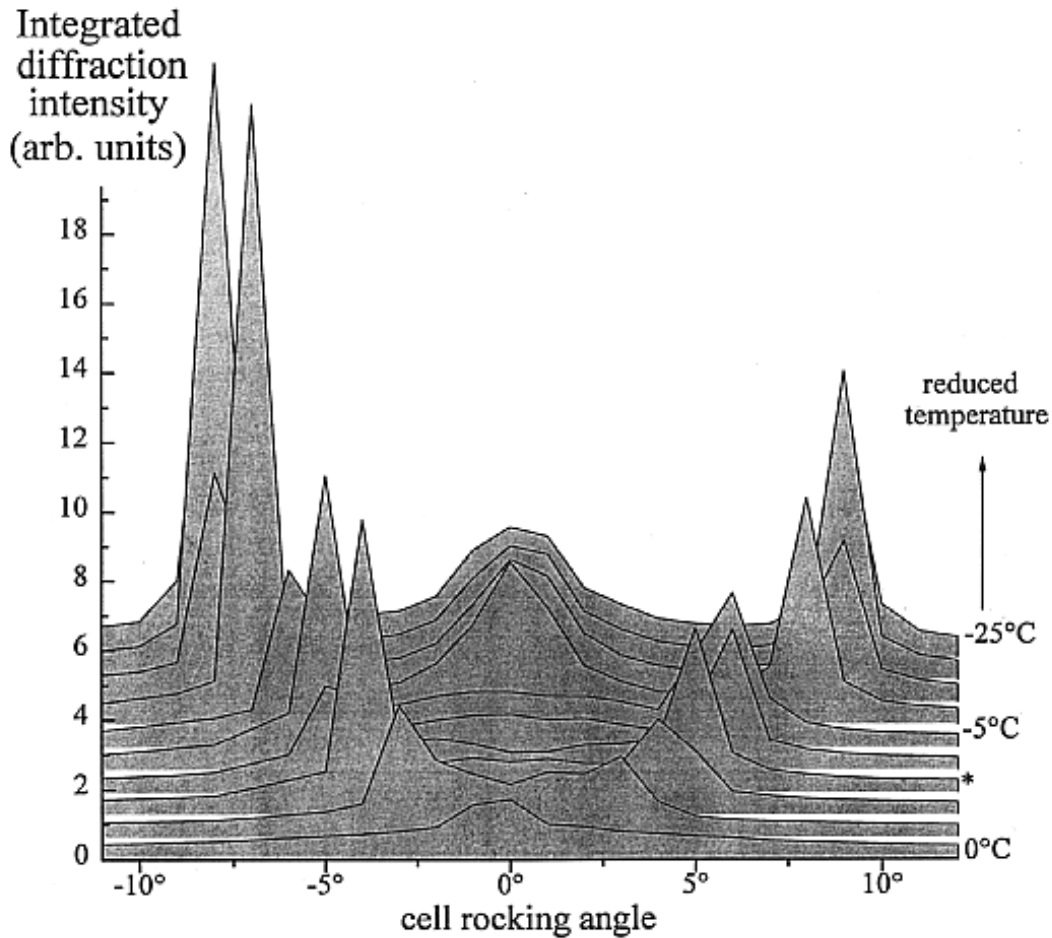
Figure 53: Normalised x-ray rocking curves as a function of temperature, for the smectic-A cell.

The bookshelf structure emerges at the transition from the nematic phase to the smectic-A phase. On cooling, the peak splits into two, indicating the formation of a chevron structure. The peaks move apart on further cooling, as the chevron angle increases. The initial layer structure in the cell before switching (dynamic experiment—section 4.5) is represented by the rocking curve for 51.5°C (reduced temperature =3°C). A central peak emerges between the reduced temperatures -5°C and -10°C. This central peak co-exists with the chevron peaks, indicating a chevron/bookshelf aggregate structure (see Appendix B). The aggregate structure forms when the chevron angle is between 6° and 7.5°. (It probably forms to overcome the strain caused by increased director splay at the chevron apex). As the sample is cooled between the reduced temperature -10°C and -15°C, the bookshelf section increases slightly and the chevron angle increases to ~8.5°. No structural changes were seen on further cooling i.e. the chevron angle remained constant at ~8.5°.

The chevron peak heights change markedly from one temperature to the next and from one arm of the chevron to the other. This is because the integrated diffraction spot intensity is very

sensitive to rocking angle and the (large) 1° rocking steps are insufficient to resolve the fine structure. It is not possible to infer from the rocking curves therefore, whether the chevron structure is symmetric or asymmetric. In the absence of an obvious mechanism for asymmetry it seems likely that the cell possesses a *symmetric* chevron state. The change in structure on cooling is shown schematically in Figure 54.
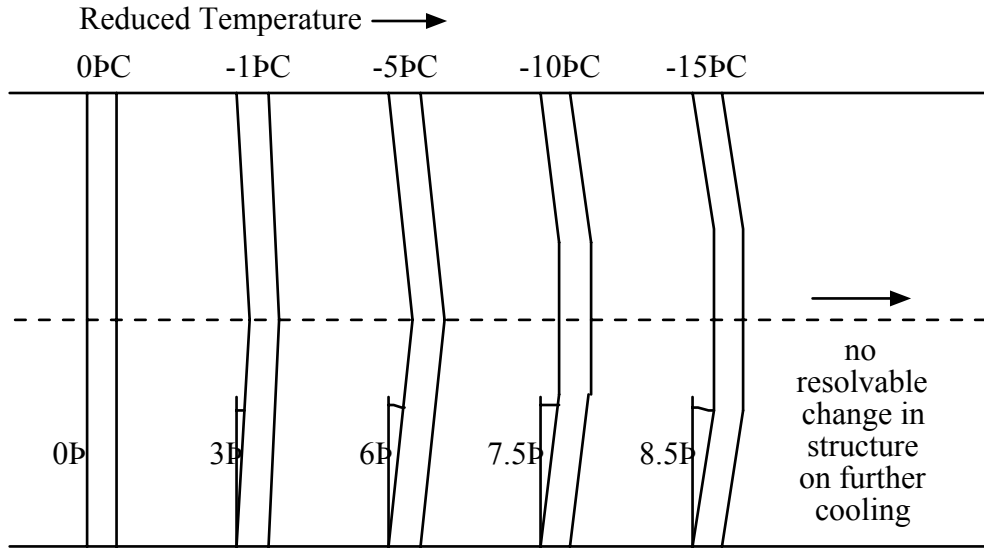
Figure 54: Scaled shematic illustration of cell structure changes with temperature.

The next step was to check that the chevron formation was due to a reduction in layer thickness. Although caused by changes in conformational length, as opposed to changes in the tilt angle, the chevrons are expected to form in the same way as they do in ferroelectric cells. This hypothesis was tested using Equation 9, redefined below.

$$d(T) = d(S\text{-}N).\cos(\delta(T))$$
<div align="right">*Equation 25*</div>

where $d(T)$ is the layer thickness below the S_A-N transition temperature, $d(S\text{-}N)$ is the layer thickness at the transition temperature, and $\delta(T)$ is the chevron angle.

The layer spacings were measured on the detector using the method described in section 4.4.5.3 (Bragg equation). The measurement at the S_A–N transition temperature was defined as $d(S$–$N)$ in Equation 25. The layer spacings were then calculated as a function of temperature $d(T)$ using, Equation 25, with the chevron angles $\delta(T)$ measured from Figure 53. Layer spacings calculated with the chevron equation are shown in Figure 55, alongside those based on the Bragg equation. The transition temperature spacings are the same by definition. The spacings at lower temperatures are self-consistent within experimental error, indicating that layer thinning is indeed the mechanism for chevron formation in the smectic-A phase. The relative error bars in the Bragg angle layer spacings in Figure 55 were determined in section 4.4.5.4. The relative error bars in the chevron angle layer spacings come from the propagated (+/- 0.5°) error in chevron angle determination.
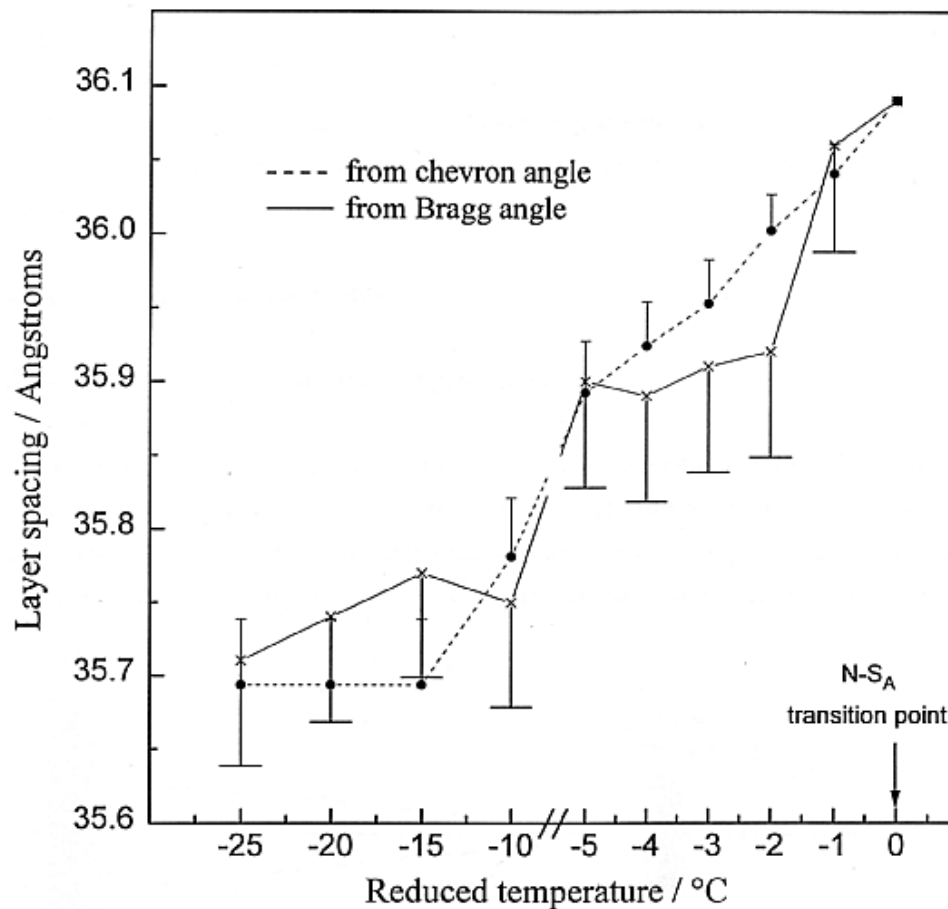
Figure 55: Comparison of layer spacings calculated using the chevron equation and the Bragg equation. The error bars are the relative errors. To make the graph more readable the negative error bar has been omitted from the "chevron angle" plot and the positive error bar has been omitted from the "Bragg angle" plot.

4.5 Dynamic Smectic-A Experiment: Layer Behaviour during Switching

4.5.1 Introduction

The dynamic experiment consisted of:

i)   An X-ray experiment to monitor layer behaviour during switching.

ii)   Photographs and electro-optic measurements to monitor optical characteristics during switching.

4.5.2 Apparatus

The apparatus is basically the same as that used to determine the initial layer structure (see Figure 43 and section 4.4.2). The only additions are the use of multiple detector time frames and equipment for generating electric fields (Figure 56).

57
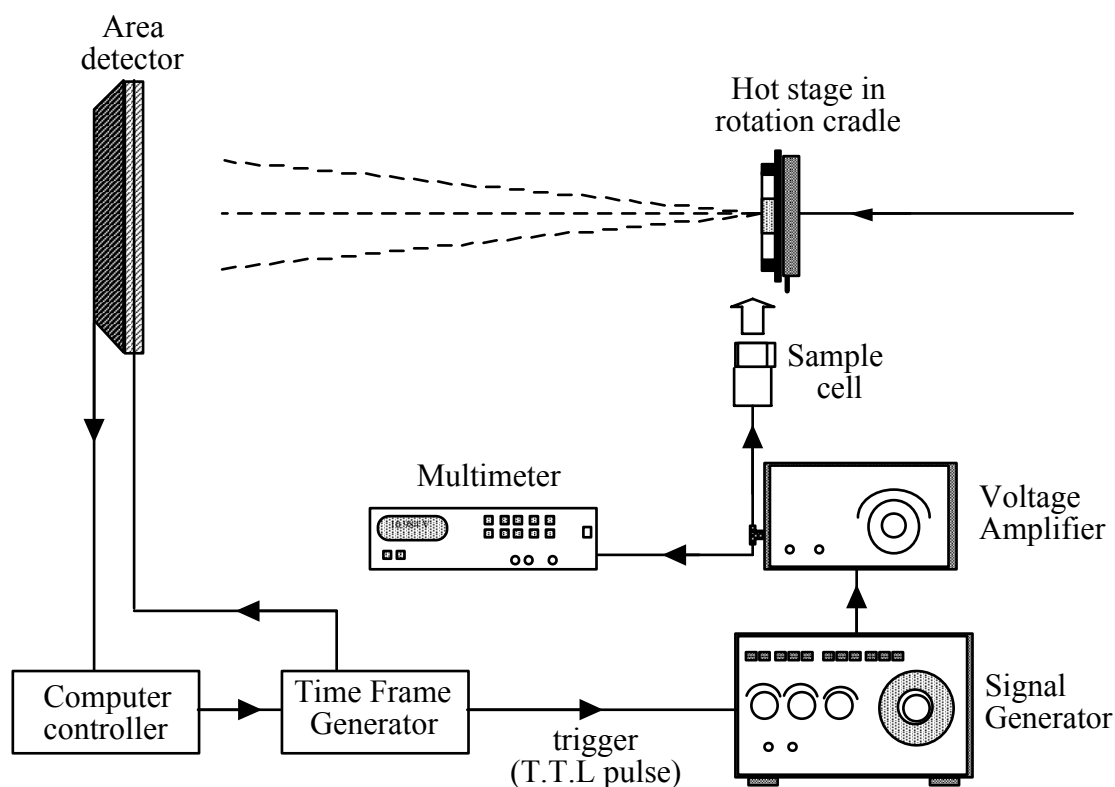
Figure 56: Additional apparatus used in the dynamic x-ray rocking experiment.

4.5.3 X-ray experiment

Diffraction patterns were recorded in successive time frames. Because the experiment was not reversible the minimum acceptable length of time frame was deemed to be that which was necessary to obtain a reasonable signal-to-noise ratio (coherent diffraction/background) at the Bragg condition. This ratio (judged by eye from the graphics monitor) was about 10:1. It took approximately 0.5 seconds to obtain such statistics. At the time of the experiment there were problems with the Daresbury computer that meant that the file size was limited to 20 time frames (out of a possible 120). The total data-capture time was thus 20 x 0.5 = 10 seconds.

The temperature and voltage of the sample were adjusted to give a switching time of ~5 seconds. The chosen temperature was 51.5°C, which was 3°C below the smectic-A/nematic transition temperature. The chosen applied waveform was a 30Vr.m.s, 1kHz sine wave. The waveform was obtained using a programmable signal generator and amplified to 30Vr.m.s using a wideband voltage amplifier. The applied voltage was measured using a multimeter. After setting the voltage the signal generator was configured to trigger from an external 5V T.T.L source and the cell was connected.

The Time Frame Generator (T.F.G) was then programmed from the local computer. Programming consisted of setting the number of time frames, their duration, and the pause interval between frames. The T.F.G can send up to 5V T.T.L pulses at the start of any time frame. The pulses are used to synchronise detector time frames with the application of stimuli to

58

the sample. For the dynamic smectic-A experiment only one T.T.L pulse was necessary. This was programmed to appear at the beginning of the second frame. The T.T.L pulse was configured to trigger the signal generator (Figure 57).
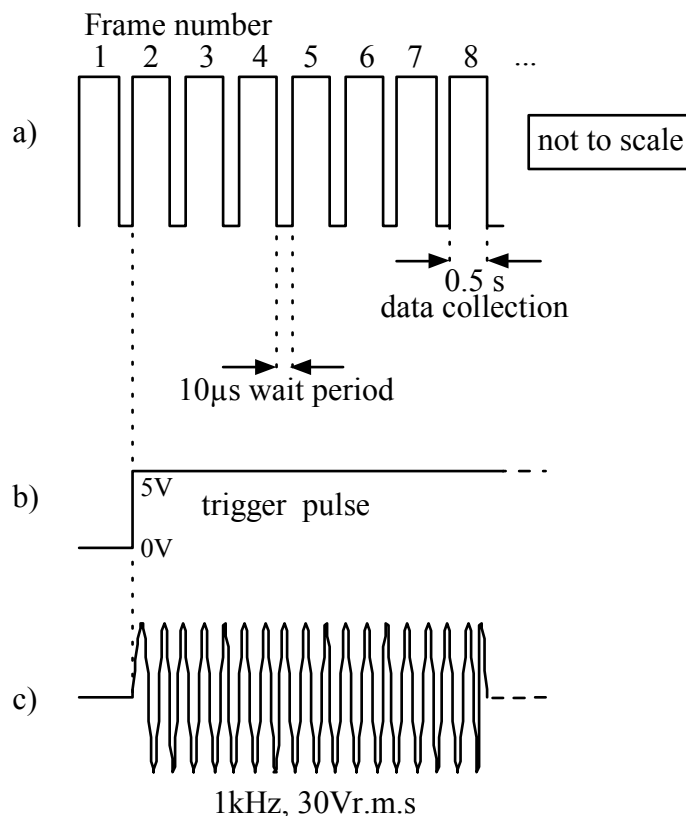
Figure 57: Experimental settings. a) Data collection time frames. (The combined wait periods add only 0.2ms to the total run time). b) Trigger pulse. c) Waveform sent to liquid crystal cell.

The sample was first aligned by heating it into the nematic phase and cooling it at 1°C/minute, to 51.5°C. The cell was then rotated to an angle of -20°. The x-ray beam was turned on. The T.F.G program was then run, thereby triggering the electric field to the sample and recording the resulting diffraction pattern as a function of time. The output file was saved, the sample was thermally realigned and the rocking angle was changed to -18°. The experiment was repeated at angular intervals of 2°, around to a rocking angle of +20°. One of the diffraction spots on the detector was chosen for the analysis. Its integrated intensity was determined for each time frame at each rocking angle. Rocking curves were then assembled, for each 0.5-second time frame.

4.5.4 X-ray results

The position of the diffraction spot on the detector remained constant throughout the experiment. This meant that there were no layer space changes during switching.

The figure below shows the normalised rocking curves obtained at each 0.5-second time interval during switching.
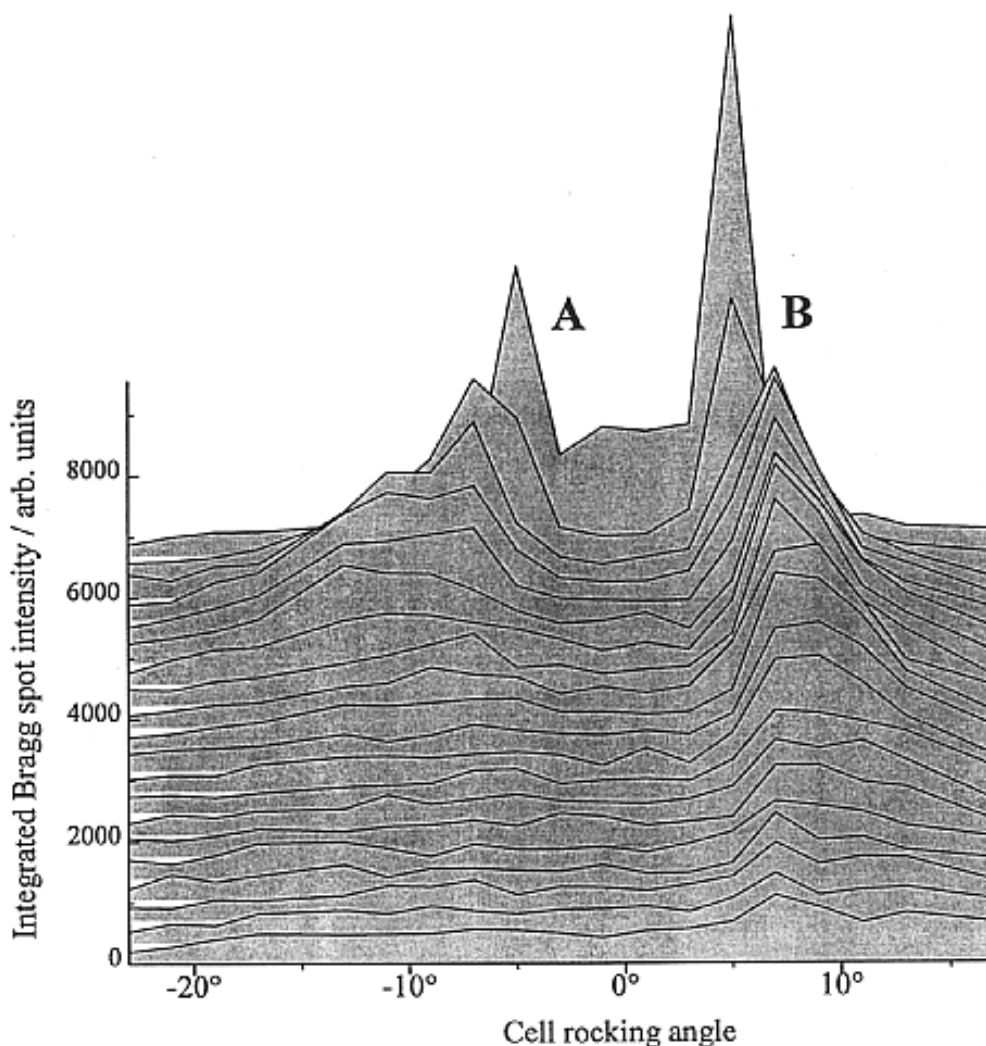
Figure 58: Assembled rocking curves from the dynamic x-ray experiment. Rocking curves are shown for each of the 0.5 second data collection frames.

Peaks A and B correspond to diffraction from each arm of the chevron structure. The fact that there are different initial peak heights does not necessarily mean that the chevron structure was asymmetric at the start of the experiment (see section 4.4.6). The persistence of peaks after application of the electric field indicates that the layers remain intact to some extent during switching. The angular shifts in peak position indicate that the two arms of the chevron structure rotate in opposite directions during switching, each towards its nearest cell wall (Figure 59). This is expected as it means that the molecules follow the easiest path. Such motion of the chevron arms is only possible if, either the layers fracture at the chevron interface, or an asymmetric chevron forms (Figure 59b). Layers A and layers B correspond to diffraction peaks A and B in Figure 58.
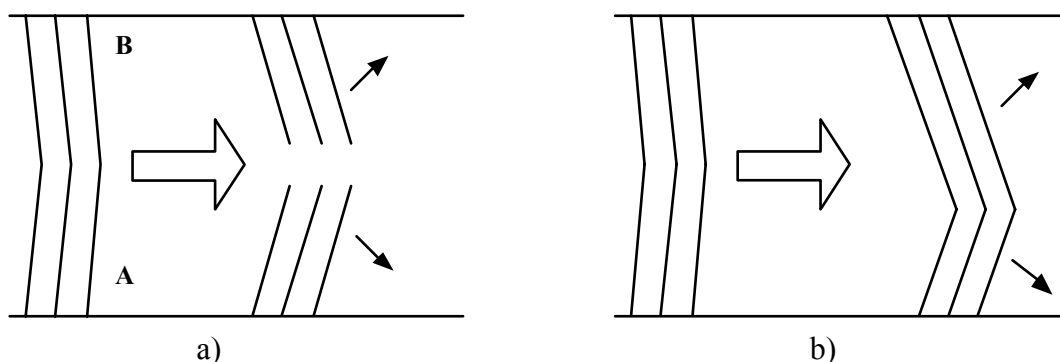
Figure 59: Possible rotations of the chevron arms during smectic-A switching. The angles are exaggerated. Case a *shows layer fracture. Case* b *shows formation of an asymmetric chevron structure.*

Figure 58 also shows that layers B rotate more slowly than layers A. The rotation is shown in more detail in Figure 60, where the angular position of each peak centre is plotted against time. The angular peak positions are plotted relative to the initial peak positions (both designated 0°). To make a comparison easier the movement of peak B is shown as if it were a movement in the opposite sense.
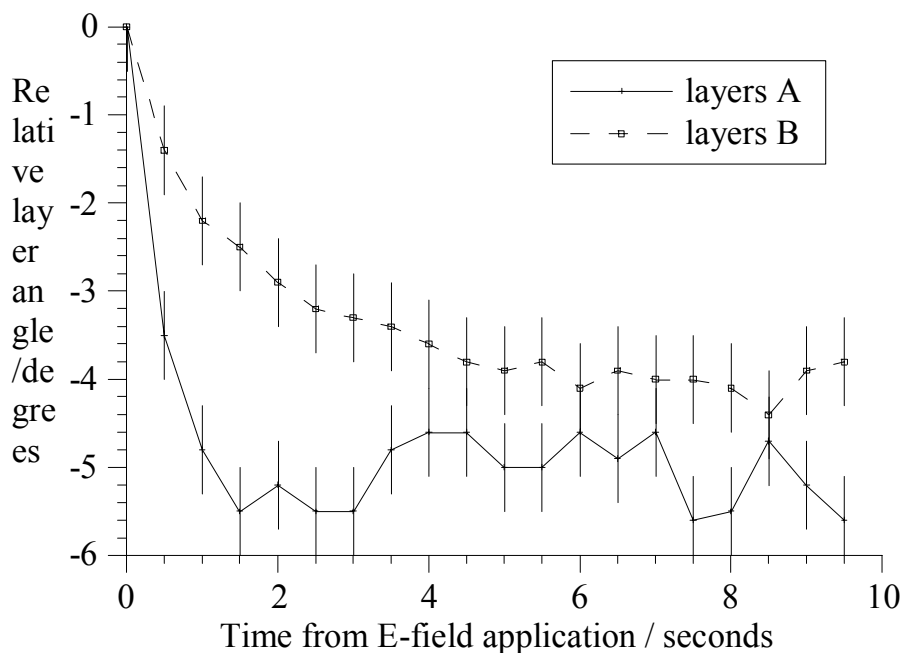
Figure 60: Rotation of the chevron arms during smectic-A switching.

The centre of peak A moves about 5° in the first two seconds and stays at this angle. Within the same time the centre of peak B moves about 3° and continues moving slowly, even towards the end of the experiment, ~9 seconds after field application.

Figure 58 shows that both peaks become more diffuse during switching, although peak A spreads out much more quickly than peak B. The diffuse peaks correspond to a spread of layer directions. This is probably due to the appearance of a multi-domain structure. The domains (to be precise the layers within them) can rotate at slightly different speeds, so as time progresses the angular distribution of layers increases. This is corroborated by the fact that the outer edge of each peak becomes more diffuse than the inner edge, implying the existence of a minimum rotation rate. Although the majority of the layers move through ~3° or ~5°, some of the faster moving layers can move through much larger angles in the same time. Figure 61, for example, shows the change in integrated diffraction intensity with time for a rocking angle of -16°. The plot indicates that a fraction of layers (from arm A of the chevron) sweep through an angle of ~-14° (-16° minus (-2°)), within several seconds of field application.
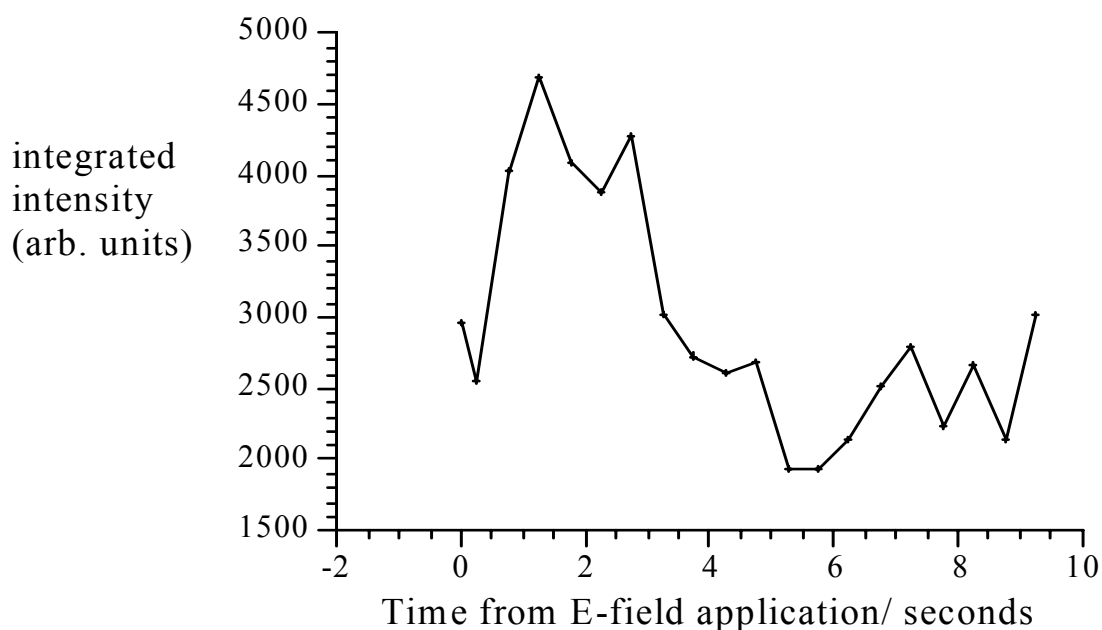
Figure 61: The integrated Bragg diffraction spot intensity as a function of time from field application for the cell rocking angle -16°.

Differences in the rates of layer rotation might be due to domain size, proximity to surfaces and proximity to the chevron apex.

The peaks (Figure 58) also become less intense during switching. The spread in layer direction due to a rotating multi-domain structure would lower the *maximum* peak intensity, but for each peak the overall diffracted intensity (the integrated intensity of all rocking angles under the peak - the peak area) would remain constant. Figure 62, below, shows a plot of the integrated intensity of each peak against time.
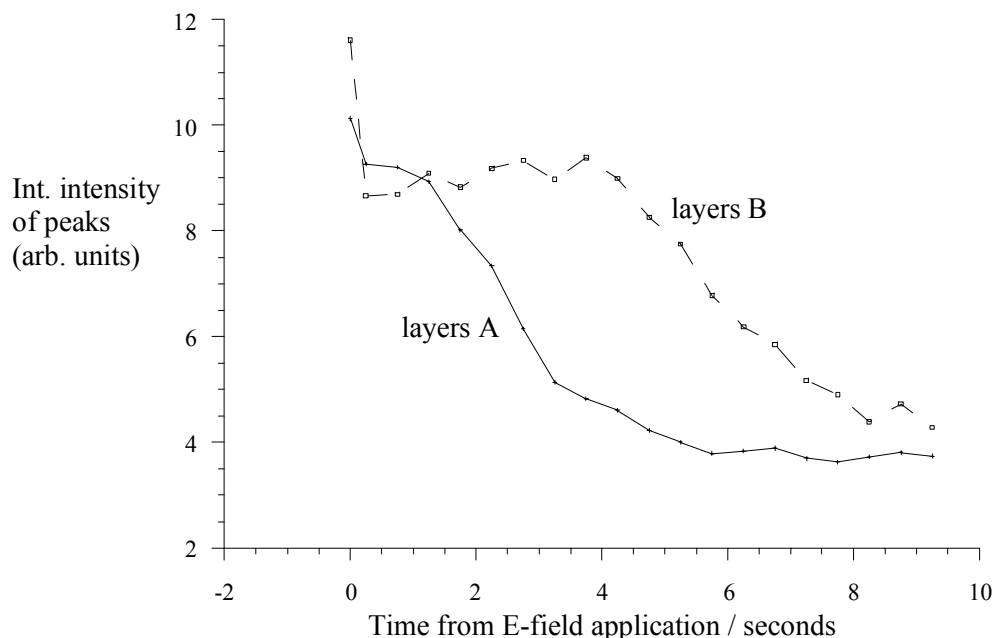
Figure 62: A plot of the total integrated intensity of each peak vs. time after application of the electric field.

Clearly the integrated intensity does not remain constant for the entire switching period, indicating that the spread in layer directions is not the only reason for the decreasing maximum peak intensities in Figure 58. The other possible reasons are:

i)   Increased mosaicity (alignment spread) in the plane of the cell faces during switching. The effect would have shown itself however, as an arcing of the diffraction spot on the detector. This was not seen.

ii)   Layer disruption. This seems likely as it is not possible for all domains to rotate co-operatively whilst maintaining layers. The driving force for the disruption is the electric torque on the molecules, so they would rotate co-operatively in nematic-like regions. Layer disruption also occurs within domain walls, so as the number of domains increases the diffraction peak intensity falls.

Figure 62 also tells us how long the layers A and B persist for. A measure of this time is the 90→10% decay time for the integrated x-ray diffraction intensity (based on the assumption that the switching is 100% complete by the last data frame). This decay time was calculated to be ~2s for layers A and ~6s for layers B.

The geometry of the experiment did not allow the final, switched layer structure of the system to be observed.

One question remains to be answered. That is, "why does one arm of the chevron (B) behave

noticeably differently to the other?" The different rotation speeds could be due to the formation of an asymmetric chevron structure early during switching, before layer disruption dominates. The initial chevron structure and the hypothesised asymmetric chevron structure are shown to scale in the figure below.
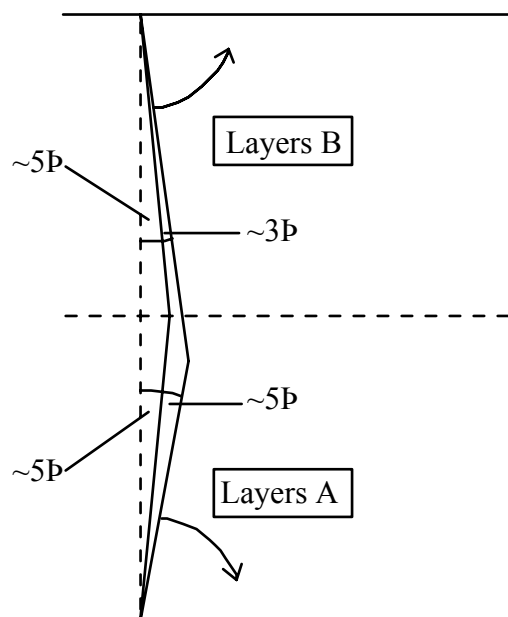
Figure 63: Scaled schematic diagram showing how an asymmetric chevron structure might form during the early stage of switching. The diagram is based on the experimental results, the angles marked correspond to the position of most of the layers after approximately two seconds (from Figure 59).

The asymmetric chevron idea explains the difference in rotation rates of the layers A and B, and explains why the intensity of the diffuse peak B is larger than that of the diffuse peak A during switching (Figure 58). But the idea implies an increase in the overall diffracted intensity from layers B during the initial stages. Figure 62 shows a slight *decrease*. The discrepancy could be because regions with cell defects undergo layer disruption early on in the process.

So why should the initial symmetric chevron become asymmetric? This could be due to the anti-parallel surface alignment rubbing: the P.V.A. induces a slight (~0.5°) director pretilt, that depends on the rubbing direction (Figure 64). In the initial chevron structure the director opposes the pretilt direction at both surfaces, thus introducing strain at the surface regions. When layers A begin to rotate, this strain decreases and the rotation is thus aided by the presence of pretilt. For layers B however, the strain increases and the rotation is hindered. In this way the speed of layer rotation will differ between layers A and B, forming an asymmetric chevron structure.
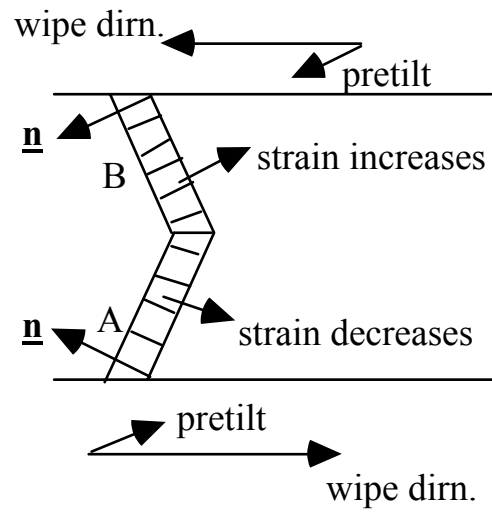
Figure 64: The effect of anti-parallel alignment rubbing on the smectic-A switching process. The angles are exaggerated for clarity.

4.5.5 Photographs
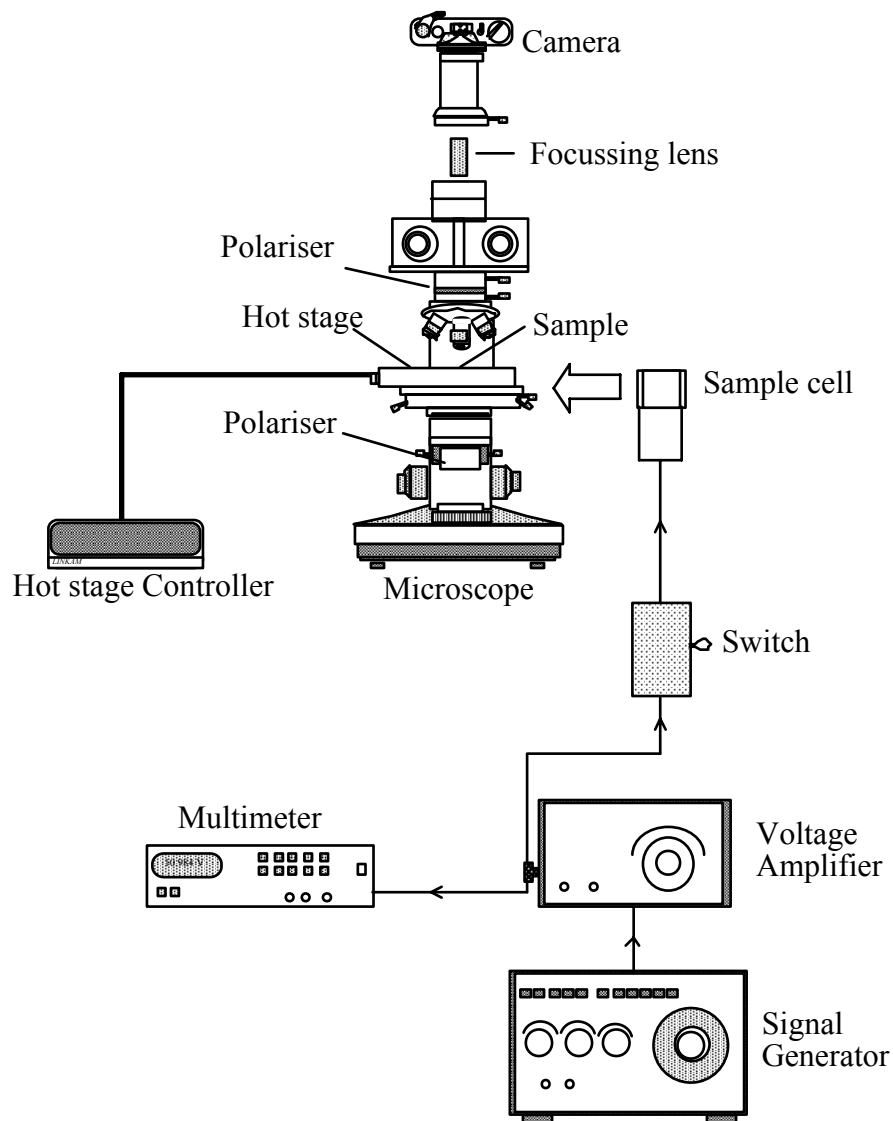
Figure 65: The apparatus used for checking cell alignment and taking photographs of the smectic-A switching process.

The sample cell is held on the heating stage (see section 4.4.2). The heating stage is placed on the rotation stage of an optical microscope (BH2- Olympus). The polarisers (of the microscope) are crossed. The apparatus for electric-field application is the same as that used in the dynamic x-ray experiment, (section 4.5.5) except that the signal generator is set to run continuously, rather than being triggered. The voltage to the cell (30Vr.m.s, 1kHz) is interrupted by a switch when required. A camera (Olympus OM1) is attached to the trinocular headpiece of the microscope, which is fitted with a x10 objective and a focussing lens. The camera was loaded with a 400 A.S.A film. The liquid crystal was brought into focus at the camera film position.

The cell orientation with respect to the polarisers was set so that the unswitched cell gave

maximum brightness (this occurs when the director is at 45° to the polarisers). Photographs were then taken before switching, and at approximately 1s, 2s and 3s after electric-field application. The photographs are shown in Figure 66.
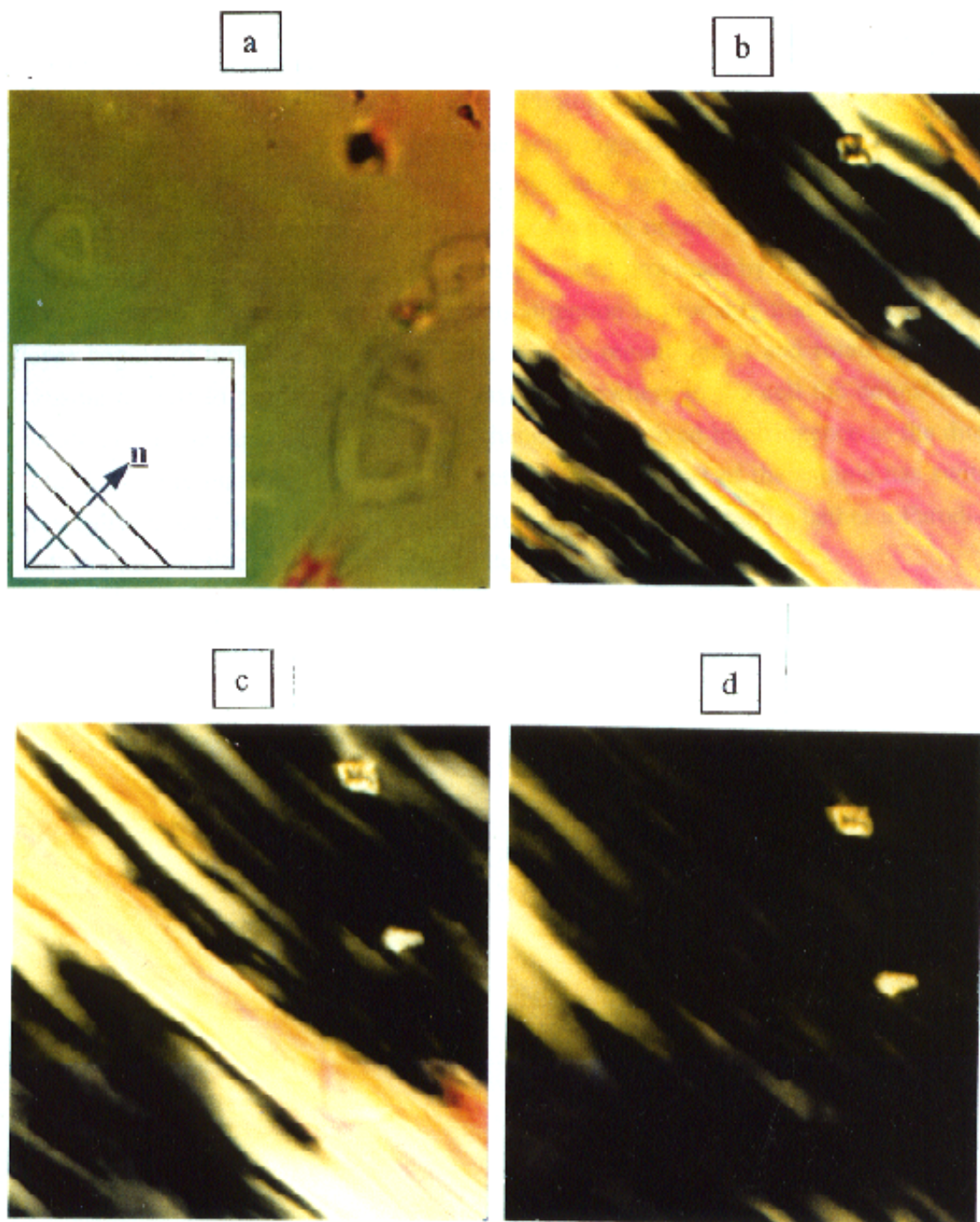
Figure 66: Photographs of the smectic-A switching process taken with the cell between crossed polarisers. Time from field application: a) 0s, b) ~1s, c) ~2s, d)~3s.

Photograph **a** shows the cell before switching. The director and layers are indicated schematically. The rainbow colours indicate a slight variation in the thickness of liquid crystal (see section 4.3). The photograph also shows that some defects are present before switching. The change of defect brightness suggests they are focal conic defects. Photograph **b** shows that switching progresses quickly close to defects, suggesting that the process nucleates at defect sites. This is probably due to the lower surface anchoring energy near these sites. Photograph **b** also shows that switching occurs more readily parallel to the layers, as observed previously by Jàckli and Saupe [93]. This preference in direction is probably because the layers try to remain intact once one end starts rotating. Elsewhere in the cell the colour changes due to a change in perceived birefringence as the director rotates into the plane of the page (see section 2.4.3). Most of the sample has switched (optically) after 3 seconds. It is unclear from the final photograph whether a Parodi-type defect array (section 2.4.2) exists after switching.

4.5.6 Electro-optic measurements
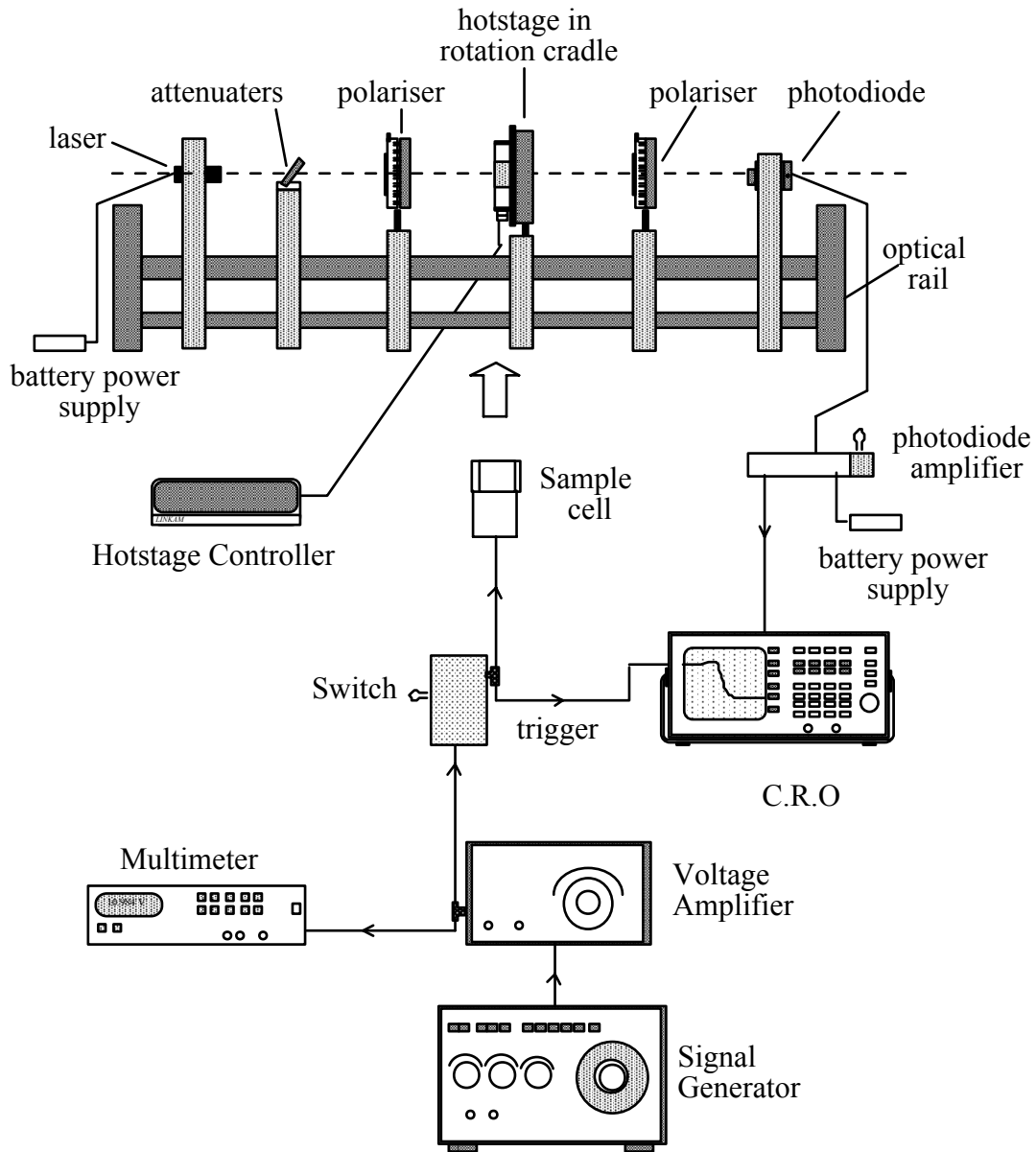
Figure 67: Electro-optic measurement apparatus.

The optical equipment is mounted on an optical rail, which was designed by the author and built by the physics department workshop. The light source is a battery powered, collimated 5mW laser-diode (Sumichem Optoelectronics Ltd.). The lasing wavelength is 670nm (red). The diode has a focussing lens which was adjusted to focus light at the sample, giving a beam spot size of ~0.5mm diameter. The incident light intensity was attenuated so as not to saturate the photodiode. The sample lies between sheet polarisers, which are crossed with an accuracy of +/-0.1°. The cell was mounted on a heating stage (section 4.4.2), which was itself mounted in a manual rotation cradle. This allowed the cell to be rotated about the beam axis. The cell face was brought perpendicular to the laser beam by moving the cell so that the (weak) reflected beam

69

coincided with the laser head. The cell temperature was held at 51.5°C, as in the dynamic x-ray experiment. The transmitted light was detected by a medium area photodiode (RS BPX65).

The photodiode signal was amplified using a home-made low-voltage amplifier, powered by battery (Figure 68).
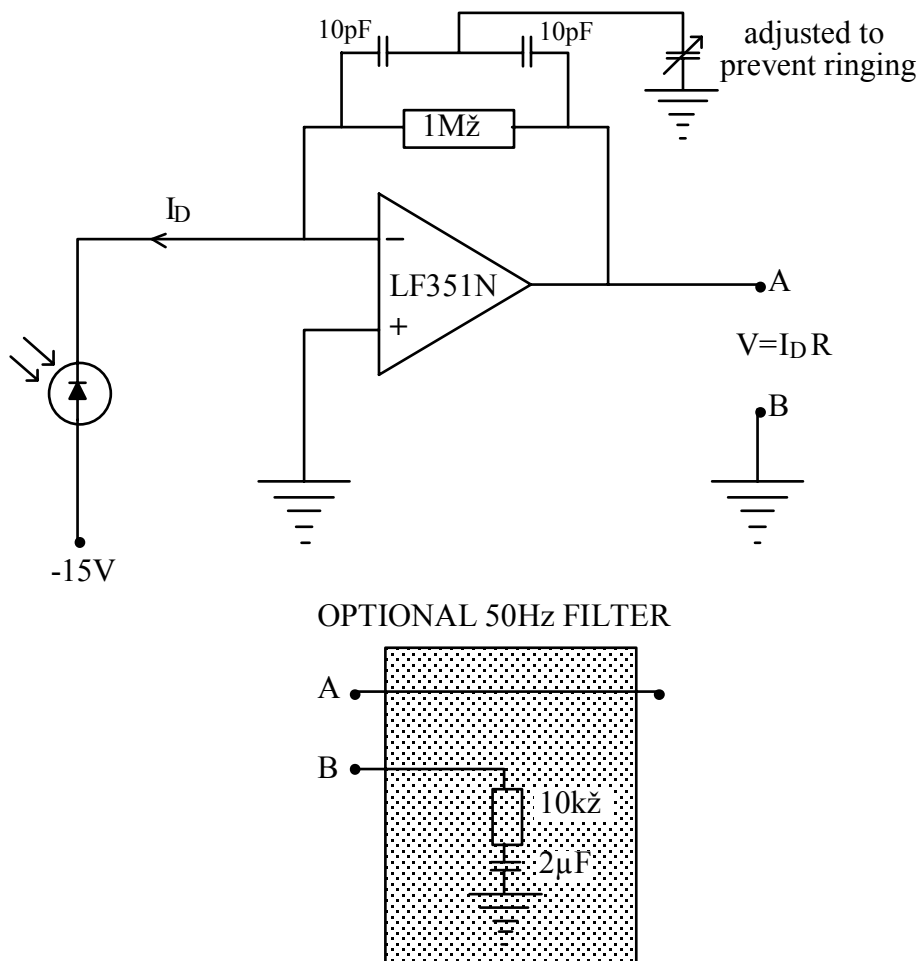
Figure 68: Photodiode amplifier circuit.

The photodiode current is proportional to the output voltage. A 50Hz mains filter was used for low response time, smectic-A studies (but not for the ferroelectric studies). The photodiode output was measured using a digital storage oscilloscope. The electric field generating equipment was the same as that used in the microscopic studies (section 4.5.5) except that the voltage applied to the sample was also used to trigger the oscilloscope. The waveform was a 30Vr.m.s, 1kHz sine wave, as used in the dynamic x-ray experiment.

Before the experiment began, a subsidiary experiment showed that the amplified photodiode voltage was proportional to light intensity (for the voltage ranges to be used). The photodiode response time (100%-0%) was about 6μs, which was sufficiently fast for all experiments.

The unswitched smectic-A cell was placed in the beam path and rotated to give maximum light intensity, as measured on the oscilloscope. This occurred with the director at 45° to the

polarisers. The switching process was then started. The resulting oscilloscope trace is reproduced in Figure 69.
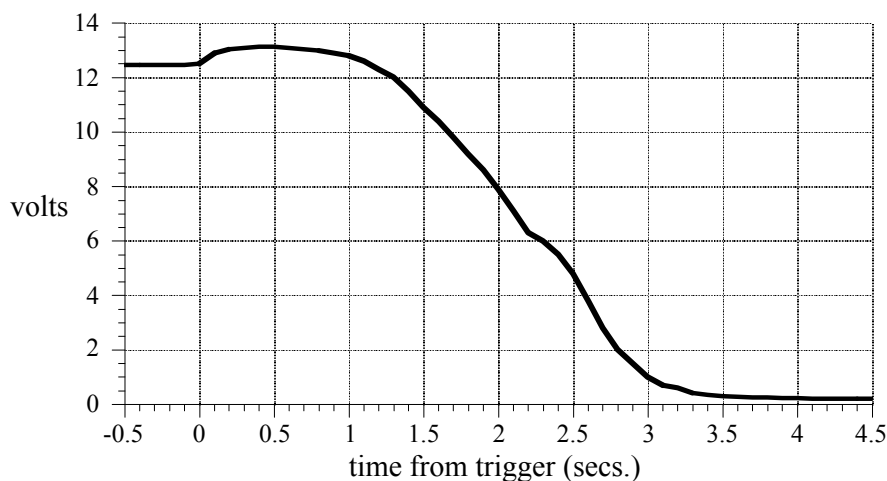
Figure 69: The change in transmitted light intensity during smectic-A switching.

The initial rise in light intensity can be attributed to increased light scattering from domain walls. The complex decay following can be explained in conjunction with the switching photographs (section 4.5.5): The detected response depends on the position of the laser beam spot with respect to cell defects. In general the spot will overlap fast and slow switching regions, giving a complex decay curve.

The optical switching time (90%–10%) for the entire beam spot area, was measured using the oscilloscope. The mean switching time was found to be 3.7 seconds ($\sigma = 0.5$ s).

4.5.7 Correlation of X-ray data and electro-optic measurements.

It is difficult to make a direct correlation of x-ray and optical data for the following reasons:

i)   The electro-optic measurements are performed with the cell face perpendicular to the beam, so that only the projection of the director is measured. It is impossible to distinguish, for example, whether the molecules are pointed towards a particular cell face or away from it by the same angle.

ii)   The electro-optic switching profile is dependent on the position of the light beam relative to cell defects. This factor alone could explain the complex response curve, but does not exclude, for example, the affect of the different rotation rates for each of the chevron arms (section 4.5.4).

The electro-optic measurements serve therefore, not to confirm the proposed model, but at least to allow its possibility. The photographs are more helpful, although they provide additional information rather than a clear correlation with layer behaviour.

4.5.8 Proposed model for switching

•1   The cell initially has a symmetric chevron structure, with a chevron angle of ~10°.

•2   When an electric field is applied the layers rotate, introducing stress in the cell, which is relieved by a multi-domain structure.

•3   Each arm of the chevron rotates towards its nearest cell wall.

•4   Layer rotation begins near cell defects. Rotation propagates along the layers, in preference to cooperative rotation with neighbouring domains.

•5   Because of the P.V.A pretilt, the initial layer rotation is slightly asymmetric

•6   Layer rotation occurs at different rates within each domain.

•7   After a few seconds the asymmetric chevron structure breaks up. This is probably due to the large increase in elastic forces at the chevron apex.

•8   After the chevron breaks up there are more domains, and also nematic-like regions.

•9   The chevron arms fracture in many places. The long arm of the asymmetric chevron does not fracture as quickly as the smaller arm. This might be because fast-moving layers are more likely to break when they hit a domain wall in their path.

•10   The optical switching time (~3.7s) is longer than the time for one set of layers to disrupt (~2s) but less than the time for the other set of layers to disrupt (~6s). The reason for this is not clear.

•11   The experimental geometry did not allow confirmation that the final switched state was layered, although it is believed that a layer structure would have reappeared once the molecules had stopped rotating.

4.6 Summary of the Smectic-A Experiments

An unusual chevron structure has been shown to exist in the planar aligned smectic-A liquid crystal phase of the material S3, from Merck-BDH Ltd. The reason for the chevron structure was shown to be the reduction in layer thickness on cooling from the nematic phase.

The behaviour of the smectic layers during switching has been observed for the first time ever, using the technique of time-resolved low angle x-ray diffraction. Supplementary information was obtained from photographs of the switching process, and electro-optic measurements of the director behaviour.

A model of the switching process has been proposed. The basic feature of the model is the rotation of intact layers during the early stages of the switching process.

Chapter 5

FERROELECTRIC EXPERIMENTS

5.1 Introduction

This chapter gives details of the apparatus and procedures used in the experiments on ferroelectric liquid crystals. Many details are the same as those for the smectic-A experiments. This chapter also presents the results that were obtained for the ferroelectric cell and discusses them in the light of the various models introduced in chapter 2.

The first objective was a study of the effect of high electric fields on the chevron cell structure - the "static" experiment. The second objective was a study of the layer behaviour during low electric field director switching - the "dynamic" experiment.

The static experiment consisted of an x-ray rocking experiment at various voltages. (The rocking curve at 0V represents the initial room temperature layer structure before the dynamic experiment.) The cell was photographed at each voltage in the static experiment.

The dynamic experiment consisted of x-ray measurements and electro-optic measurements. The electro-optic measurements revealed the timescale of director reorientation. This timescale was divided into timeframes that were used to monitor layer changes during switching, using x-rays. The sample was switched and the layer diffraction characteristics were measured as a function of time. The experiment was repeated many times to acquire sufficient radiation counts in each timeframe.

5.2 Liquid Crystal Material

The main requirements of the ferroelectric liquid crystal were the presence of a nematic phase (for good alignment), and a smectic-A phase (to give a symmetric chevron structure on cooling), in a low molar mass system. SCE13 was chosen. SCE13 is the commercial name for a mixture of low molar mass ferroelectric compounds from Merck-BDH Ltd [78]. The company is unwilling to release details of the chemical composition. SCE13 possesses the following phase sequence:

$$K \xrightarrow{\;<-20\ C\;} S_C^* \xrightarrow{\;60.8\ C\;} S_A^* \xrightarrow{\;86.3\ C\;} N^* \xrightarrow{\;100.8\ C\;} I$$
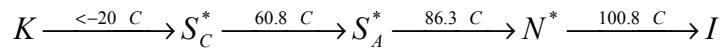
The dielectric anisotropy of SCE13 at room temperature is approximately -0.5.

5.3 Cell Design

The cell design and fabrication procedure is very similar to that used in the smectic-A experiments (see section 4.3). The only difference is a spacer thickness of 2μm. The overall cell thickness (spacers+glue) was 4μm (+1μm, -1.25μm).

5.4 Static Experiment: High Electric Fields (E.F.T)

5.4.1 Apparatus and experimental procedure

The initial (0V) layer structure within the ferroelectric cell was determined by an x-ray rocking experiment, in the same way that the initial layer structure of the smectic-A cell was determined. The apparatus and general experimental procedure were the same (see section 4.4.2). The only differences were as follows:

i)   The ferroelectric experiment was conducted at 25°C (after cooling the cell at 1°/minute from a temperature of 90°C (in the nematic phase)).

ii)   The thinner ferroelectric samples required a longer x-ray exposure time (1 min.).

iii)   The larger expected chevron angle in the ferroelectric cell necessitated rocking through a greater angle (~-30° to ~+30°). (The rocking angle step size used was 1°.)

Having confirmed the presence of a chevron structure, the effect of large electric fields on the structure, was investigated. The apparatus was the same as that used for determination of the initial cell structure, with the addition of electric field equipment. The electric field equipment was used to supply and measure the D.C. voltage to the cell. Rocking experiments were conducted at each chosen voltage. The experimental procedure was basically the same as that used in determination of the initial layer structure. The cell was rocked from -30° to +25° in 1° steps. The voltage was increased, between rocking curves, in 2V steps until a structural deformation was seen. The experiment was then repeated at 0V to see if the transformation was reversible. Whenever it was clear that no deformation had occurred, the sample was rocked through the featureless central region (-15° to +15°) in larger, 5° steps. The data was normalised (section 4.4.5). The results are shown in Figure 70.

5.4.2 Results of the ferroelectric static X-ray experiment
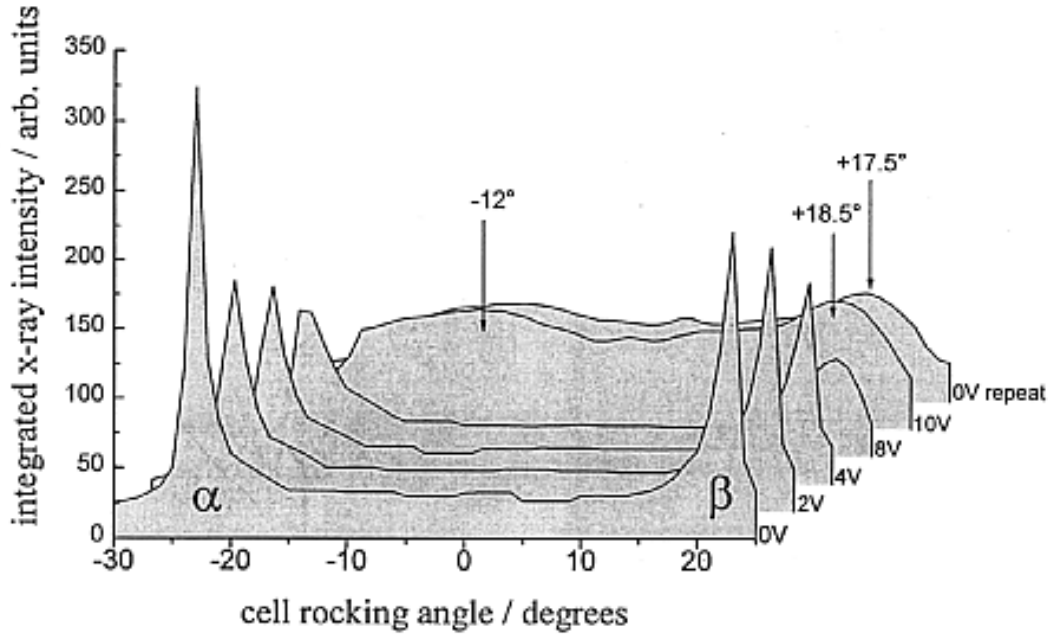
Figure 70: The effect of high electric fields on the chevron structure. The peaks marked α and β correspond to the sets of layers forming each arm of the chevron structure.

The data file for the 6V rocking curve was corrupted and does not therefore appear in Figure 70. The figure shows an initial chevron structure within the cell; the chevron angle being 22.5°+/-0.5°.

Voltages up to 4V D.C do not affect the structure. At ~8V D.C structural changes take place: The chevron arms become slightly obtuse, although there is no change in the chevron angle at the cell walls. Between 8V and 10V D.C there is a significant structural alteration as the sample begins to adopt a bookshelf structure. (For the sample thickness of 4μm (+1μm, -1.25μm), 10 volts corresponds to an electric field strength of 2.5V/μm (+1.1V/μm,-0.5V/μm)). The chevron structure is not completely removed, however: The chevron arms become obtuse, and the chevron angle decreases. The decrease is not the same for both arms (layers α and layers β (Figure 70)). Layers α rotate, on average, to approximately -12°; a rotation of ~10.5°. Layers β rotate, on average, to approximately +18.5°; a rotation of only ~4°. The structural change is shown schematically in Figure 71.
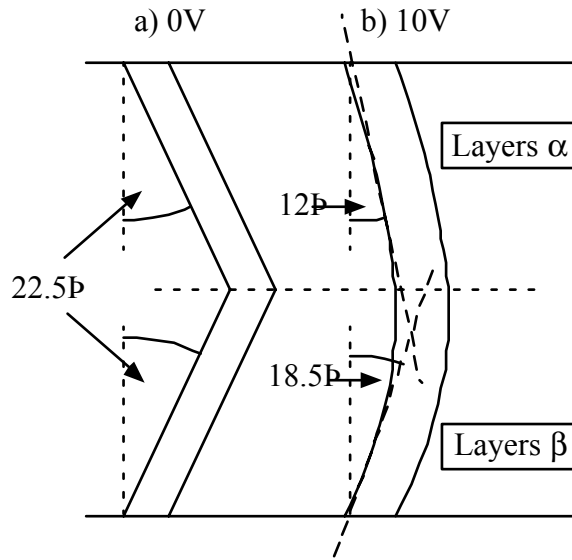
Figure 71: Scale drawing showing the formation of an asymmetric, low-tilt obtuse chevron structure on application of a high electric field (10V across a 4µm cell) to a ferroelectric liquid crystal.

The structural asymmetry might be due to the anti-parallel P.V.A rubbing and the subsequent difference in director strain at each surface (see section 4.5.4).

The repeated rocking curve at 0V shows only a slight change from the 10V rocking curve: a further rotation of layers β, to about 17.5°. This extra rotation is in a direction contrary to that which would be expected from surface alignment forces. It could however be because the strain at the chevron apex is relieved by layers α "pulling" the other layers. The slight differences between the 10V and 0V rocking curves shows that the process is essentially irreversible

In addition to the rocking curve measurements, the Bragg spot on the area detector was monitored. (See section 2.5.3.5 and Appendix B.) Figure 72 shows the raw data for the cell angle of 0° and an applied voltage of 10V (a similar picture at 0V (before E.F.T) showed no structural data).
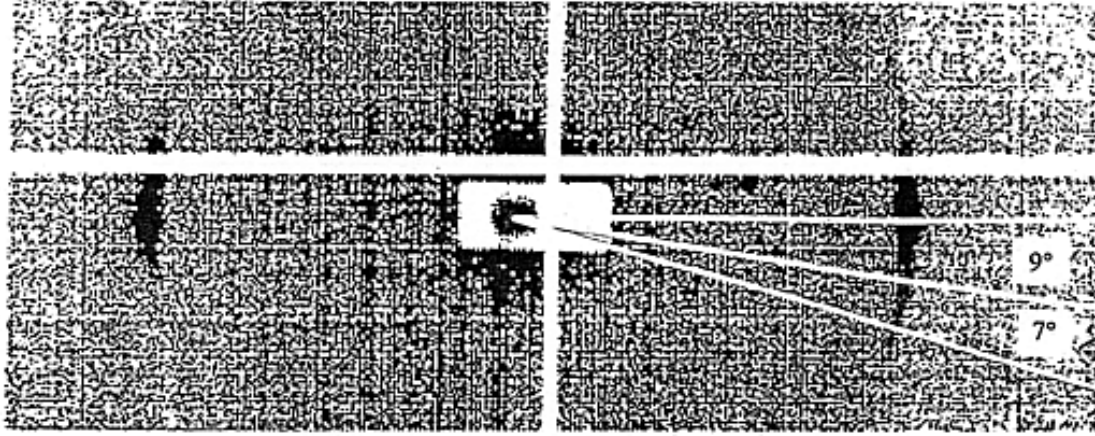
Figure 72: Bragg spot arcing due to E.F.T

Bragg spots can be seen to emerge at an angle of 0°, in accordance with Figure 70. The spots arcing can be partly attributable to the mosaicity in the plane of the sample (alignment spread). The mosaicity was measured by determining the angular spread of one of the Bragg spots in the 0V experiment. The result was +/-9° about the global director. As shown in Figure 72, the mosaicity alone does not account for the arcing, which measures up to ~16°. This indicates that there has been a rotation of layers in the plane parallel to the cell faces. The continuous arcing suggests that the rotated layers are not sharp, as portrayed by Srajer *et al* [54], but that they are obtuse. The irreversibility of the process implies that even the layers at the surface have rotated. The most probable layer formation is shown in Figure 73.
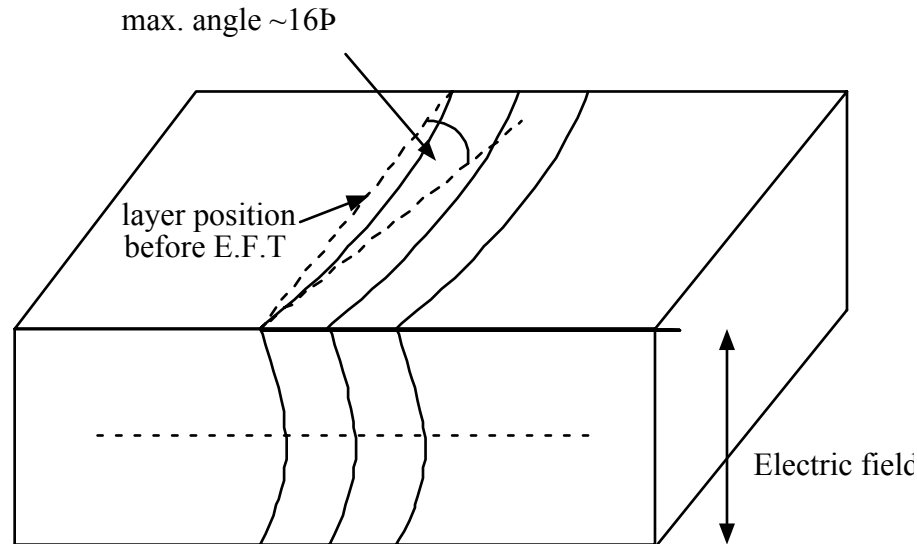
Figure 73: Rotation of layers with E.F.T.

5.4.3 Photographs

Photographs of the sample were taken before electric field application, and after 10V application

(with the field removed), using a microscope with crossed polarisers, as discussed in section 4.5.5. The cell was aligned with the polarisers, so as to give the best observation of textural changes in the area examined with x-rays.

Figure 74: Photographs of the ferroelectric cell a) before and b) after E.F.T

The photographs show clear structural changes. The colour changes are due to the change in perceived birefringence as the local director orientation changes. The fine lines approximately parallel with the director in photograph **b** are due to the formation of striped domains from zigzag defects. These zigzag defects were present in the cell, as shown later in Figure 83. They cannot be seen in photograph **a** because of the poor contrast between domains when an electric field is not applied. The striped defects are not as obvious as those reported by other authors [62]. The reason for this is probably the incomplete chevron destruction observed in this case. A larger electric field applied to the cell might have caused complete conversion to a bookshelf structure within the cell and a sharper layer reorientation at the surface.

5.5 Dynamic Experiment: Low Electric Fields

5.5.1 Introduction

The purpose of the dynamic experiment was to look at the layer motion that might occur during standard switching in a SSFLC cell (as the molecules swing around the cone defined by the tilt angle). The electric fields are low in comparison with those that irreversibly distort the chevron structure (E.F.T). The two switching states will be referred to in this section as UP and DOWN, although the absolute direction of the spontaneous polarisation isn't important. The chosen switching waveform was a +/-6V square wave. This voltage was below that necessary for E.F.T (~8-10V, as measured in section 5.4) and yet reasonably high, in the belief that potential layer motion would be more noticeable with faster switching. The sample temperature was nominally chosen as 54.5°C (giving a convenient switching time). The experiment involved three investigations, as follows:

i)   A determination of the timescale for switching (at the chosen temperature/voltage). This consisted of an electro-optic experiment to monitor the birefringence changes.

ii)   A partial x-ray rocking experiment on the unswitched structure, using small rocking angle steps to accurately locate one of the two (chevron) positions of maximum diffracted intensity. The apparatus and experimental procedure are the same as those used in determination of the initial layer structure (section 5.4) but with a resolution in rocking angle of 0.072°. The results were only pertinent to the experimental procedure below (iii). They were not in themselves relevant to this thesis and were thus discarded.

iii) A time-resolved x-ray experiment to monitor layer behaviour upon electric field application to the cell (with the cell sitting at the angle of maximum diffracted intensity, as determined above).

5.5.2 X-ray experiment

The apparatus is the same as that used in the dynamic smectic-A experiment (section 4.4.2) although the experimental procedure is different and the sample temperature was 54.5°C. After determining the timescale for switching (~200μs) the T.F.G was programmed to provide 26 data capture timeframes, each 20μs long and having a preceding 10μs wait period. A 10μs T.T.L trigger pulse was programmed to appear at the beginning of the second frame. The subsequent 25 frames allowed data capture over a period of 25x30=750μs. The trigger pulse was sent to the

signal generator, which was programmed to supply a single burst (one cycle of a square wave), on receipt of an external trigger. The square wave voltage was +/-6V and its frequency 1.5kHz, as in the electro-optic experiment. In common with other signal generators, a triggered square wave must begin its cycle at some phase angle other than 0° or 180° (it was not possible to have the output at 0V initially). The signal generator output was thus set to +6V and programmed so that the trigger pulse would start a single square wave from a phase angle of 90° i.e. 1/4 cycle high, 1/2 cycle low (-6V), 1/4 cycle high. The output would then remain high. The square wave period was checked to be within +/-~0.1μs (using the oscilloscope). The error in the starting phase angle was quoted in the signal generator manual, as +/-2° in a 360° cycle. This corresponds to a +/-5 μs error in the time of polarity reversal (the switching "edges"). The rise and fall times of the edges themselves were ~40ns i.e. insignificant. The timing errors of the T.F.G system were sub-nanosecond and therefore insignificant.

The T.F.G was programmed to repeat the experiment many times, the trigger pulse each time ensuring that the detector timeframes were synchronised with the electric field. The data in each frame was accumulated and monitored in real time on the graphics display. This is referred to as "strobing". The experiment was interrupted when significant intensity levels were obtained for each timeframe. This corresponded to approximately 2 seconds total data collection time in each frame, giving an overall experiment time of about 52 seconds. The timeframes, electric field behaviour and sample response are illustrated schematically in Figure 75.
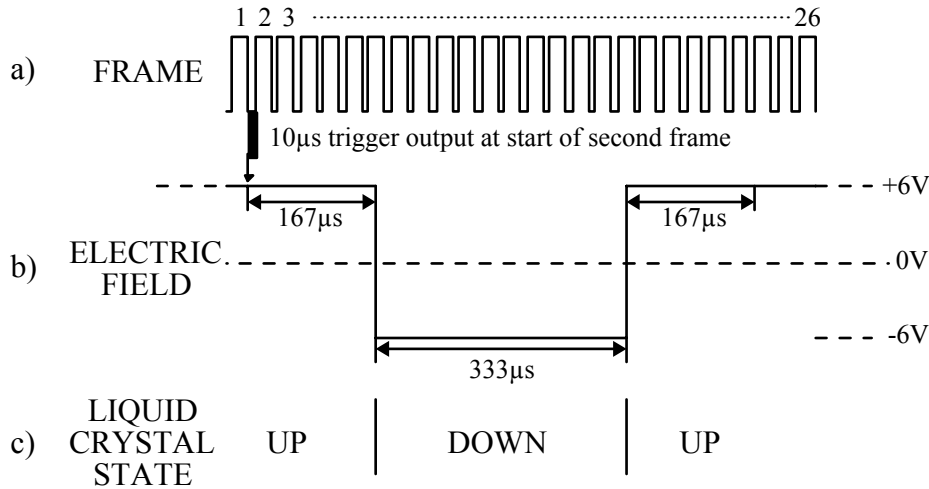
Figure 75: a) timeframe settings. Timeframes consist of a 10μs wait period, followed by a 20μs data capture period. b) the triggered 1/4 cycle, 1/2 cycle, 1/4 cycle square wave electric field. c) the liquid crystal stable state during switching.

The experiment was conducted with the cell rocked to the chevron angle (one of the positions of maximum diffracted intensity (see section 5.5.1)). The experiment was only conducted at this one rocking angle due to time constraints. The area detector allowed three pieces of information to be simultaneously obtained:

i)   Layer space changes by Bragg angle measurement.

ii)   Chevron angle changes. A decrease in diffracted intensity would indicate possible

movement of layers to another angle.

iii)   Changes in surface layering direction (angular changes in the diffraction spot)

5.5.3 X-ray results

There were no *observable* changes in layer spacing during switching.

Figure 76 and Figure 77 show intensity contour plots of the raw data on the detector corresponding to, an UP and DOWN state respectively. The main beam strikes the detector to the left. Both plots have been rotated so as to make the UP state diffraction spot lie on the equator. This makes the differences between the plots easier to see.
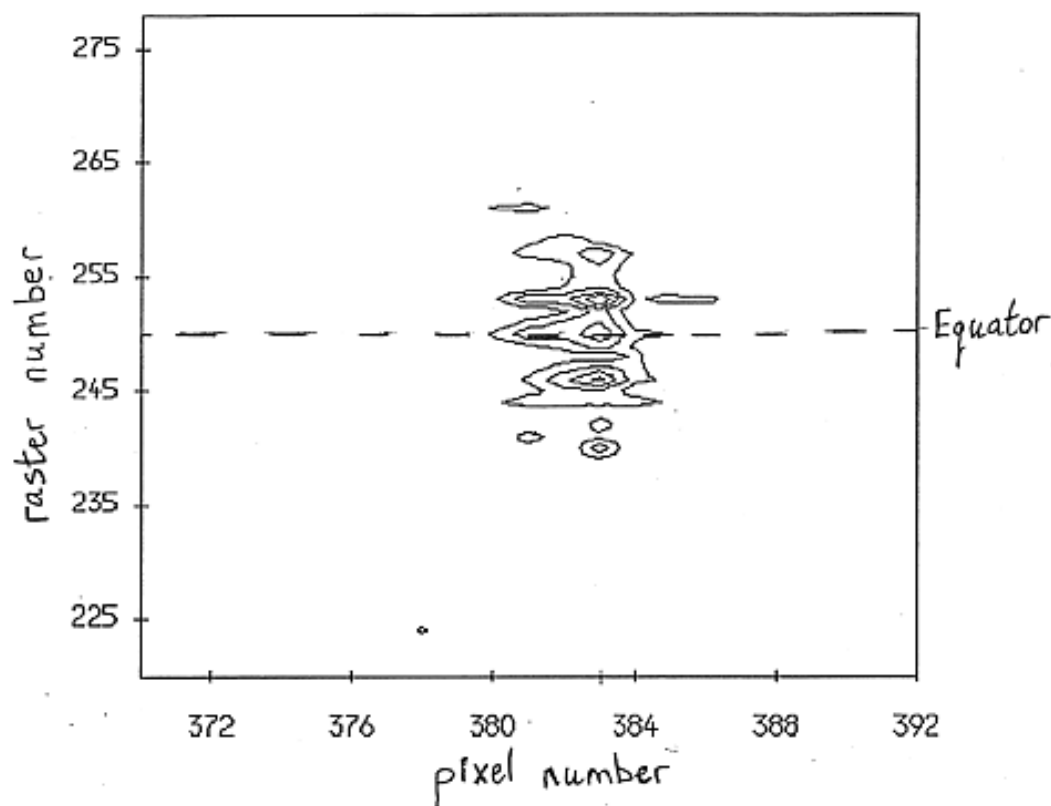
Figure 76: An x-ray intensity contour plot of the raw data in the UP state.
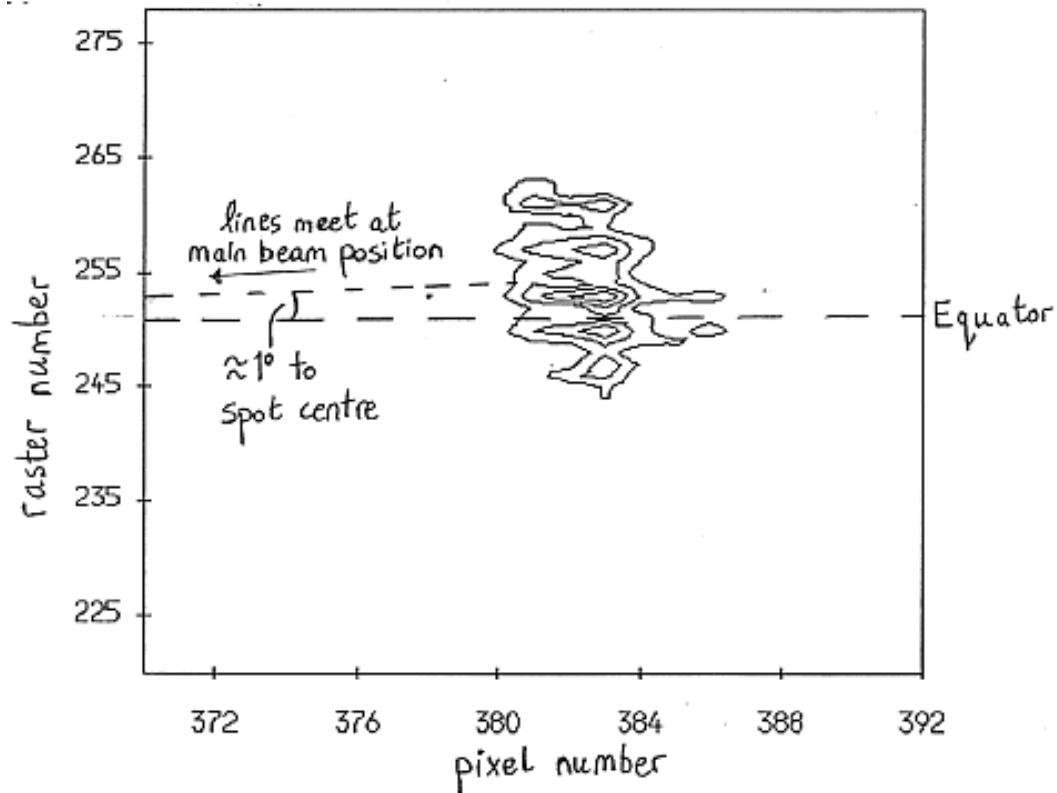
Figure 77: An x-ray intensity contour plot of the raw data in the DOWN state.

The changing spot angle relative to the equator indicates a rotation of the layer direction <u>in a plane parallel to the cell face</u>, on moving from an UP to a DOWN state (shown schematically in Figure 78).
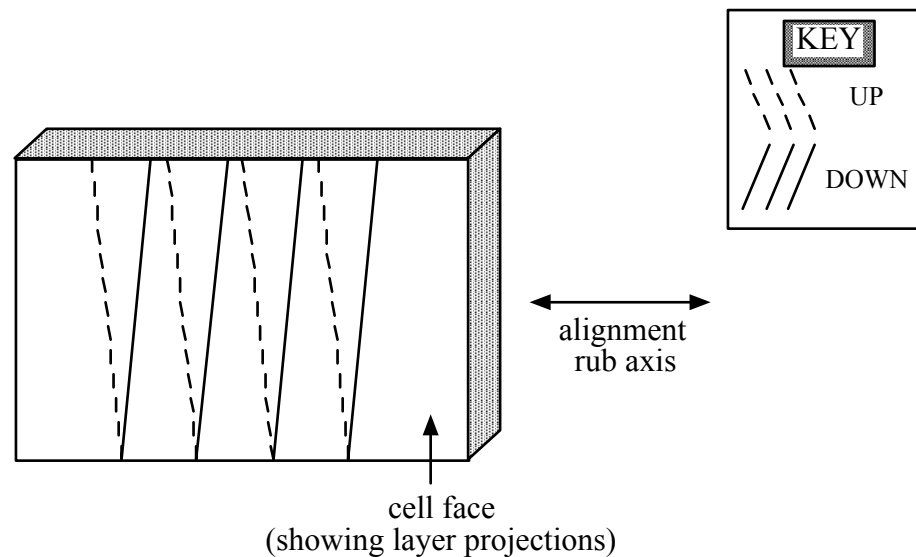
Figure 78: Schematic illustration of experimentally observed layer rotation in the plane(s) parallel to the cell faces. The angles are greatly exaggerated.

The angular rotation was quantified by calculating the position of the diffraction peak centre as a function of time during switching. The main beam position on the detector was easily identified from the fraction of beam intensity penetrating the beamstop. The Bragg peak centre was then determined, relative to the main beam position, by finding the centre-of-area of the peak in terms of horizontal and vertical pixel number (see section 4.4.5.1.) The angle of the diffraction peak, with respect to the equator, was then calculated using simple trigonometry, as shown below.

$$\theta = \arctan(Y/X)$$
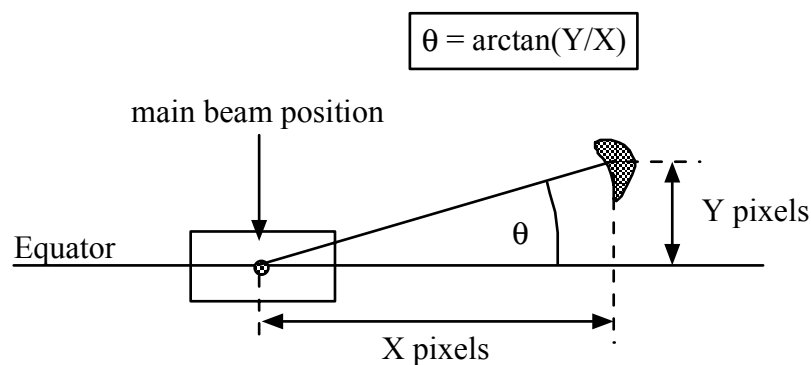
Figure 79: Determination of diffraction peak angle relative to the equator.

The angular position is plotted as a function of time, in Figure 80.
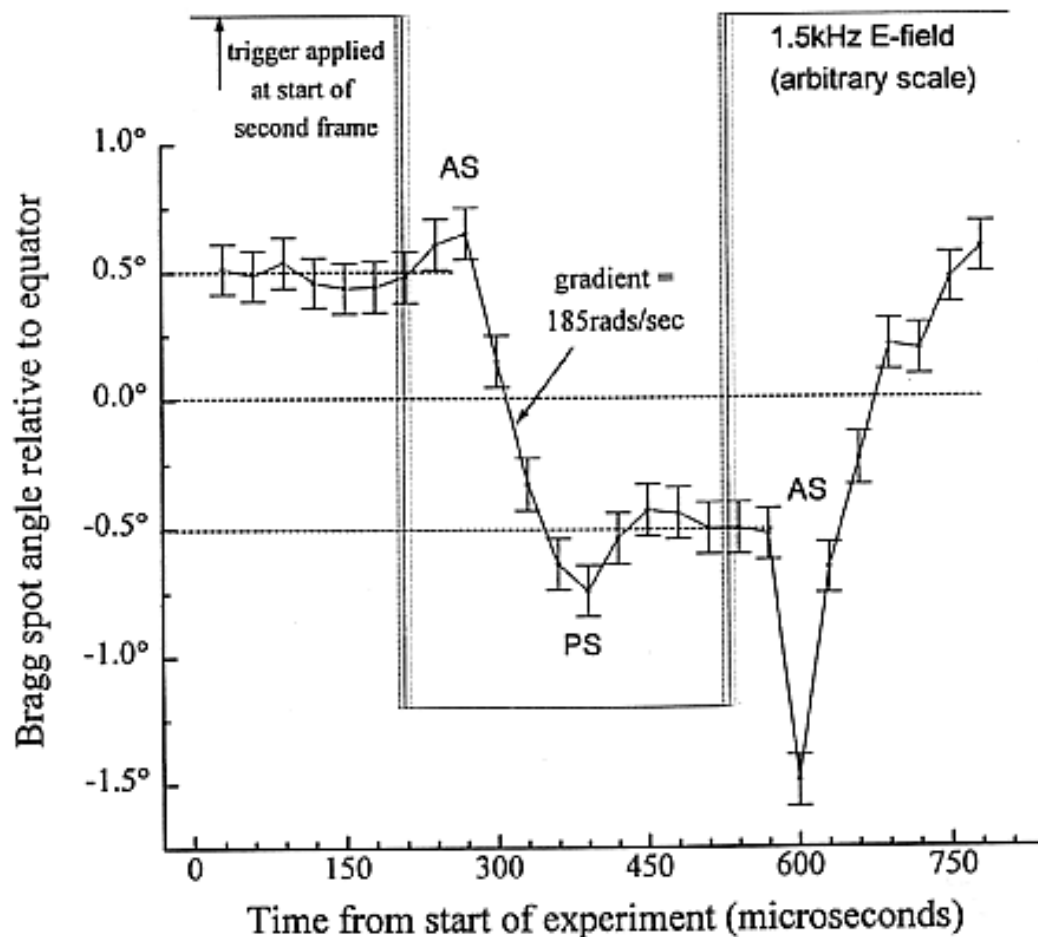
Figure 80: The angle of the Bragg diffraction spot relative to the equator, as a function of time during switching. Each data point represents the accumulated intensity in the preceding 30μs.

The angles have an error of +/- 0.05°. In the UP state the layers sit at an angle of about 0.5°. In the DOWN state they sit at about -0.5°. The angular layer separation of stable states is thus about 1°. Whenever the field direction is changed the layers first rotate in such a direction that increases this angular separation. The periods for which this occurs are marked on Figure 80 as AS (Ante-Switch). They last for approximately 75μs. Starting from the UP state the AS maximum angle increase is ~0.2°, whereas starting from the DOWN state it is ~1°. The reason for this asymmetry is not clear. Following the AS period the layers reverse their direction of rotation, and rotate, at an angular velocity of ~185 radians per second, towards the new stable state. The layers swing past the stable state angle, during a period marked PS (Post-Switch). This period lasts for approximately 100μs. The data capture timeframes did not last long enough to see if there was also asymmetry in the PS maximum angle.

Such changes in layer direction were unexpected, as they have not been mentioned in any switching theories (section 2.5.3), nor have they been reported experimentally. It is important to emphasise that the rotation occurs in a plane parallel to the cell face. The diffraction spot is

caused by the layers in one arm of the chevron structure. The fact that the diffraction spot did not appear to fragment on switching implies that at least the majority of the layers throughout this half of the sample thickness participate in the rotation. From the x-ray evidence however, it is not possible to say weather or not layers close to the surface were involved. It is also not possible to say weather or not layers in the unobserved arm of the chevron structure also rotated, although it is reasonable to assume they did.
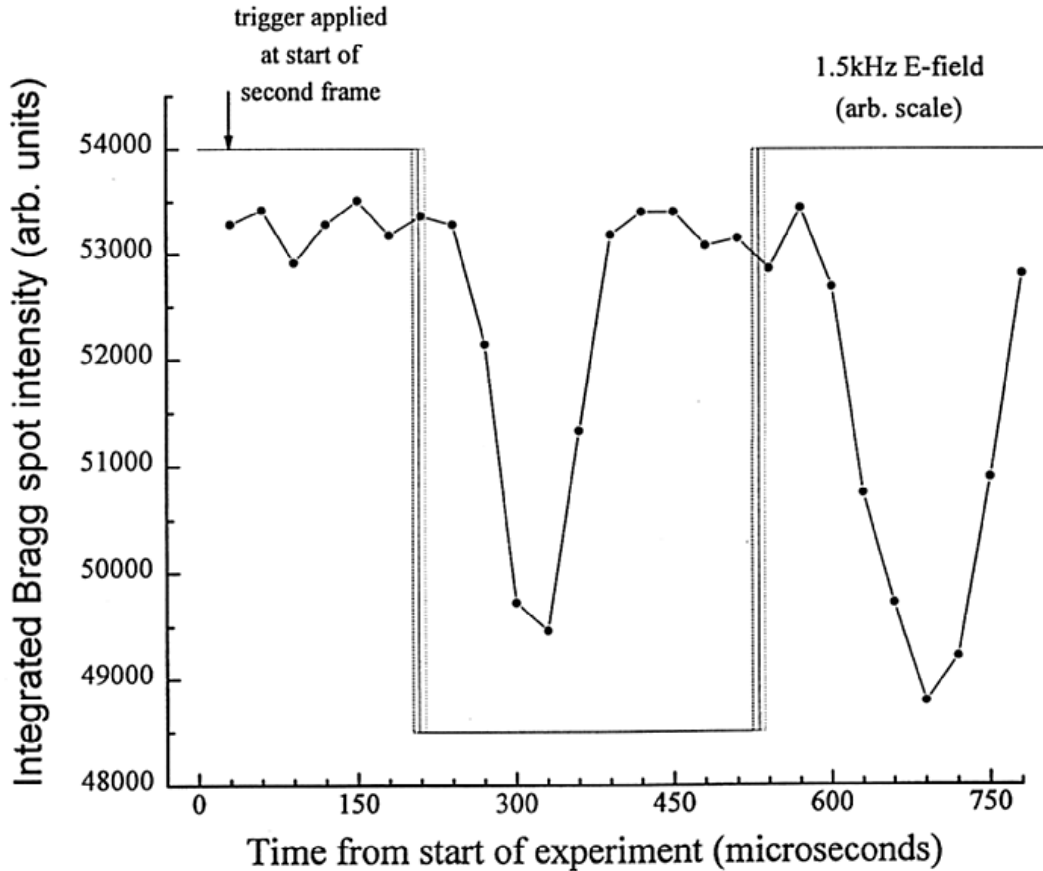
Figure 81: The diffracted intensity against time during switching. Each data point represents the accumulated intensity in the previous 30μs.

The plot shows a fall in intensity after approximately 60μs of field reversal, followed by a rise back to the pre-switched level. The dip in intensity might be due to:

i)   The formation of an asymmetric chevron structure, the observed arm of the chevron being the shorter of the two arms during switching.

ii)   A change in chevron angle during switching.

Without having performed the experiment at more rocking angles it was not possible to distinguish between these two factors. In the light of the switching theories (section 2.5.3.5) it seems more likely that the second factor is correct however; such layer behaviour having been hypothesised by Hartmann *et al* [47] (see Figure 27).

5.5.4 Electro-optic measurements

The ferroelectric electro-optic experiment is similar to the smectic-A electro-optic experiment (section 4.5.6), except that the emphasis in the ferroelectric case is on determining the timescale of the switching rather than on analysing the switching process. The theory is the same as that describing smectic-A electro-optic response measurements (section 2.4.3), with a slight difference: because there is no change in the number of domains during ferroelectric switching there is no observable time-dependent scattering component in the intensity of the transmitted light. The experiment is thus simply a measurement of the change in perceived birefringence with time.

The electro-optic measurement apparatus was the same as that used in the smectic-A experiment (section 4.5.6). The sample was held at 54.5°C. A +6V D.C voltage was first applied to the cell to switch all the molecules into, say, the UP state. The cell was then rotated about the axis of the laser beam, until the director was aligned with one of the polarisers. This position corresponded to a minimum in transmitted light intensity.

The applied waveform was changed to a +/- 6V square wave. This caused the director to switch back and forth continuously. As it moved to the DOWN state the perceived birefringence increased and the transmitted light intensity rose. The oscilloscope was set to trigger from the rising edge of the square wave, recording the electro-optic response. The waveform frequency was set so that the response saturated i.e. so that the director fully switched in one direction before it reversed. An appropriate setting was 1.5kHz. The display was averaged over 256 switching cycles.

The ferroelectric electro-optic response results are shown below.
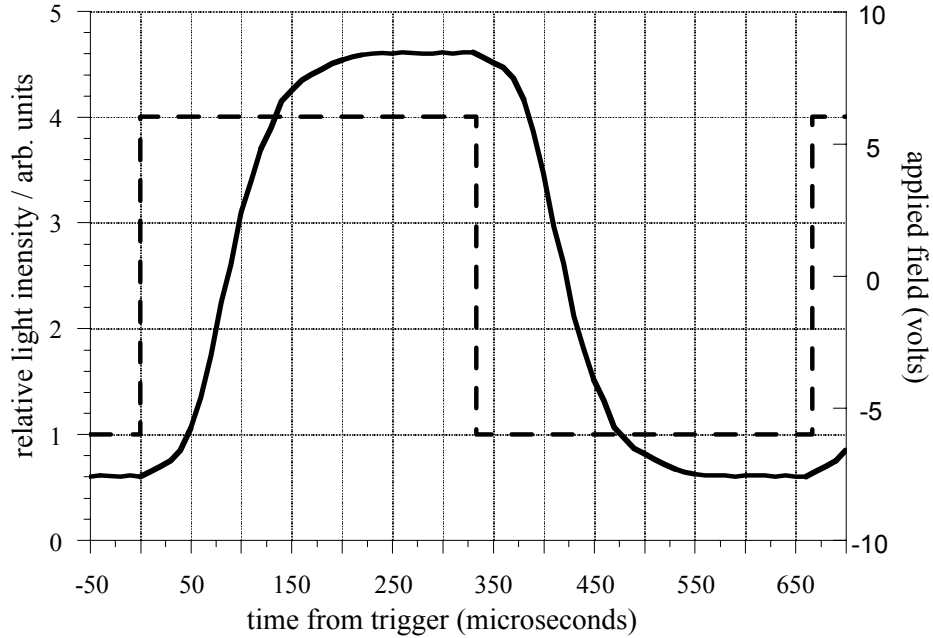
Figure 82: Ferroelectric electro-optic response.

The 10%-90% response time was measured, using the oscilloscope to be 200μs (+/-10μs).

Photographs were taken to show the optical difference between the UP and DOWN states. The apparatus used for taking the photographs was the same as that described in section 4.5.5. The cell was oriented so as to give the largest optical contrast between the two states. +6V was applied to the cell while a photograph was taken in the UP state (Figure 83a). –6V was then applied to the cell while a photograph was taken in the DOWN state (Figure 83b).
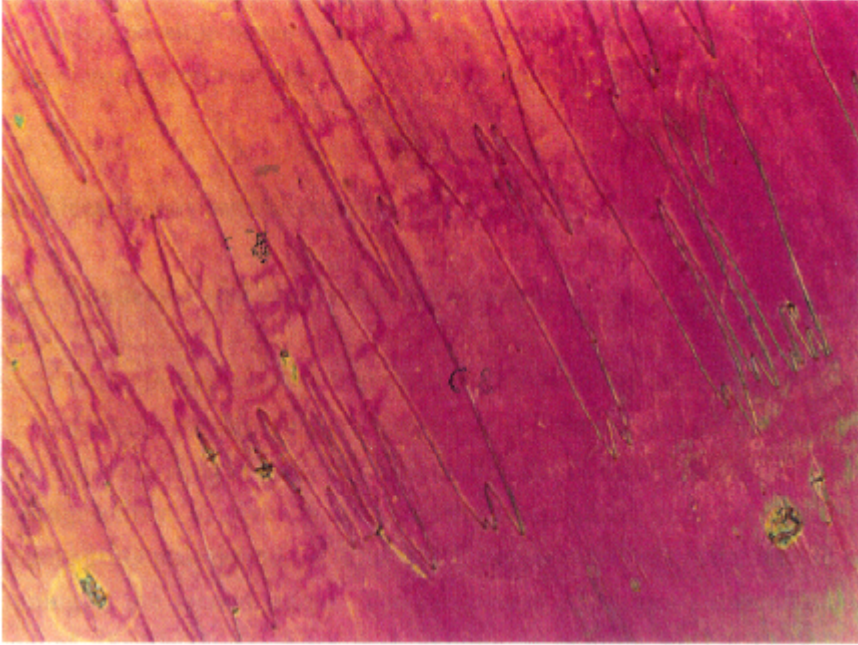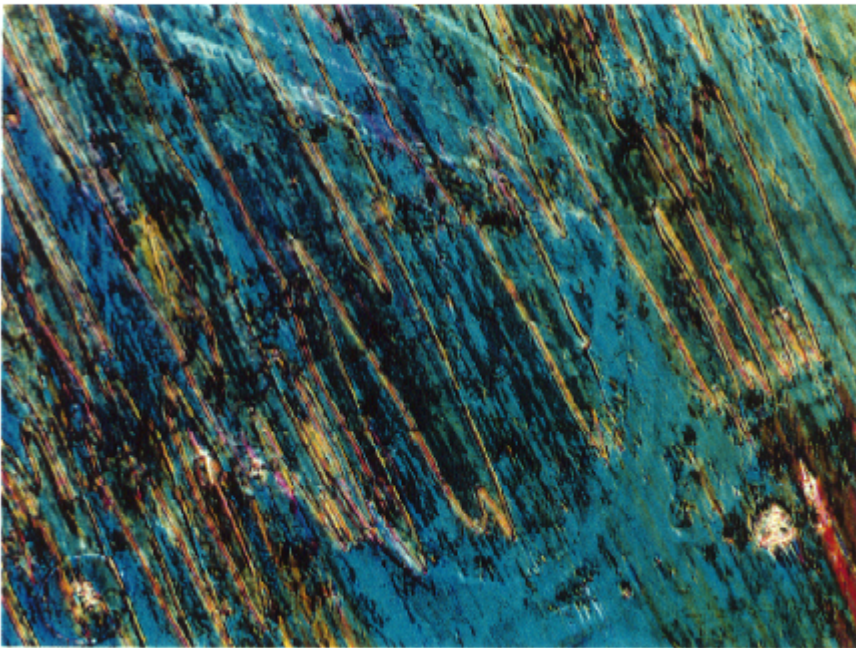
Figure 83: Photographs of the ferroelectric cell with a low electric field applied to switch the director between a) the UP state and b) the DOWN state. The cell is viewed between crossed polarisers.

The photographs show zigzag defects, indicative of conflicting chevron directions within the cell. A completely dark state was not possible because of a) the large spread in alignment (see section 5.4) and b) the splayed director profile within the chevron structure (see section 2.5.3.4).

5.5.5 Proposed model for switching

On application of an electric field to an SSFLC the molecules rotate around the cone defined by the tilt angle. This rotation is helped by a wobble of the chevron structure and by a simultaneous rotation of layers in the planes parallel to the cell faces (Figure 84). The reason for the "wobble" has been explained by Hartmann *et al* [47] on the basis of a coupled layer-director model. The reason for the layer rotation isn't known. It could perhaps be due to domain motion in the plane of the chevron apex. This would not affect the surface anchoring.
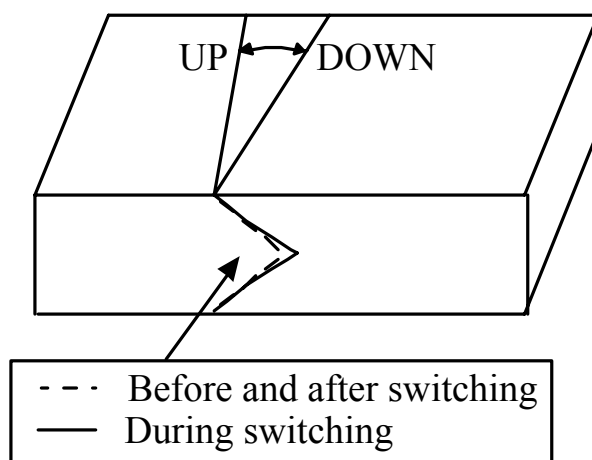
Figure 84: Representation of layer behaviour during director switching in a ferroelectric liquid crystal cell. The angular variation at the cell surface is greatly exaggerated.

5.6   Summary of the ferroelectric experiments

A chevron structure has been shown to exist in the ferroelectric cell used in this thesis. On application of high electric fields (~2.5V/μm) the structure has been shown to undergo an irreversible deformation. The sharp chevron structure has been shown to change to a low-tilt obtuse chevron structure, which is asymmetric. The use of an area detector has revealed that the deformation also involves a restructuring of layers in the planes parallel to the cell faces.

On application of low electric fields (~1.5V/μm) the director was seen to rotate around the cone defined by the tilt angle, to its stable state. Time-resolved x-ray diffraction showed that this motion was accomplished via a small (~1°) layer rotation in the planes parallel to the cell faces, and a simultaneous "wobble" of the chevron structure. This was the first time ever that layer motion has been observed during ferroelectric switching.

Chapter 6

SUMMARY AND SUGGESTIONS FOR FUTURE RESEARCH

Thesis Summary

A detailed review of previous switching studies has been presented for both smectic-A and ferroelectric liquid crystals.

A review of liquid crystal x-ray diffraction patterns has been presented.

The effect of electric fields on a smectic-A liquid crystal was examined. An initial x-ray investigation showed the existence a chevrons structure, which was shown to form as a consequence of a decrease in layer spacing on cooling. On application of an electric field to the cell a time-resolved x-ray experiment showed that the smectic layers rotate intact, coupling with the director rotation. Electro-optic experiments showed that switching began near cell defects. They also showed that layers in a domain rotate, in preference to co-operative rotation with adjacent domains. This made the electro-optic response dependent on the position and size of the incident light beam relative to the cell face.

The affect of high and low electric fields on ferroelectric liquid crystals was examined. X-ray rocking curves showed that (high) electric field treatment (E.F.T) caused a structural change of the layers in the planes normal to the cell faces. An area detector allowed a simultaneous movement of the surface layers to be seen. The results account for the contradiction between the Srajer model [54] and the experimental observations made by other authors.

Time-resolved x-ray diffraction was used to monitor layer motion during director switching in a low electric field. The results showed that switching involved a small rotation of the layers in the planes parallel to the cell faces and a simultaneous "wobble" of the chevron structure. The wobble of the chevron structure is indicative of a coupled layer-director model, as proposed by Hartmann *et al* [47].

This thesis also includes the first comprehensive reference guide to the interpretation of x-ray rocking curves obtained from smectic liquid crystal cells (Appendix B).

Note: This abridged version of the full thesis does not include a description of a novel apparatus designed (and tested) for simultaneous electro-optic and x-ray studies of liquid crystals. See reference [94] for more details.

Suggestions for future research

Because of time constraints the x-ray rocking angle resolution poor. In particular it was not possible to distinguish between a symmetric and an asymmetric chevron structure. Any future research should use smaller rocking steps.

The cell thickness measurements had acceptable errors for the purposes of the qualitative results

presented in this thesis. The use of a spectrophotometer, rather than a micrometer, would be advised for quantitative experiments, however. The spectrophotometer is typically accurate to within +/- 0.2μm [85].

Further work on smectic-A materials could involve an x-ray analysis switching in cells containing a true bookshelf structure, where there is no preferred layer rotation direction. Such a system might perhaps be necessary for the appearance of a Parodi defect array (section 2.4.2). Future work could also look at the effect of different planar alignment agents on the switching process.

Further research on ferroelectric materials could involve a more detailed E.F.T x-ray study of SCE13 cells, looking specifically to see if the structure is completely bookshelf on application of electric fields higher than those used in this thesis. Other work might include further time-resolved x-ray studies of layer behaviour in SCE13 cells, in order to reproduce the results obtained in this thesis. Research into the effect of specific electric field waveforms might also be interesting.

<div style="border: 1px solid black;">

Appendix A:
DEFECTS IN SMECTIC LIQUID CRYSTALS

</div>

A.1 Basic Definitions

Conic:

A curve formed by the intersection of a plane with a circular cone. This "curve" could be an ellipse, circle, parabola, hyperbola or a straight line.

Focal Conics:

Two or more conics which share the same focus.

A.2 The Dupin Cyclide

The building block for the focal conic defect is the Dupin cyclide.

L1
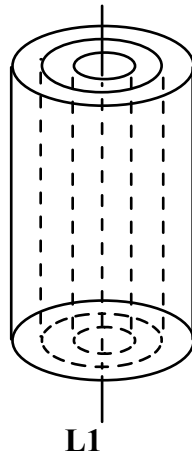
The cyclide consists of cylindrical layers that are lie around a line singularity L1.

A.3 The Toroidal Focal Conic Defect

The Dupin cyclide folds into a ring. The defect L1 becomes a circle and a new line defect, L2, emerges.
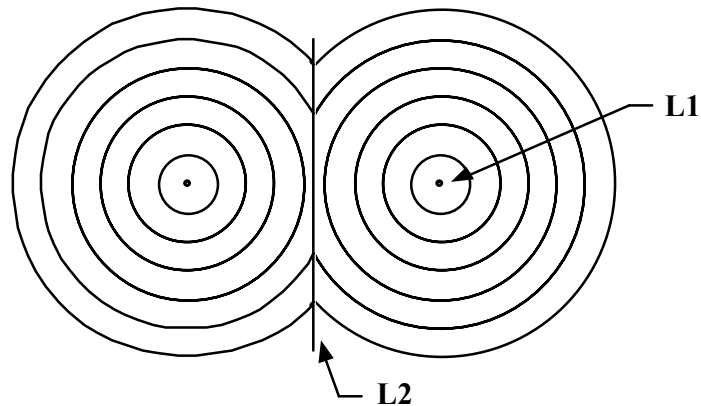
A.4 The Focal Conic Defect

The Dupin cyclide folds into an ellipse. Additional layers are added. L1 becomes an ellipse and L2 is a hyperbola.
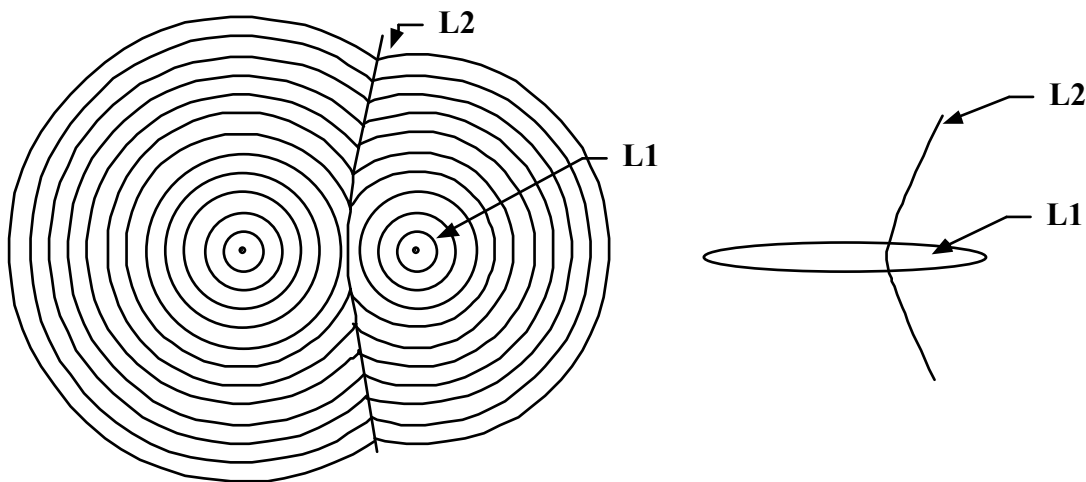
In reality the defect size is limited by director splay energy and the layers form within a shape defined by the defect line singularities as shown below,
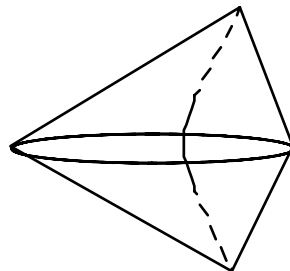
A.5 The Parabolic Focal Conic Defect

This defect is quite often seen in planar smectic-A samples. It is made from two intersecting parabolic defect lines.
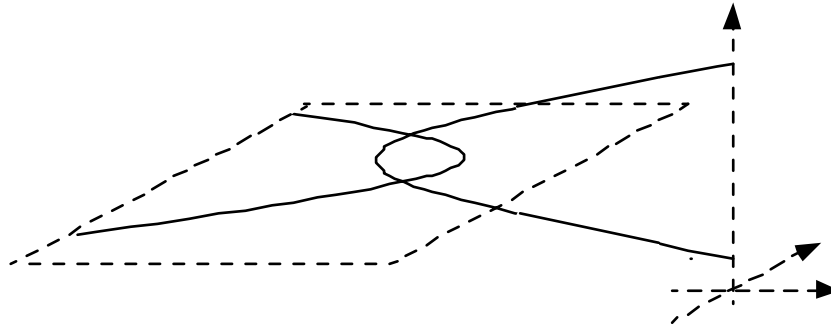
A.6 The Boundary Focal Conic Defect

This is a common defect in smectic-A systems. It occurs when a focal conic defect is restricted by a boundary wall.

surface
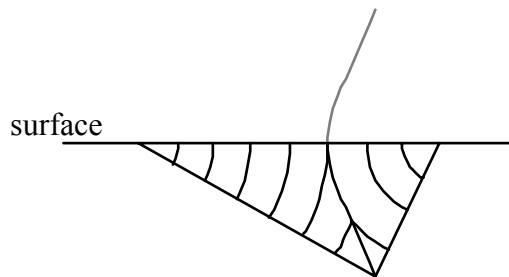
A.7 The Boundary Toroidal Focal Conic Defect

This defect occurs when the toroidal focal conic defect is restricted by a boundary wall.

plan view

surface

side view
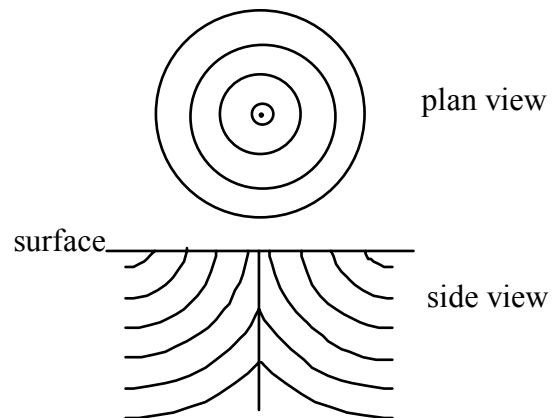
Appendix B:
GUIDE TO X-RAY ROCKING CURVES

This guide shows the typical x-ray rocking curves for smectic systems and the cell layer structures that cause them. A standard nomenclature is presented for the cell structures, because different research groups call each structure by a different name (in particular the term "quasi-bookshelf" is ambiguous).

Notes:

i) The rocking angle is defined to be 0° when the incoming beam hits the cell at the appropriate (Bragg) angle to give diffraction from bookshelf layers.

ii) Background counts have been subtracted.

iii) The samples are assumed to be well-aligned.

iv) The rocking axis is parallel to the surface layers, as below:
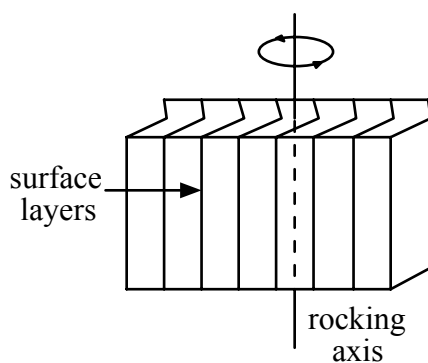
The surface layers are assumed to be parallel over the entire cell surface and the surface layer direction is assumed to remain constant. These assumptions are valid for the majority of cases.

Table B1: X-ray Rocking Curves and Inferred Cell Structures—continued overleaf
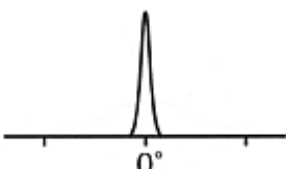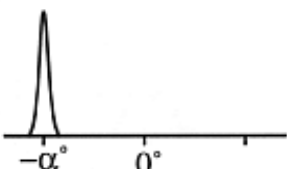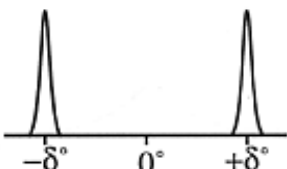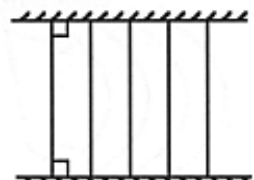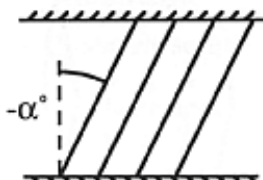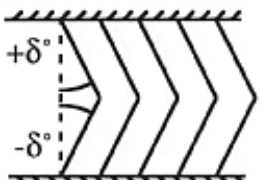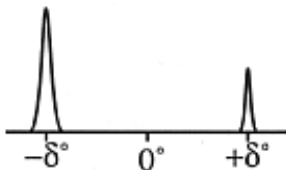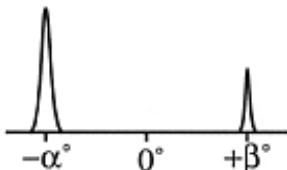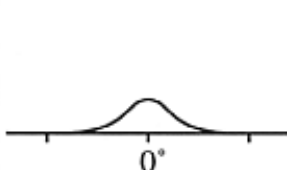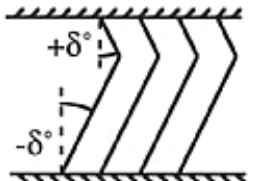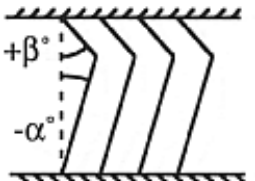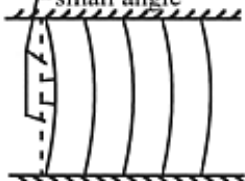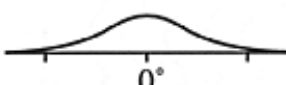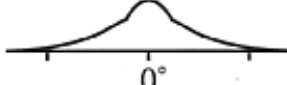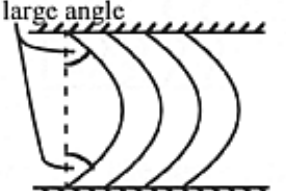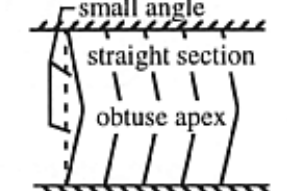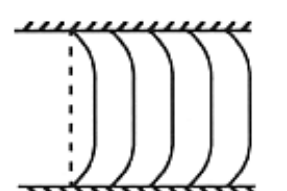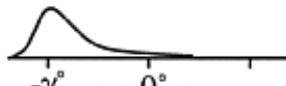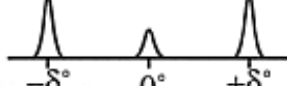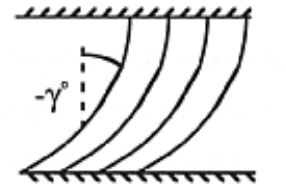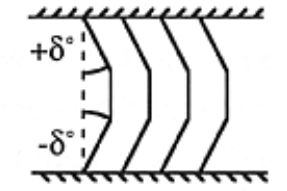
Rocking Info.	$0°$	$-\alpha°$ $0°$	$-\delta°$ $0°$ $+\delta°$
Inferred Structure		$-\alpha°$	$+\delta°$ $-\delta°$
Author-given names	Bookshelf	Tilted Bookself Quasi-bookshelf	chevron
My name	Bookshelf	Tilted Bookself	chevron

Rocking Info.	$-\delta°$ $0°$ $+\delta°$	$-\alpha°$ $0°$ $+\beta°$	$0°$
Inferred Structure	$+\delta°$ $-\delta°$	$+\beta°$ $-\alpha°$	small angle
Author-given names	Asymmetric chevron	Asymmetric chevron	Quasi-bookshelf Bent bookshelf
My name	Asymmetric chevron	Asymmetric chevron typeII	Bent bookshelf

96

Table B1 continued…

Rocking Info.	0°	0°	0°
Inferred Structure	large angle	small angle / straight section / obtuse apex	
Author-given names	Quasi-bookshelf Obtuse chevron	Quasi-bookshelf Obtuse chevron	Bookshelf Quasi-bookshelf Bent bookshelf
My name	Obtuse chevron	low-tilt obtuse chevron	Quasi-bookshelf

Rocking Info.	$-\gamma°$ $0°$	$-\delta°$ $0°$ $+\delta°$	
Inferred Structure	$-\gamma°$	$+\delta°$ / $-\delta°$	
Author-given names	Quasi-bookshelf Bent tilted Tilted	not named	
My name	Bent tilted	chevron/bookshelf aggregate	

<u>The Effect of a Change in Surface Layer Direction on Rocking Curves</u>

If the angle of the surface layers changes then the required axis for rocking is altered. This happens, for example, when a surface chevron structure emerges, as shown below.
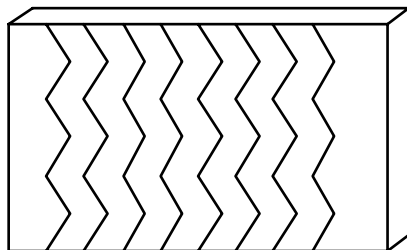
For x-rays this structure is equivalent to a single chevron across the cell surface.
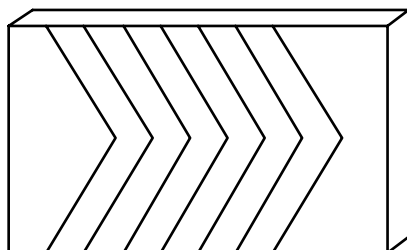
The single-chevron representation is used for clarity in the following discussion.

The cell diagrams overleaf depict the general set of structures that *might* occur during Electric Field Treatment of SSFLC cells. The corresponding diffraction patterns are based on the following experimental set-up:
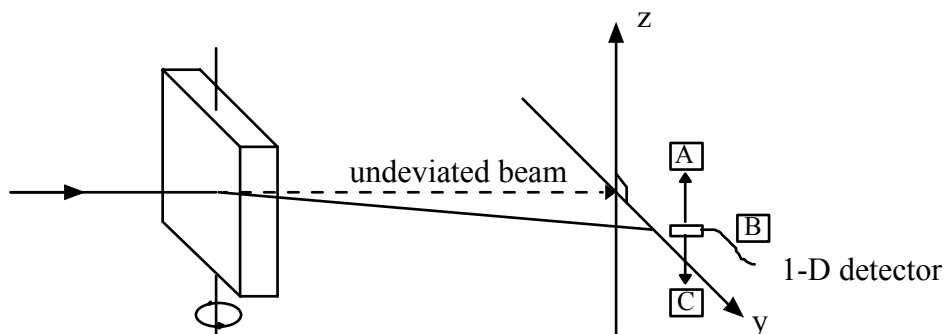
The cell is rocked about the z-axis. A 1D detector sits on the equator at position B, the position corresponding to Bragg diffraction from the layers. A rocking curve is obtained. The 0° position is defined as the cell angle at which (Bragg) diffraction occurs for the layers. A and C are additional detector positions in the z-y plane, above and below B.

Table B2. The Effect of a Change in Surface Layer Direction on a 1D rocking curve
—continued overleaf
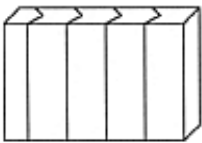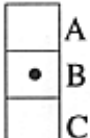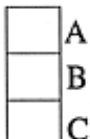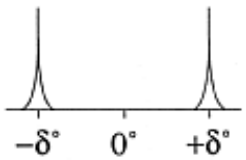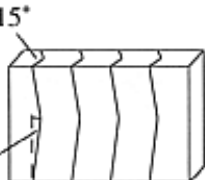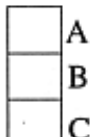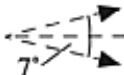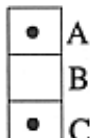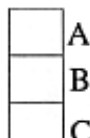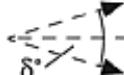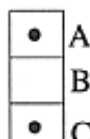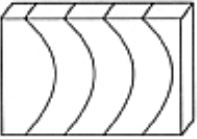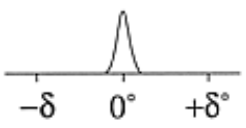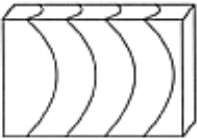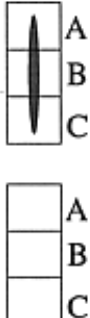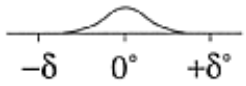
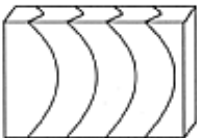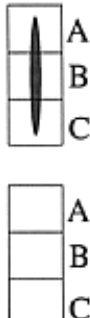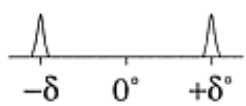| Cell structure	Detector information	Rocking curve for detector on the equator (B)
standard thickness chevron chevron angle = δ°	some cell (rocking) angles : +/- δ ° A / • B / C any other angle A / B / C	(two peaks) −δ° 0° +δ°
~15° thickness chevrons ~7° surface chevrons 15° 7°	some cell (rocking) angles : +/- δ ° or any other angle A / B / C 15° • A / B / • C 7°	−15° 0° +15° i.e. nothing, even at 15°!
thickness bookshelf + ~δ° surface chevrons δ°	some cell (rocking) angles : +/- δ ° or any other angle A / B / C 0° • A / B / • C δ°	−δ 0° +δ° i.e. nothing, even at δ°!

Table B2 continued…

Cell structure	Detector information	Rocking curve for detector on the equator (B)
thickness bookshelf + obtuse surface chevrons	some cell (rocking) angles : 0° spread A B C any other angle A B C	low intensity
bent thickness bookshelf + obtuse surface chevrons	some cell (rocking) angles : 0°+/- a few ° spread A B C larger angles A B C	low intensity
thickness chevrons + obtuse surface chevrons chevron angle = δ°	some cell (rocking) angles : +/- δ° spread A B C any other angle A B C	−δ 0° +δ° low intensity

100

<u>Notes</u>

i) When the surface has straight chevrons and the detector is on the equator a rocking curve will not show the structure within the cell (chevron or bookshelf).

ii) If the surface chevrons are obtuse then the structure within the cell will be seen in a rocking curve although with low intensity.

iii) The diagrams show the benefit of using a 2D detector i.e. diffraction away from the equator can be seen by rocking about a single axis. (The diffraction pattern reflects the structure of the cell surface.)

REFERENCES

[1] B. Bahadur, "Liquid Crystals: Applications and Uses", vols. 1, 2 and 3, World Scientific, Singapore, 1991.

[2] K. Toyne, "Thermotropic Liquid Crystals", ed. G. Gray, published for The Society of Chemical Industry by John Wiley & Sons, UK, 1987.

[3] H. Kelker and R. Hatz, "Handbook of Liquid Crystals", Verlag-Chemie, Weinheim, 1980.

[4] G. Vertogen and W.H. de Jeu, "Thermotropic Liquid Crystals, Fundamentals", Springer Series in Chemical Physics, 45, Berlin, 1988.

[5] P.G de Gennes and J. Prost, "The Physics of Liquid Crystals", 2nd ed., Oxford University Press, 1993.

[6] G. Gray and J.W. Goodby, "Smectic Liquid Crystals", Leonard Hill, Glasgow, 1984.

[7] R.B. Meyer, L. Liébert, L. Strzelecki, and P. Keller, J. de Phys. Letts., 36, L69, (1975).

[8] L.M. Blinov and V.G Chigrinov, "Electrooptic Effects in Liquid Crystal Materials", Springer and Verlag, 1994.

[9] M. Schadt, "The Twisted Nematic Effect: Liquid Crystal Displays and Liquid Crystal Materials", Mol. Cryst. Liq. Cryst., 165, 405, (1988).

[10] J.W. Goodby et al, "Ferroelectric Liquid Crystals. Principles, Properties and Applications" (Ferroelectricity and Related Phenomena, Vol. 7), Gordon and Breach Science Publishers, U.K, 1991.

[11] W.H. de Jeu, "Physical Properties of Liquid Crystalline Materials", Gordon and Breach Science Publishers, UK, 1980.

[12] V. Fredericks and V. Zolina, Trans. Faraday Soc., 29, 919, (1933).

[13] A. Rapini, J. de Phys., 33, 237, (1972).

[14] E.F. Carr, Phys. Rev. Letts., 24, 807, (1970).

[15] C. Tani, App. Phys. Letts., 19(7), 241, (1971).

[16] P.G. de Gennes,"The Physics of Liquid Crystals", 1st ed., Oxford University Press, 1974.

[17] O. Parodi, Solid State Comms., 11, 1503, (1972).

[18] M. Goscianski, L. Leger and A. Mircea-Roussel, J. de Phys.Letts., 36, L-313, (1975).

[19] K. Yoshino, K. Yamashiro and Y. Inuishi, Jap. J. appl. Phys., 14(2), 216, (1975).

[20] M. Hareng, S. le Berre and J.J. Metzger, Appl. Phys. Letts., 27(11), 575, (1975).

[21] D.K. Rout and R.N.P. Choudhary, Mol. Cryst. Liq. Cryst., 166, 75, (1989).

[22] C.E. Williams and M. Kléman, J. de Phys., 36, C1-315, (1975).

[23] A. Jàkli and A. Saupe, Mol. Cryst. Liq. Cryst., 222, 101, (1992).

[24] M. Hareng, S. le Berre and L. Thirant, Appl. Phys. Letts., 25(12), 683, (1974).

[25] I.G. Chistyakov, B.N. Makarov, L.K. Vistin and C.P. Chumakova, Sov. Phys. Dokl., 21(8), 436, (1976).

[26] J.P. Hurault, J. Chem. Phys., 59, 2068, (1973).

[27] W. Helfrich, Appl. Phys. Letts., 17, 531, (1970).

[28] D.F. Aliev, C.G. Akhundov and A. K. Zeinally, Sov. Phys. Crystallogr., 27(1), 92, (1982).

[29] O.D. Lavrentovich and M. Kléman, Phys. Rev. A, 48(1), R39, (1993).

[30] A.A. Razumov and E.A. Kirsanov, Sov. Phys. Tech. Phys., 27(5), 615, (1982).

[31] H.P. Hinov, Liq. Cryst., 3(11), 1481, (1988).

[32] H.P. Hinov and K. Avramova, Liq. Cryst., 3(11), 1505, (1988).

[33] P.E. Cladis and S. Torza, J. appl. Phys., 46(2), 584, (1975).

[34] H.P. Hinov, J. de Phys., 42, 307, (1981).

[35] H.F. Gleeson, Ph.D. Thesis, University of Manchester, U.K, (1986).

[36] T.P. Rieker, N.A. Clark, G.S. Smith, D.S. Parmar, E.B. Sirota and C.R. Safinya, Phys. Rev. Letts., 59(23), 2658, (1987).

[37] Y. Takanishi, Y. Ouchi, H. Takezoe and A. Fakuda, Jap. J. appl. Phys., 28(3), L-487, (1989).

[38] Y. Ouchi, Y. Takanishi, H. Takezoe and A. Fakuda, Jap. J. appl. Phys., 28(12), 2547, (1989).

[39] L. Limat and J. Prost, Liq. Cryst., 13(1), 101, (1993).

[40] S. Kralj and T.J. Slukin, Phys. Rev. E, 50(4), 2940, (1994).

[41] N.A. Clark and S.T. Lagerwall, Appl. Phys. Letts., 36(11), 899, (1980).

[42] J. Xue and N. Clark, Phys. Rev. E, 48(3), 2043, (1993).

[43] K. Skarp and M.Handschy, Mol. Cryst. Liq. Cryst., 165, 439, (1988).

[44] T.P. Rieker, Ph.D. Thesis, University of Colorado, U.S.A, (1988).

[45] N.A. Clark and T.P. Rieker, Phys. Rev. A, 37, 1053, (1988).

[46] J.C. Jones, "Ferroelectric Liquid Crystals and the Problem with Chevrons", B.L.C.S Newsletter, March 1995.

[47] W.J.A.M. Hartmann, G. Vertogen, C. Gerritsma, H.A.v. Sprang and A.G.H. Verhulst, Europhys. Letts., 10(7), 657, (1989).

[48] F. Giesselmann and P. Zugenmaier, Mol. Cryst. Liq. Cryst., 237, 121, (1993).

[49] A. MacGregor, J. Mod. Optics., 37(5), 919, (1990).

[50] M. Johno, A.D.L. Chandini, Y. Ouchi, H. Takezoe, A. Fakuda, M. Ichihashi and K.

Furukawa, Jap. J. appl. Phys., 28(1), L119, (1989).

[51] M. Johno, Y. Ouchi, H. Takezoe, A. Fakuda, K. Terashima and K. Furukawa, Jap. J. appl. Phys., 29(1), L111, (1990).

[52] W.J.A.M. Hartmann and A.M.M. Luyckx-Smolders, J. Appl. Phys., 67(3), 1253, (1990).

[53] J. Patel, S. Lee and J. Goodby, Phys. Rev. A., 40(5), 2854, (1989).

[54] G. Srajer, R. Pindak and J. Patel, Phys. Rev. A, 43(10), 5744, (1991).

[55] Y. Sato, T. Tanaka, H. Kobayashi, K. Aoki, H. Watanabi, H. Takeshita, Y. Ouchi, H. Takezoe and A. Fakuda, Jap. J. appl. Phys., 28(3), L483, (1989).

[56] M. Oh-E, M. Isogai and T. Kitamura, Liq. Cryst., 11(1), 101, (1992).

[57] K. Itoh, M. Johno, Y. Takenishi, Y. Ouchi, H. Takezoe and A. Fakuda, Jap. J. appl. Phys., 30(4), 735, (1991).

[58] M. Isogai, M. Oh-E, T. Kitamura and A. Mukoh, Mol. Cryst. Liq. Cryst, 207, 87, (1991).

[59] M. Kuwahara, M. Kato, Y. Idoo, T. Terasawa, H. Onnagawa and K. Miyashita, Proceedings of the S.I.D., vol. 32/4, (1991).

[60] T. Uchida, M. Hirano and H. Sakai, Liq. Cryst., 5(4), 1127, (1989).

[61] P. Willis, N. Clark, J. Xue and C. Safinya, Liq. Cryst., 12(6), 891, (1992).

[62] R.F. Shao, P. Willis and N. Clark, Ferroelectrics, 121, 127, (1991).

[63] K. Nagao, M. Yudasaka and T. Harada, Jap. J. appl. Phys., 30, 7A, L1189, (1991).

[64] L. Lejcek and S. Pirkl, Liq. Cryst., 8(6), 871, (1990).

[65] S. Miura, M. Kimura and T. Akahane, Jap. J. appl. Phys., 33, Part1 - 1A, 209, (1994).

[66] N. Itoh, M. Koden, S. Miyoshi, T. Wada and T. Akahane, Jap. J, appl. Phys., 33, Part 2 - 2B, L241, (1994).

[67] J. Patel, T. Leslie and J. Goodby, Ferroelectrics, 57, 137, (1984).

[68] P. Willis, N.A. Clark and C. Safinya, Liq. Cryst., 11(4), 581, (1992).

[69] D.C. Ulrich and S.J. Elston, Liq. Cryst., 17(1), 23, (1994).

[70] A. Jàkli and A. Saupe, Phys. Rev. A., 45(8), 5674, (1992).

[71] Y. Asao and T. Uchida, Jap. J. appl. Phys., 32, Part 2 - 4B, L604, (1993).

[72] D.W.L. Hukins, "X-ray Diffraction by Disordered and Ordered Systems", Pergamon Press, Oxford, 1981.

[73] P.G de Gennes and J. Prost, "The Physics of Liquid Crystals", 2nd ed., Oxford University Press, 1993.

[74] M. Deutsch, Phys. Rev. A, 44(12), 8264, (1991), and references therein.

[75] E. Hecht and A. Zajac, "Optics", Addison-Wesley Publishing Co., U.S.A, 1974.

[76] E.E. Koch, "Handbook on Synchrotron Radiation", vol. 1A, North Holland Publishing Co., Amsterdam, 1983.

[77] E. Towns-Andrews, A. Berry, J. Bordas, G. R. Mant, P. K. Murray, K. Roberts, I. Sumner, J. S. Worgan, R. Lewis and A. Gabriel, Rev. Sci. Instrum. 60(7) 2346 (1989)

[78] Merck-BDH Ltd., Merck House, Poole, Dorset, UK, BH15 1TD.

[79] M.F. Toney, T.P. Russell, J.A. Logan, H. Kikuchi, J.M. Sands and S.K. Kumar, Nature, vol. 374, 709, (1995).

[80] L.M. Blinov and V.G Chigrinov, "Electrooptic Effects in Liquid Crystal Materials", Springer and Verlag, 1994.

[81] Pilkington Space Technology, Unit 2, Kinmel Park, Bodelwyddan Rhyl, Clwyd, UK.

[82] G.E.C. Hirst Research Centre, Elstree Way, Borehamwood, Hertfordshire, UK, WD6 1RX.

[83] Goodfellows Cambridge Ltd., Cambridge Science Park, Cambridge, UK, CB4 4DJ.

[84] Ciba-Geigy Plastics and Adhesives Co., Duxford, Cambridge, UK.

[85] Heather Allinson, Ph.D. Thesis, University of Manchester, UK, (1994).

[86] For example, H.J. Young, "University Physics", 8th ed., Addison Wesley, U.S.A, 1992.

[87] Linkam Scientific Instruments Limited, Tadworth, Surrey, U.K., KT20 5HT.

[88] B.K. Vainshtein, "Diffraction of X-rays by Chain Molecules", Elsevier, Amsterdam, 1966.

[89] MicroCal Software, Inc., One Roundhouse Plaza, Northampton, M.A. 01060, U.S.A.

[90] B.D. Cullity, "Elements of X-ray Diffraction", 2nd ed., Addison-Wesley Publishing Co., U.S.A, 1978.

[91] A. de Vries, A. Ekachai and N.Spielberg, J. de Phys., 40(4), C3–147, (1979)

[92] "International Tables for X-Ray Crystallography", published by Kynoch Press, Birmingham, for the International Union of Crystallographers, 1962.

[93] A. Jàkli and A. Saupe, Mol. Cryst. Liq. Cryst., 222, 101, (1992).

[94] H.F. Gleeson, C. Carboni and A.S. Morse, Rev. Sci. Instrum., 66(6), (1995)